

**LATE CRETACEOUS AND EOCENE PHREATOMAGMATIC
VOLCANISM AND MAGMA-SEDIMENT INTERACTION IN
THE BIG BEND AREA OF WEST TEXAS**

by

Kenneth Befus

Bachelor of Science, 2003
Texas Christian University
Fort Worth, Texas

Submitted to the Graduate Faculty
College of Science and Engineering
Texas Christian University
in partial fulfillment of the requirement
for the degree of

Master of Science

August, 2006

Acknowledgements

Many people helped me during the course of this research project. I would like to offer special thanks to the following individuals:

- Dr. Richard Hanson – Thank you for the effort and professionalism that you brought to all aspects of this project.
- Dr. John Breyer – Thank for you being one of my thesis committee members and for being generous with previous research and assistance during fieldwork.
- Dr. Art Busbey – Thanks for being one of my thesis committee members and for much help in the computer lab, as well as down on Pitcock Ranch (making appointments, ATV details included).
- Dr. Tom Lehman – Thank you for spending a day with me in the field, for sharing your research on Peña Mountain, and for sharing your knowledge of the stratigraphy and paleontology of the Big Bend region.
- Randy Griffen – Thank you for helping deepen this research project by performing U–Pb geochronology on some of the samples.
- Trey Hargrove – Thank you for the advice on how to display the geochronology data.
- Paul Horton – Thanks for sharing your geologic map of the Pitcock Ranch with me and for collaborating on computer drafting back in the lab.
- Mr. Roy Pitcock – Thank you for allowing access to your land and use of the Star House.
- Sid and Mike Ferris – Thank you for the help with the ATV and, more importantly, for the hospitality you offered me during my many visits to the Pitcock Ranch.

Table of Contents

Table of Contents.....	iv
List of Figures.....	vi
List of Tables.....	x
Chapter 1: Introduction.....	1
General setting.....	1
Statement of problem.....	3
Pyroclastic deposits at Peña Mountain.....	3
Tertiary intrusions showing magma-sediment interaction.....	4
Analytical techniques.....	5
Geochronology.....	5
Geochemistry.....	7
General volcanological background.....	8
Introduction to phreatomagmatism.....	8
Pyroclastic facies relationships.....	11
Magma-sediment interaction.....	13
Chapter 2: Regional geology.....	17
Stratigraphy.....	19
Aguja Formation.....	19
Javelina Formation.....	20
Black Peaks Formation.....	21
Hannold Hill Formation.....	21
Canoe Formation.....	22
Chisos Group.....	23
Paleoclimates.....	23
Tectonics and Magmatism.....	24
Late Cretaceous volcanism.....	26
Chapter 3: Late Cretaceous phreatomagmatic volcanism at Peña Mountain, Big Bend National Park.....	31
Geological Setting.....	31
General features of the pyroclastic strata.....	33
Pyroclastic deposits on the northern side of Peña Mountain.....	40
Pyroclastic deposits on the southern side of Peña Mountain.....	47
Less disturbed pyroclastic sequence.....	47
Strongly disturbed zone.....	54
Geochemistry.....	55
Geochronology.....	64
Sample B4.....	65
Sample C29.....	65
Sample C30.....	66
Interpretation of pyroclastic deposits at Peña Mountain.....	70
Interpretation of geochronology.....	78
Chapter 4: Eocene intrusions and magma-sediment interaction.....	81
Introduction.....	81
Dikes and Cottonwood Wash intrusion.....	84

Long east-west-trending dike	85
Dikes in the drainage on the southeastern portion of Pitcock Ranch.....	86
Cottonwood Wash intrusion	97
Geochemistry	100
Conclusion	108
Peperitic diatreme root zones	111
Main diatreme root zone and associated intrusions	117
Interpretation.....	130
Western diatreme root zone	133
Interpretation.....	137
Eastern diatreme root zone	138
Interpretation.....	140
Chapter 5: Conclusions.....	142
References.....	148

List of Figures

Figure 1:	Map showing the geographic location of Big Bend National Park and the study areas of this thesis.....	2
Figure 2:	Lateral facies relationships established by Chough and Sohn (1990) at Songaksan tuff ring.....	12
Figure 3:	Vertical facies sequences compiled by Chough and Sohn (1990).	13
Figure 4:	Stages of magma-sediment interaction and relationship to phreatomagmatic volcanism.	16
Figure 5:	Stratigraphy in the eastern Tornillo basin.	17
Figure 6:	Regional geologic map of part of the Tornillo basin.....	18
Figure 7:	Regional map showing the extent of Tertiary igneous rocks formed by arc magmatism and during Basin and Range extension in Trans-Pecos Texas	25
Figure 8:	Geologic map of fault-bounded pyroclastic deposits on the Pitcock Ranch.....	26
Figure 9:	Measured section of pyroclastic deposits on the Pitcock Ranch.....	27
Figure 10:	Fluidal basalt bomb with teardrop shape.	28
Figure 11:	Clast of carbonized wood in base-surge deposit	30
Figure 12:	Geologic map of the area surrounding Peña Mountain, Big Bend National Park.....	32
Figure 13:	View looking east at the covered contact between Aguja mudstone and Upper Cretaceous pyroclastic deposits on the northeastern side of Peña Mountain.	34
Figure 14:	Typical views of pyroclastic deposits.....	36
Figure 15:	Photomicrographs of basalt from a bomb.	37
Figure 16:	Photomicrographs of angular to fluidal basaltic ash particles in lapilli tuff, set within a matrix of finer ash, mud, and quartz grains.....	37
Figure 17:	Lithic blocks in the pyroclastic deposits at Peña Mountain.....	39
Figure 18:	Centimeter-scale measured section of pyroclastic strata from the northern side of Peña Mountain, divided into packages.....	41
Figure 19:	Measured section of lower and upper pyroclastic sequences on the northern side of Peña Mountain	42
Figure 20:	Truncation surface (dashed) separating upper and lower pyroclastic sequences on the northern side of Peña Mountain.....	43
Figure 21:	Syn depositional normal faults cutting pyroclastic deposits in the lower sequence.....	44
Figure 22:	Planar bedded to laminated, calcareous lacustrine strata that mark the truncation surface in some locations.....	45
Figure 23:	Bedded, lacustrine deposit unconformably overlain by a base-surge deposit at base of upper pyroclastic sequence.....	45
Figure 24:	Araucarioid trunk in pyroclastic strata on the northwestern side of Peña Mountain.....	46
Figure 25:	Tape-and-compass map of part of the southeastern side of Peña Mountain.....	48
Figure 26:	Tape-and-compass map of part of the southern side of Peña Mountain.....	49
Figure 27:	Measured section of less disturbed pyroclastic strata on the southern side of Peña Mountain.....	50
Figure 28:	Lapilli tuff overlying disrupted Aguja mudstone along an erosional contact.....	52
Figure 29:	Tabular mass of erupted mudstone mixed with fluidal basalt clasts.	52
Figure 30:	Close-up of fluidal basalt clasts within tabular mass of erupted mudstone.	53

Figure 31: Basaltic cauliflower bomb, ~1 m across, with irregular lower contact that formed as the bomb shattered upon impact.....	53
Figure 32: Irregular depositional contact (dashed) between disrupted Aguja sandstone and strongly disturbed pyroclastic strata.....	55
Figure 33: Ridge-forming disturbed Aguja sandstone mass (outlined) that rims the northeastern portion of the strongly disturbed pyroclastic strata on the southern side of Peña Mountain.	56
Figure 34: Analyses of basalt bombs plotted on total alkalis vs. silica (TAS) diagram.....	58
Figure 35: Analyses of basalt bombs plotted on Zr/TiO ₂ vs. Nb/Y discrimination diagram.....	59
Figure 36: Analyses of basalt bombs plotted on standard trace-element discrimination diagrams.	60
Figure 37: Analyses of basalt bombs plotted on other standard discrimination diagrams.	61
Figure 38: Analyses of basalt bombs plotted on Th–Hf–Ta discrimination diagram	62
Figure 39: Chondrite-normalized REE patterns for samples of basalt bombs.....	62
Figure 40: Multi-element diagram normalized to MORB for the samples of basalt bombs	63
Figure 41: Multi-element diagram normalized to primitive mantle for the samples of basalt bombs.....	63
Figure 42: Concordia diagram for Sample B4.	65
Figure 43: Tera-Wasserburg concordia diagram for analyses yielding younger ages for Sample B4.	66
Figure 44: Concordia diagram for Sample C29.	67
Figure 45: Tera-Wasserburg concordia diagram for analyses yielding younger ages for Sample 29.....	67
Figure 46: Concordia diagram for Sample C30.	68
Figure 47: Tera-Wasserburg concordia diagram for analyses yielding younger ages for sample C30.	68
Figure 48: Model of two overlapping maar volcanoes at Peña Mountain.....	77
Figure 49: Concordia diagram for the youngest concordant analyses for all three samples from Peña Mountain.	79
Figure 50: Geologic map of the southern flank of the Rosillos laccolith showing locations of all studied Tertiary intrusions.....	82
Figure 51: K–Ar ages and trends of dikes associated with the emplacement of the Christmas Mountains intrusive complex.....	83
Figure 52: Billowed margin of the east-west-trending dike.	87
Figure 53: Elongate billows up to ≤ 5 m long on exposed margin of east-west-trending dike.....	87
Figure 54: Map of southeastern part of Pitcock Ranch showing the drainage where many of the dikes occur.	88
Figure 55: Photomicrograph of billowed margin of long east-west-trending dike.	89
Figure 56: Pillowed area at the eastern outcrop of Dike A.....	90
Figure 57: Small intrusive pillow visibly connected to coherent basalt. The intrusive pillow is surrounded by blocky peperite composed of mudstone and basalt.....	91
Figure 58: Pipe vesicles developed along intrusive pillow margin.....	91

Figure 59: View of blocky peperite composed of altered, angular hyaloclastite shards and disturbed mudstone present along quenched pillow margin.....	93
Figure 60: Tape-and-compass map of parallel dikes.....	93
Figure 61: View of the dike margin exposed in the drainage showing the billowed margin of the dike, intrusive pillow extending from the dike, and baked mudstone	94
Figure 62: View of the billowed contact showing third-order billows superimposed upon second-order billows.....	95
Figure 63: View of third-order billows.....	96
Figure 64: Irregular intrusive relationship with a crook-shaped apophysis that extends from dike C into Black Peaks mudstone.....	97
Figure 65: Outcrop of the Cottonwood Wash intrusion composed of domains fresh and altered basalt.	98
Figure 66: Photomicrograph of fine-scale globular peperite developed between altered basalt and Javelina mudstone in the Cottonwood Wash intrusion.....	99
Figure 67: Analyses of samples from the dikes and Cottonwood intrusion plotted on total alkalis vs. silica (TAS) diagram.....	101
Figure 68: Analyses of samples from the dikes and Cottonwood Wash intrusion plotted on Zr/TiO ₂ vs. Nb/Y discrimination diagram.....	102
Figure 69: Major-element variation diagrams (in wt. %) for samples from the dikes, Cottonwood Wash intrusion, and diatreme root zones	104
Figure 70: Analyses of samples from the dikes, Cottonwood Wash intrusion, and diatreme root zones plotted on standard trace-element discrimination diagrams.....	105
Figure 71: Analyses of samples from the dikes, Cottonwood Wash intrusion, and diatreme root zones plotted on other standard trace-element discrimination diagrams.....	106
Figure 72: Multi-element diagram normalized to primitive mantle for samples from the dikes and Cottonwood Wash intrusion.....	107
Figure 73: Multi-element diagram normalized to MORB for samples from the dikes and Cottonwood Wash intrusion.	107
Figure 74: Chondrite-normalized REE abundances for samples from the dikes and Cottonwood Wash intrusion.	108
Figure 75: Photomicrographs of diabase in the eastern diatreme root zone.	112
Figure 76: Analyses of samples from the diatreme root zones plotted on total alkalis vs. silica (TAS) diagram.	113
Figure 77: Analyses of samples from the diatreme root zones plotted on Zr/TiO ₂ vs. Nb/Y discrimination diagram	114
Figure 78: Multi-element diagram normalized to primitive mantle for samples from the diatreme root zones.....	115
Figure 79: Multi-element diagram normalized to MORB for samples from the diatreme root zones.	116
Figure 80: Chondrite-normalized REE abundances for samples from the diatreme root zones.	116
Figure 81: Geologic map of the western diatreme root zones and associated intrusions.	118
Figure 82: Tape-and-compass map of the main diatreme root zone on the Pitcock Ranch.....	120

Figure 83: Microglobular peperite composed of basalt and Javelina mudstone developed along the intrusive contact of the main diatreme root zone.	121
Figure 84: Limestone, chert, and sandstone cobbles weathering out of Javelina mudstone near the southeastern margin of the diatreme root zone.	122
Figure 85: Globular peperite formed when basalt (dark) intruded into and mixed with wet, unconsolidated sediment (light).	123
Figure 86: Smaller scale globular peperite consisting of basalt and unconsolidated sediment	123
Figure 87: Clastic dike with discontinuous internal layering that parallels the margin of the dike.	124
Figure 88: Inclined pillowed dike that extends from the main diatreme root zone.	125
Figure 89: Tape-and-compass map of the inclined pillowed dike.	126
Figure 90: A) Tape-and-compass map of the irregularly shaped intrusive mass. B) Photograph of intrusion with author for scale.	127
Figure 91: Concordia diagram for the sample taken from basalt within the main diatreme root zone	128
Figure 92: Concordia diagram for the two youngest analyses for the sample taken from basalt within the main diatreme root zone.	130
Figure 93: Model for the formation of the main diatreme root zone.	131
Figure 94: Sketch map of the western diatreme root zone.	134
Figure 95: Northernmost mass of basalt in contact with conglomerate in the western diatreme root zone.	135
Figure 96: Conglomerate-hosted peperite formed between basalt and down-slumped Hannold Hill conglomerate.	135
Figure 97: Outcrop view of the western diatreme root zone looking north.	137
Figure 98: Raft of trough cross-bedded sandstone within the eastern diatreme root zone.	139
Figure 99: Sediment-filled contraction cracks forming well-developed triple junctions.	140
Figure 100: Closely packed peperite consisting of diabase and light-colored sedimentary material.	141

List of Tables

Table 1:	Characteristics of tuff rings and tuff cones	9
Table 2:	Geochemical data for volcanic samples.....	57
Table 3:	Analytical and calculated data from SHRIMP-RG analyses of zircon grains extracted from basaltic bombs in pyroclastic deposits at Peña Mountain.	69
Table 4:	Geochemical data for dikes, Cottonwood Wash intrusion, and diatreme root zones.....	110
Table 5:	Clast counts of conglomerate.....	121
Table 6:	Analytical and calculated data from SHRIMP-RG analyses of zircon grains extracted from basalt at the main diatreme root zone, Pitcock Ranch.....	129

Chapter 1: Introduction

General setting

The Big Bend area of Trans-Pecos Texas (Figure 1) is located in the far southeastern portion of the Basin and Range province, west of the Great Plains. The area contains Upper Cretaceous and Paleogene terrestrial strata deposited in the Tornillo basin. The following six units occur in the Tornillo basin (in order of increasing age) and bear on this study:

- Chisos Group
- Canoe Formation
- Hannold Hill Formation
- Black Peaks Formation
- Javelina Formation
- Aguja Formation

These strata are intruded or overlain by Tertiary (64–17 Ma), alkaline, intrusive and extrusive rocks of the Trans-Pecos magmatic province, which formed during continental arc magmatism and Basin and Range extension (Price et al., 1986; Gilmer et al., 2003). Plio-Pleistocene alluvial fan deposits cover large portions of the Big Bend area, especially in the vicinity of large Tertiary igneous bodies, which form major topographic highs (e.g., Chisos Mountains, Rosillos Mountains).

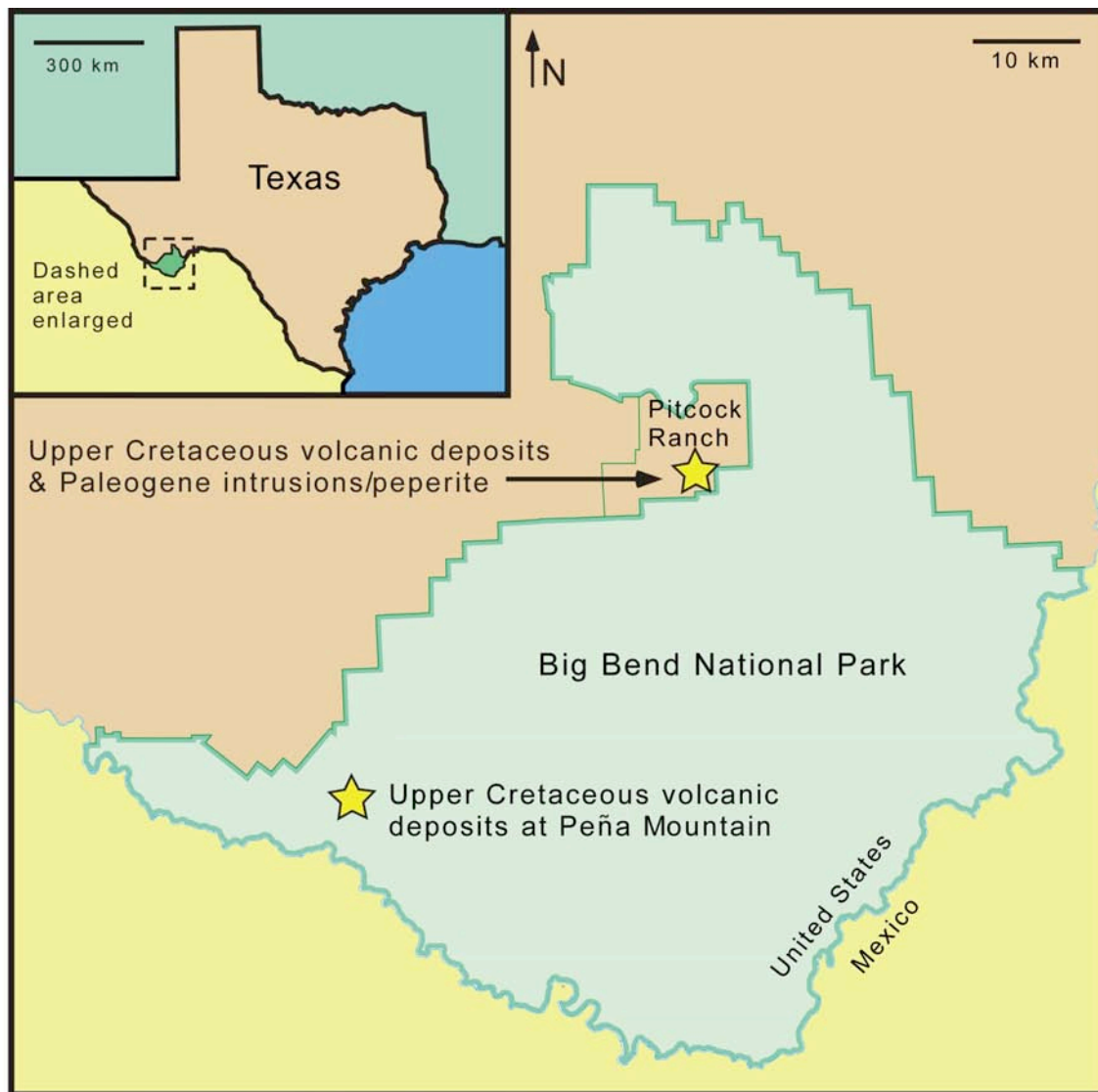


Figure 1: Map showing the geographic location of Big Bend National Park and the study areas of this thesis. Modified from www.nps.gov/bibe/BIBEmaps/BIBE_Map1_noSR.pdf.

Statement of problem

This study focuses on the following two separate volcanological problems in Big Bend National Park and on the Pitcock Ranch north of the park:

- Upper Cretaceous pyroclastic deposits at Peña Mountain, Big Bend National Park
- Tertiary intrusions and associated magma-sediment interaction on the southern flank of the Rosillos Mountains laccolith

Preliminary reports on this research have been presented by Befus et al. (2006a, 2006b).

Pyroclastic deposits at Peña Mountain

Dr. Thomas Lehman first recognized Upper Cretaceous pyroclastic deposits at Peña Mountain during reconnaissance studies in the 1980's; however, these deposits have never been rigorously examined. Until Busbey et al. (1998) and Breyer et al. (2005) described Upper Cretaceous phreatomagmatic deposits on the southern boundary of the Rosillos Mountains laccolith, there were no known Cretaceous igneous rocks in Trans-Pecos Texas, except for distal air-fall tuffs. The phreatomagmatic deposits described herein are very similar to those discussed by Busbey et al. (1998) and Breyer et al. (2005); however, the deposits at Peña Mountain are much better exposed.

The objective of this portion of my research was to examine the Peña Mountain pyroclastic deposits in detail to characterize the eruptive processes, vent locations, and depositional environments of this poorly understood episode of phreatomagmatic volcanism.

The following methods were used to document the pyroclastic deposits at Peña Mountain:

- detailed field mapping of known exposures (1:4000 and tape-and-compass)
- reconnaissance mapping of the surrounding area

- bed-by-bed measured sections to determine depositional features, sedimentary structures, and vertical and lateral facies sequences
- examination of outcrops and polished slabs to document the nature and morphology of pyroclasts
- petrographic studies of basaltic pyroclasts
- major- and trace-element geochemistry of four selected basalt samples (methodology described below)
- U–Pb SHRIMP geochronology performed by W.R. Griffen, Ph.D. candidate at the University of Texas, Dallas (methodology described below)

Tertiary intrusions showing magma-sediment interaction

Numerous Tertiary basaltic to intermediate dikes, sills, and other igneous bodies intrude into and interact with Upper Cretaceous to Paleogene strata of the Javelina, Black Peaks, and Hannold Hill Formations on the Pitcock Ranch and adjacent parts of Big Bend National Park. None of these intrusions has previously been the focus of a detailed research project. In this area, the intrusions and host Cretaceous and Tertiary sedimentary strata are exposed only where erosion has cut through Plio-Pleistocene to Recent alluvial fan deposits (Dennie, 2001).

The objective of this portion of my research was to map a number of the Tertiary intrusions on the southern flank of the Rosillos Mountains laccolith, examine the petrogenetic relationships of the intrusions, and document examples of magma-sediment interaction in detail. The following methods were used to accomplish these goals:

- mapping of dikes, sills, and other intrusive bodies at 1:24,000

- detailed tape-and-compass mapping of important locations
- field examination of intrusive contacts
- petrographic studies of intrusions and zones of magma-sediment interaction
- major- and trace-element geochemistry on eight samples from the intrusions
(methodology described below)

Analytical techniques

Geochronology. Four bulk-rock samples were processed at the University of Texas, Dallas to extract zircon using standard crushing and mineral separation techniques. After separation, zircon grains were handpicked under a binocular microscope in distilled isopropyl alcohol. Analyses were performed in 2005 by W.R. Griffen using the sensitive high mass-resolution ion microprobe with reverse geometry (SHRIMP-RG) co-operated by the U.S. Geological Survey and Stanford University in the SUMAC facility at Stanford University. The following information on analytical techniques has been provided by workers at that facility. Zircon grains were mounted on double-sided tape on glass slides in 1 x 6 mm rows and cast in epoxy to form a disc 25 mm wide by 4 mm thick, which was ground and polished to a 1 μm finish to reveal quasi-equatorial sections through the grains. Digital images of the grains were captured via cathodoluminescence on a JEOL 5600LLV scanning electron microscope and via transmitted light on an optical microscope prior to and following analysis; image quality was enhanced using Photoshop[®] software. Grain mounts were washed with a saturated EDTA solution, rinsed in distilled water, dried in a vacuum oven, and coated with Au.

Mounts typically sat in a loading chamber at high pressure (10^{-7} torr) for several hours before being moved into the source chamber of the SHRIMP-RG. The primary ion beam was first rastered for 120 seconds over the analysis area to remove any surface contamination. The primary beam was then focused for an analysis time of 12 minutes and typically produced an ablation spot 20–40 μm wide and 1–2 μm deep. Secondary ions were generated from the target spot with an O^{2-} primary ion beam at 4–6 nA. Nine peaks were measured sequentially for each zircon spot and included $^{90}\text{Zr}_2^{16}\text{O}$, ^{204}Pb , background (0.050 amu above ^{204}Pb), ^{206}Pb , ^{207}Pb , ^{208}Pb , ^{238}U , $^{248}\text{Th}^{16}\text{O}$, and $^{254}\text{U}^{16}\text{O}$. Autocentering on selected peaks and guide peaks for low or variable abundance peaks (e.g., $^{96}\text{Zr}_2^{16}\text{O}$ 0.165 mass unit below ^{204}Pb) were used to improve the reliability of locating peak centers. Measurements were made at mass resolutions of 6000–8000 (10% peak height), resolutions that eliminate all interfering atomic species. Lead isotope ratios are taken as measured after correction for background. Pb/U ratios were calibrated against the concomitant UO/U ratio, and an overall normalization relating ion intensity to actual ratio was taken at the mean UO^+/U^+ and Pb^+/U^+ values. Concentration data for unknown zircons were calibrated against the R33 zircon standard (419 Ma, quartz diorite of Braintree complex, Vermont, Black et al., 2004), which was analyzed four to five times at the start of each new mount and after approximately every four unknown grains thereafter.

Data reduction followed the methods described by Williams (1997) and Ireland and Williams (2003) and was performed by J. Wooden at the USGS/Stanford lab using SQUID 1.02 (Ludwig, 2001) software. Correction for common lead was performed by fitting a model age for the sample, based on the uncorrected data, to the lead evolution model of Stacey and Kramers (1975) and applying that to the uncorrected data. Analysis points were plotted and

ages calculated using Isoplot/Ex 3.0 (Ludwig, 2000). Decay constants used for age calculation are as follows: $^{238}\text{U} = 1.55125 \times 10^{-10}$; $^{235}\text{U} = 9.8485 \times 10^{-10}$; $^{232}\text{Th} = 4.9475 \times 10^{-10}$. Statistical evaluations were not performed on the points used to calculate the age. Instead, we relied on geological information, zircon morphology and cathodoluminescence, degree of concordance, and visual discrimination between apparent populations of points on the concordia diagram to determine which analyses were most likely to produce an appropriate and meaningful age.

Analytical data acquired by SHRIMP-RG for all grains and apparent concordia ages are presented in later chapters. All analyses are plotted as 2σ error ellipses on regular or Tera-Wasserburg concordia diagrams, and all MSWD values are measurements of scatter of the points relative to concordia. Tera-Wasserburg plots are preferred for microprobe studies because data are plotted exactly as they are measured and because recent Pb-loss from zircon is more easily distinguished (Pb-loss shifts $^{238}\text{U}/^{206}\text{Pb}$ to lower values but does not affect $^{207}\text{Pb}/^{206}\text{Pb}$).

Geochemistry. Bulk-rock samples of a few kilograms were collected in the field and returned to the rock-preparation laboratory at Texas Christian University, where weathered/altered parts of the samples were separated out as best as possible. The samples were initially crushed in a steel jaw crusher and then in a smaller ceramic jaw crusher. The samples were then split into representative portions of ~50 g by repeated use of the cone-and-quarter technique. The samples were sent to the GeoAnalytical Laboratory at Washington State University, where they were ground into powder following standard techniques used by that laboratory. Major- and trace-element concentrations (SiO_2 , TiO_2 , Al_2O_3 , FeO , MnO ,

MgO, CaO, Na₂O, K₂O, P₂O₅, Ni, Cr, V, Ga, Cu, Zn, Bi) were determined by X-ray fluorescence (XRF) on fused glass beads. Refer to <http://www.wsu.edu/~geology/geolab/overview.html> for information on the precision and accuracy of the XRF analyses. The remaining trace-element concentrations (La, Ce, Pr, Nd, Sm, Eu, Gd, Tb, Dy, Ho, Er, Tm, Yb, Lu, Ba, Th, Nb, Y, Hf, Ta, U, Pb, Rb, Cs, Sr, Sc, Zr) were analyzed by an inductively coupled plasma-source mass spectrometer (ICP-MS). Details of sample preparation, precision, and accuracy can be found at the website <http://www.wsu.edu/~geology/geolab/note/icpms.html>.

General volcanological background

Introduction to phreatomagmatism

A phreatomagmatic eruption occurs when magma comes in contact with external water and rapidly converts the water to steam. Experiments on molten fuel-coolant interaction by Wohletz (2002) demonstrated explosive interaction between thermite (basalt analog) and wet, unconsolidated sand. The experiments generated a phreatomagmatic, Surtseyan eruption, which formed a crater and a fine-grained tephra cone. In basaltic systems, violent expansion of water vapor combines with release of magmatic volatiles to drive pulsatory explosions that typically form small, monogenetic tuff rings, tuff cones, and maar volcanoes. Phreatomagmatic eruptions form deposits primarily composed of ash and fine lapilli, even in near-vent settings, due to intense shattering of magma by steam explosions. Condensation of steam or eruption of liquid water produces wet, cohesive air-fall and base-surge deposits (Cas and Wright, 1987).

Base surges are turbulent mixtures of steam, water, and solids that form when the eruption column collapses and spreads laterally (Cas and Wright, 1987). Base surges travel limited distances from the vent as low-particle-concentration density currents. Near-vent base-surge deposits tend to be poorly sorted, crudely stratified lapilli tuff. Thinly bedded tuff with tractional bed forms like antidunes and cross-bedding becomes more common in distal portions of base-surge deposits. This down-current or lateral facies relationship is due to decreasing particle concentration and particle fall-out rate while tractional and sorting processes increase (Chough and Sohn, 1990).

Pyroclastic air-fall deposits form by gravitational fall-out of pyroclasts in an eruption column. The nature of air-fall deposits depends on the nature of the corresponding eruption. In general, deposits form well-sorted, continuous beds that drape underlying topography. They have no tractional bed forms. Phreatomagmatic air-fall deposits are characterized by generally fine-grained pyroclasts and common occurrence of accretionary lapilli and armored lapilli (Cas and Wright, 1987).

The differences between deposits of tuff rings and tuff cones are controlled by the nature of the eruption and the resulting pyroclastic material. The distinguishing characteristics of tuff rings and tuff cones are summarized in Table 1.

Table 1: Characteristics of tuff rings and tuff cones.

Characteristics	Tuff ring	Tuff cone
rim-to-rim width	up to 2000 m	up to 2000 m
maximum dip	less than 12°	less than 30°
rim thickness	less than 50 m	greater than 100 m

Modified from Wohletz and Sheridan (1983)

Tuff cones are composed of thick (> 100 m) sequences of steeply dipping ($> 30^\circ$) pyroclastic beds. Tuff cones develop from wet eruptions in which free water had access to the vent and the water freely mixed with the uprising magma (Wohletz and Sheridan, 1983). Tuff-cone deposits commonly contain vesiculated tuffs, accretionary lapilli, and armored lapilli. Vesiculated tuff forms when water vapor is trapped within wet, cohesive tuff beds upon deposition. Armored lapilli form in steam-rich eruption columns when pyroclasts are coated in sticky, wet ash. Accretionary lapilli form in a similar fashion; however, they are composed entirely of ash-sized particles in concentric layers created by collisions of ash particles in a wet eruption column (Cas and Wright, 1987).

In contrast, tuff rings are composed of relatively thin sequences (< 50 m) of shallowly dipping ($< 12^\circ$) pyroclastic beds. Formation of tuff rings is favored by dry phreatomagmatic eruptions, which occur when water is relatively restricted from the magma. Tuff rings contain high-temperature base-surge deposits with carbonized organic matter (Wohletz and Sheridan, 1983).

Maars are phreatomagmatic volcanoes with craters below the pre-existing ground surface. In general, craters of tuff rings and tuff cones broaden and deepen during eruption until, in some cases, maars form when the eruption excavates below the surface. Tuff rings are associated with maars while tuff cones rarely excavate below the original surface. Excavation leads to collapse/slumping of older surrounding sedimentary strata and newly formed pyroclastic deposits in the crater rim. Collapse is evidenced by disrupted strata, large (10–30 m) normal faults, and small (< 2 m) synsedimentary normal faults. Excavation also leads to the eruption of lithic blocks and smaller pyroclasts of country rock. Lithic blocks

show an inverted stratigraphy when mapped in pyroclastic beds due to progressive excavation through local strata (Wohletz and Sheridan, 1983; Cas and Wright, 1987).

Vent locations often change during phreatomagmatic eruptions. In some cases, multiple vents are active with different production rates. Pyroclastic deposits are usually asymmetrically arranged around a vent due to the influence of prevailing winds (Wohletz and Sheridan, 1983; Cas and Wright, 1987; Sohn and Park, 2005).

Diatremes are conduits of phreatomagmatic volcanoes, which are filled with pyroclastic debris and blocks of country rock (Lorenz, 1973; Lorenz et al., 2002). Diatreme root zones represent the lowest levels of diatremes in tuff rings, tuff cones, and maars. The root zones to the diatremes are composed of irregularly shaped hypabyssal intrusive bodies cutting or intermixed with phreatomagmatic slurry, which consists of massive tephra containing disaggregated sediment and quenched and fragmented magma (White, 1991).

Pyroclastic facies relationships

Figure 2 shows lateral facies relationships compiled by Chough and Sohn (1990) based on detailed research on the Songaksan tuff ring in Korea. The figure shows how the nature of base-surge deposits consistently changes with distance from the vent. Near-vent (< 300 m) deposits are predominantly massive, reversely graded, and have scoured bases, with little to no undulatory, tractional bed forms. Stratified to massive, normally graded deposits are common 300–450 m from the vent; tractional bed forms remain rare in this interval. Beyond 450 m, base-surge deposits are typically well bedded and contain undulatory, tractional bed forms.

Chough and Sohn (1990) also describe three vertical facies sequences based on pyroclastic sequences they observed repeatedly at the Songaksan tuff ring (Figure 3). Vertical facies sequence 1 consists of a basal zone of scoured, bedded tuff with tractional bed forms, which is overlain sequentially by inversely graded tuff, massive tuff, and laminated tuff. This sequence records deposition from a turbulent, near-vent base surge over-ridden by the low-particle-concentration tail of the surge. Vertical facies sequence 2 is composed of reversely to normally graded lapilli tuff, which grades into massive and laminated tuff.

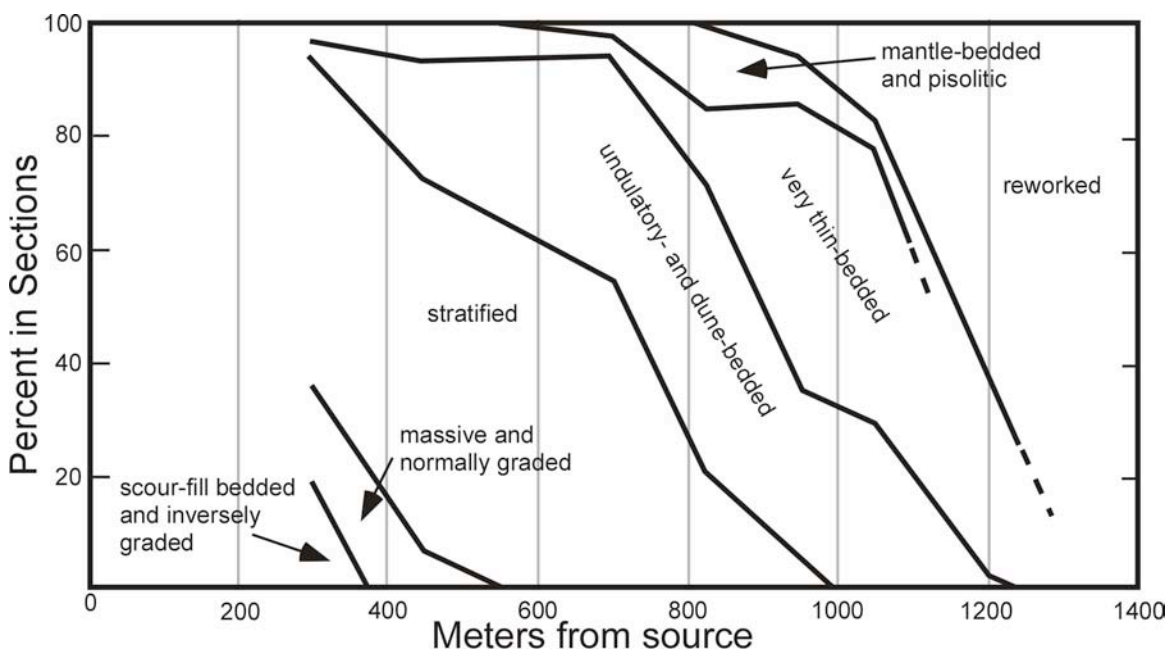


Figure 2: Lateral facies relationships established by Chough and Sohn (1990) at Songaksan tuff ring.

This sequence forms by deposition of near-vent base surges containing coarse lapilli and lithic blocks. Large pyroclasts settle to basal portions of the surges, where dispersive pressure during tractional transport creates reverse grading. These portions of the deposits are over-ridden by turbulent, low-particle-concentration portions of the base surges. Laminated tuff represents deposition from the base-surge tail or post-surge air fall. Vertical facies sequence

3 is composed of a basal, disorganized lapilli tuff that grades into stratified lapilli tuff with undulatory bed forms, which in turn grades into stratified tuff. This sequence records the temporal evolution of a base surge. Basal disorganized lapilli tuff was deposited during rapid fall-out in a near-vent setting. As the surge evolved, a turbulent, high-energy portion of the surge deposited the lapilli tuff with undulatory, tractional bed forms. Stratified tuff records the final, low-energy stages of a base surge where particles were deposited by air fall or from the tail of the surge.

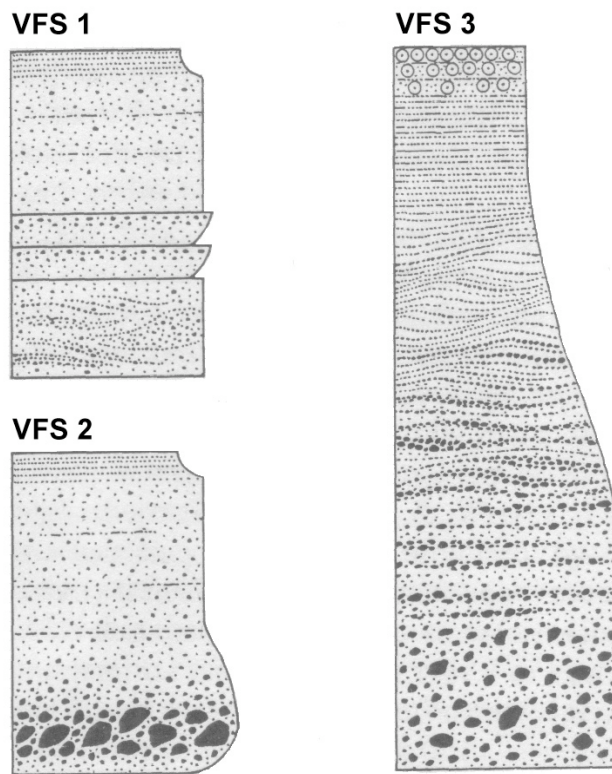


Figure 3: Vertical facies sequences compiled by Chough and Sohn (1990). Accretionary lapilli are shown at the top of VFS 3.

Magma-sediment interaction

Peperite is a rock composed of sedimentary and igneous components that forms when magma intrudes into and interacts with wet, unconsolidated sediment. Interaction between

magma and wet sediment is very common. Peperite forms in common geological settings such as deep subaqueous volcanic environments, emergent subaqueous to subaerial volcanic environments, intrusive environments where magmas cut through aquifers, and lava flowing on wet sediment (Skilling et al., 2002). Past studies demonstrate that understanding the formation of peperite provides insights into the reconstruction of paleoenvironments, relative chronology of igneous activity and sediment accumulation, and the mechanisms of magma-sediment interaction that accompany or precede volcanic eruptions. Since peperite develops in unconsolidated sediment, its formation has generally been taken to indicate penecontemporaneous sedimentation and magmatism (Skilling et al., 2002). As will be shown, this premise is not always valid.

Peperite forms on a variety of scales from less than a cubic meter up to several cubic kilometers. It may form along regular igneous/sedimentary contacts or may develop as highly irregular pods (Skilling et al., 2002). Peperite composed largely of host sediment is termed dispersed peperite, while peperite composed primarily of juvenile, igneous material separated by thin sediment tendrils is labeled closely packed peperite (Hanson and Wilson, 1993; Skilling et al., 2002). Domains of dispersed and closely packed peperite grade into one another in many occurrences. Characteristics of the juvenile component of peperite vary with changes in magma composition and fluidity, as well as with changes in properties of the host sediment such as grain size, degree of consolidation, and water content (Busby-Spera and White, 1987; Hanson and Hargrove, 1999; Skilling et al., 2002). Blocky peperite forms by minor steam explosions and/or quench fragmentation of magma. It commonly shows jigsaw-fit texture. Clasts of globular peperite have highly irregular, fluidal shapes. Globular peperite tends to form from fluidal magma insulated from rapid quenching by vapor films produced

from heating of pore water in the host sediment (Busby-Spera and White, 1987; Skilling et al., 2002).

Many of the dikes and sills examined during this study have irregular contacts marked by cusped, billowed margins and intrusive pillows. Kokelaar (1982), Leat and Thompson (1988), Kano (1991), and Walker (1992) described similar features, formed where magma has come in contact with unconsolidated sediment. In the present study, billows are defined as curved, undulatory surfaces of otherwise tabular intrusions that are separated by cusped, sediment-filled invaginations. Billows can be elongate or equidimensional features that range up to 5 m in length. Intrusive pillows are defined as protruding ellipsoidal bodies that extend from or occur near the main intrusive body. Pillows that are apparently detached from the main body may be connected to it in three dimensions. Intrusive pillows have a typical sack-like shape in two dimensions; however, they may consist of interconnected tubes in three dimensions. Intrusive pillows may have an obvious quenched rim, be associated with hyaloclastite and peperite, and have pipe vesicles (cf. Kano, 1991; Walker, 1992). Figure 4 illustrates the different stages of magma-sediment interaction described above, which may possibly lead to phreatomagmatic explosive activity.

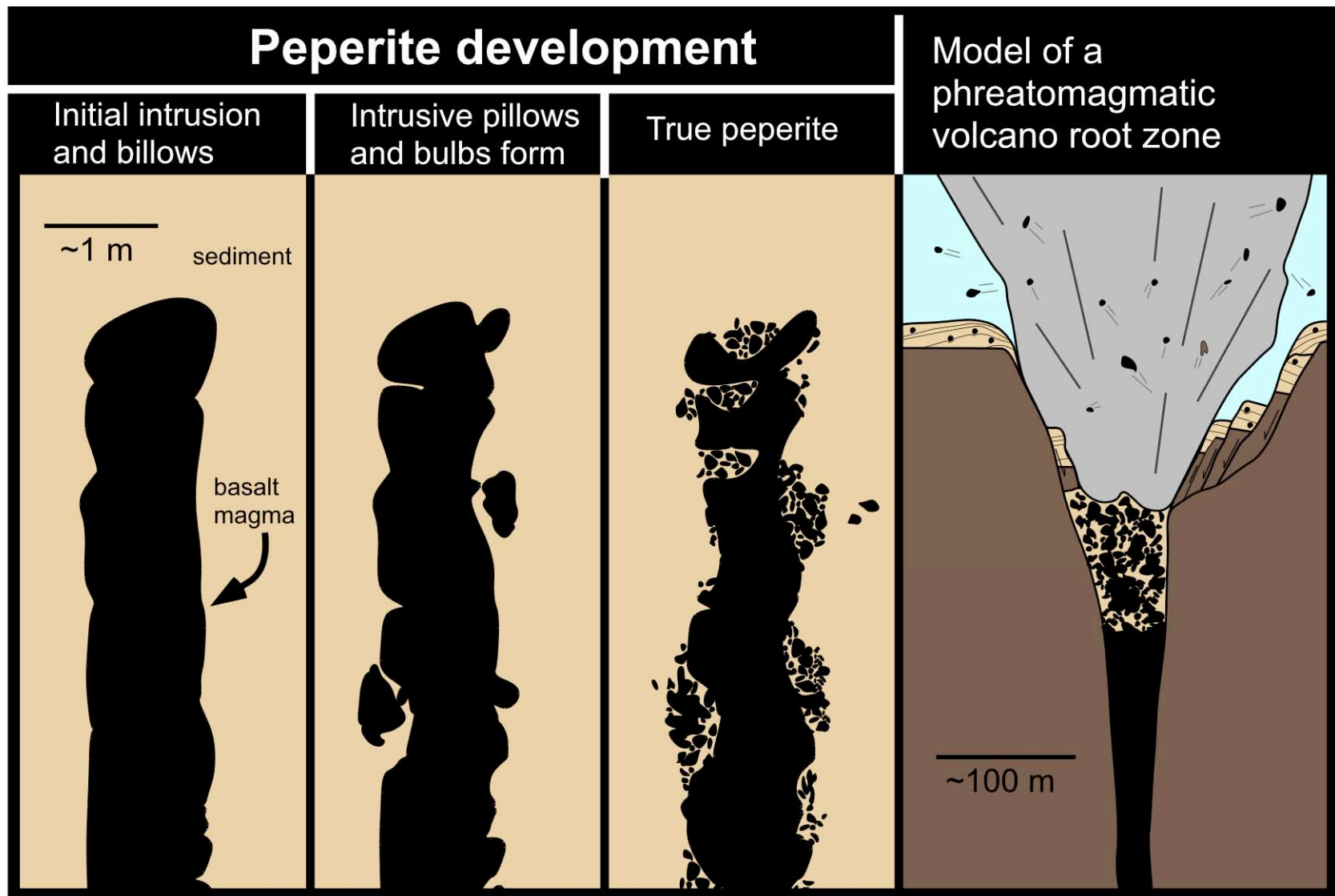


Figure 4: Stages of magma-sediment interaction and relationship to phreatomagmatic volcanism.

Chapter 2: Regional geology

Cretaceous to Tertiary stratigraphic units in the Big Bend area of West Texas which bear on this study are shown in Figure 5 and are discussed in detail below. Stratigraphic nomenclature of Lehman (1988, 1991) is followed; see Schiebout et al. (1987) for an alternate view. The general geologic framework is shown in the map in Figure 6.

Paleogene	Eocene	34 Ma	Priabonian	Chisos Group ≤1000 m
		37 Ma	Bartonian	
		40 Ma	Lutetian	Canoe Formation ~20 m
		49 Ma	Ypresian	Hannold Hill Formation ~250 m
	Paleocene	66 Ma	Thanetian	Black Peaks Formation ~300 m
			Selandian	
			Danian	
	Late Cretaceous	71 Ma	Maastrichtian	Javelina Formation ~130 m
			Campanian	Aguja Formation upper shale member ~100 m
		Marine to deltaic sandstones and shales		
84 Ma		Santonian	Pen Formation	

Figure 5: Stratigraphy in the eastern Tornillo basin. Modified from Maxwell et al. (1967), Lehman (1985), and Lehman and Coulson (2002); time scale from Gradstein et al. (2004). Thicknesses not to scale.

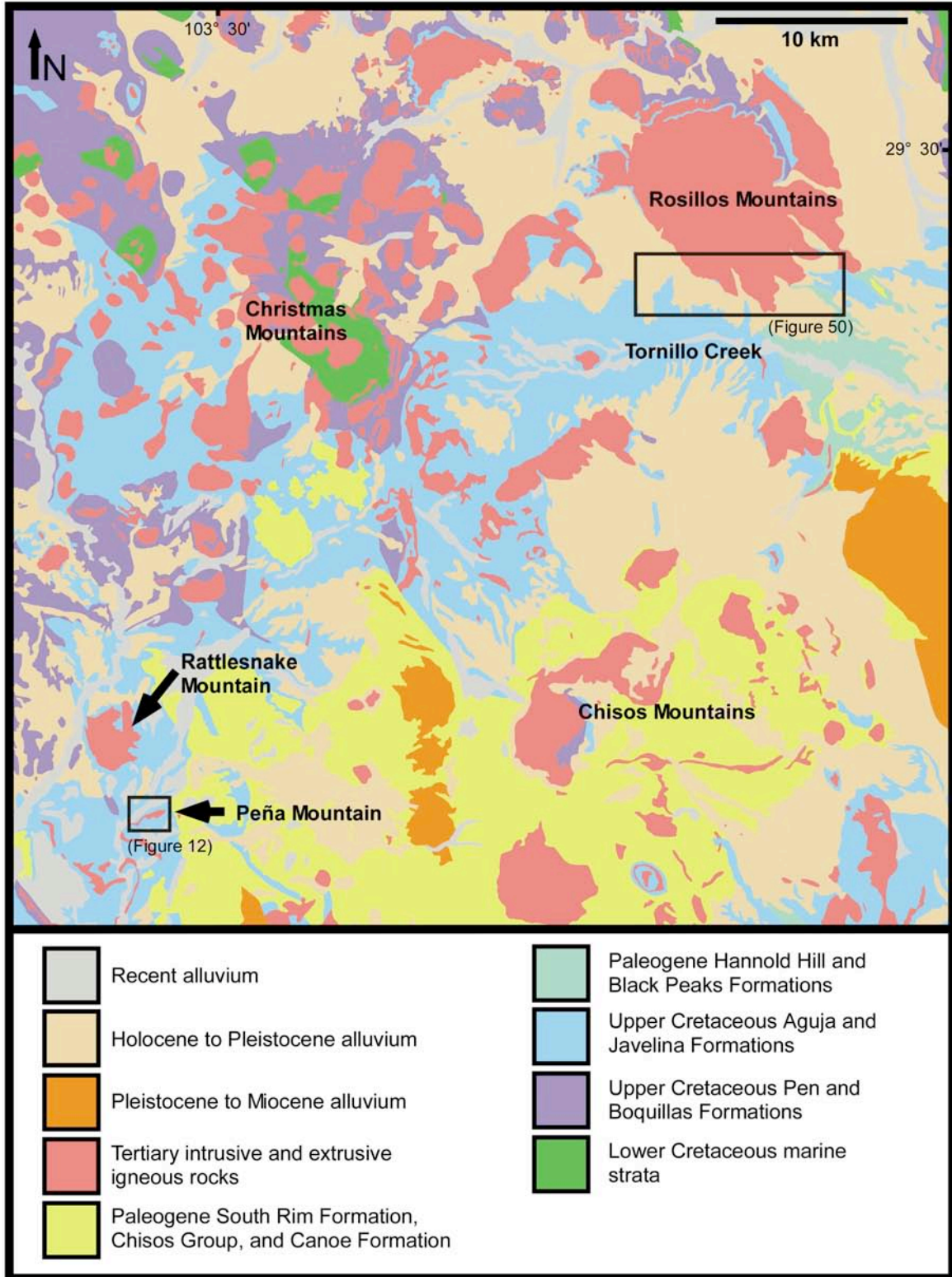


Figure 6: Regional geologic map of part of the Tornillo basin. Study locations are boxed. Modified from Barnes (1979).

During the Jurassic to Early Cretaceous, sedimentation buried a landscape created by the opening of the Gulf of Mexico. In the Late Cretaceous, sedimentation shifted to the Tornillo basin, which is a Laramide-age sedimentary basin that formed in Trans-Pecos Texas (Lehman, 1991). Laramide tectonism during the Paleocene resulted in subsidence in the eastern portion of the Tornillo basin (Lehman, 1986).

Stratigraphy

Aguja Formation

The Campanian to Lower Maastrichtian Aguja Formation is composed of terrestrial and marine members. Marine members conformably overlie or intertongue with marine strata of the Pen Formation (Lehman, 1985; Schiebout et al., 1987) and are fossiliferous, marine mudstones with intercalated deltaic, littoral, and marine sandstones (Lehman, 1985). The terrestrial upper shale member conformably overlies the marine members. The upper shale member is composed of an upper and lower portion, which can be differentiated by the color of mudstones. The lower part of the member is dominantly composed of olive to gray mudstones, whereas the upper portion contains light to dark gray, purple, and maroon color-banded mudstones interbedded with tan, lenticular volcanic arenite and plagioclase arkose (Lehman, 1985). Drab mudstones in the lower part of the upper shale member accumulated in a coastal plain. The upper portion was deposited in an inland floodplain much farther from the coast (Lehman, 1985). Small amounts of freshwater, lacustrine limestone and lignite are also present in the upper shale member (Schiebout et al., 1987). Hadrosaur and ceratopsian dinosaur fossils, as well as remains of crocodylian and turtle species, have been found in the upper shale member (Maxwell et al., 1967; Lehman, 1985).

Tractional bed forms in the upper shale member indicate southeastward sediment transport during deposition, while northeastwardly paleocurrents flowing away from volcanic highlands in Mexico are recorded in the units beneath the upper shale member (Lehman, 1986). This change in paleocurrent direction is concurrent with initiation of Laramide deformation and is also marked by the appearance of coarse volcanic detritus and chert pebbles in fluvial sandstones (Lehman, 1986). Channel sandstones and channel-lag conglomerates contain abundant detrital plagioclase and detrital volcanic rock fragments, which are dominantly intermediate in composition. Lehman (1991) interpreted the large volume of fresh plagioclase to be consistent with a volcanic source. Since there were no known nearby source regions, Lehman (1991) surmised the plagioclase and volcanic rock fragments likely came from magmatic arc volcanism over 500 km away in western Mexico.

Javelina Formation

The Aguja Formation is conformably overlain by the Maastrichtian Javelina Formation. The latter unit is approximately 200 m thick in the study area (Lehman, 1986). Maxwell et al. (1967) placed the contact between these units at “the top of a sandstone above which the beds are predominantly varicolored clay.” The Javelina Formation is dominated by mudstone. It is composed of color-banded, structureless, bentonitic mudstones and yellow to brown lenticular sandstones. Mudstone layers are white, gray, olive-green, maroon, and brown and commonly contain calcite concretions. Lenticular sandstones are typically cross-bedded and contain ripple marks, which indicate southeasterly sediment transport. The sandstones are fluvial channel deposits that contain bone and petrified wood fragments; entire dinosaur bones and coherent petrified logs are generally preserved only in the

mudstones. The Javelina Formation represents a continental floodplain environment consisting of highly sinuous fluvial channel sands and overbank flood-plain deposits (Maxwell et al., 1967; Schiebout et al., 1987; Lehman, 1986, 1991; Lehman and Coulson, 2002).

Varied colors of the extra-basinal chert cobbles in the channel-lag conglomerates suggest the chert cobbles were derived from Lower Cretaceous limestone of the Cox and Glen Rose Formations ~100–200 km away (Lehman, 1986, 1991). The only carbonate clasts in the conglomerates are paleocaliche nodules. Volcanic rock fragments and plagioclase grains occur in Javelina sandstone and channel-lag conglomerate. Lehman (1991) described the coarse volcanic rock fragments as enigmatic because there was no known nearby source.

Black Peaks Formation

The contact between the Black Peaks Formation (Upper Maastrichtian to Paleocene) and the Javelina Formation is conformable (Lehman and Coulson, 2002). The mudstone-dominated Black Peaks Formation is ~225 m thick in the study area (Lehman, 1986). The formation is composed of light-colored, gray to white sandstone and black, gray, and maroon noncalcareous mudstone (Maxwell et al., 1967). Sandstone units have features characteristic of meandering streams. The Black Peaks Formation represents a low-relief floodplain deposit (Schiebout et al., 1987).

Hannold Hill Formation

The Black Peaks Formation is locally unconformably overlain by the mudstone-dominated, Lower Eocene Hannold Hill Formation (Lehman, 1986; Schiebout et al., 1987).

The Hannold Formation is ~100 m thick in the study area and is composed of calcareous to noncalcareous, gray to maroon mudstone, cross-bedded channel sandstone, and conglomerate (Maxwell et al., 1967; Lehman, 1986). Conglomerates contain pebbles and cobbles of black chert, Comanchean limestone, and novaculite up to 8 cm in diameter (Lehman, 1988, 1991). This assemblage is unique because older conglomerates contain no reworked Lower Cretaceous limestone clasts and younger conglomerates contain volcanic clasts (Lehman, 1986, 1988). The Hannold Hill Formation accumulated in a terrestrial floodplain environment; however, a large proportion of lenticular sandstones and the characteristics of the conglomerates likely indicate uplift of adjacent areas and an increase in regional tectonism (Schiebout et al., 1987; Lehman, 1988, 1991).

Canoe Formation

The basal Big Yellow Sandstone Member of the Canoe Formation (Middle Eocene) unconformably overlies the Hannold Hill Formation. In the vicinity of the Canoe syncline, near the study area on Pitcock Ranch, the Canoe Formation is ~20 m thick; however, it is greater than 350 m thick in other locations (Maxwell et al., 1967; Lehman, 1986; Schiebout et al., 1987). The Big Yellow Sandstone Member is a braided stream deposit dominantly composed of massive yellow sandstone with common channel-lag and gravel-bar conglomerates. Above the Big Yellow Sandstone Member, the Canoe Formation is composed of several lava flows, tuff, tuffaceous conglomerate, tuffaceous sandstone, and tuffaceous mudstone deposited in a volcanoclastic apron setting (Maxwell et al., 1967; Schiebout et al., 1987; Runkel, 1990).

Chisos Group

The Chisos Group is ≤ 1000 m thick and crops out predominantly in the Chisos Mountains (Henry and Davis, 1996). It is composed of massive conglomerate, coarse-grained sandstone, tuffaceous fine- to medium-grained sandstone, tuffaceous mudstone, tuff, and lava flows deposited during the Late Eocene to Early Oligocene (Maxwell et al., 1967; Price et al., 1986). The Chisos Group was produced by volcanoclastic sedimentation from the Christmas Mountains, from a source in Mexico, and by local eruptions of lava flows (Maxwell et al., 1967; Schiebout et al., 1987; Runkel, 1990).

Paleoclimates

Color-banded mudstones of the Javelina, Black Peaks, and Hannold Hill Formations are paleosols deposited in floodplains. The bands of color were created by soil-forming processes predominantly controlled by changes in the water table (Schiebout et al., 1987; Lehman, 1989, 1990). Red to gray calcareous mudstones in the Javelina and Hannold Hill Formations formed when calcium carbonate nodules developed in dry soils due to a lowered water table. Red mudstone formed when the water table dropped, allowing iron to oxidize in the mud. Black mudstone, typical of the Black Peaks Formation, formed when the water table was near the surface so that organic matter was unable to decompose. Paleontological discoveries and studies of paleosols indicate that during the Late Campanian to Paleocene period, the Big Bend area of West Texas had a semiarid to warm humid climate (Schiebout, 1987; Lehman, 1990, 1991; Lehman and Coulson, 2002).

The climate remained stable into the Eocene. In the Davis Mountains, lacustrine carbonate rocks intercalated with Eocene strata (approximate age equivalents of the Chisos

Group) lack evaporites; in addition, terrestrial gastropod fossils occur in approximately equivalent strata farther west in the Trans-Pecos region. These features indicate Trans-Pecos Texas experienced a subhumid to temperate, moist climate during the Eocene (Roth, 1984; Collinsworth and Rohr, 1986; Runkel, 1990).

Tectonics and Magmatism

Since the Cretaceous, the Big Bend area of West Texas has experienced three tectonic environments:

- **Laramide deformation** – Laramide deformation created a compressional environment that began during the last depositional stages of the Aguja Formation ~70 Ma and ceased prior to deposition of the Eocene Canoe Formation ~50 Ma. Laramide tectonism resulted from shear between the shallowly subducted, oceanic Farallon plate and the over-riding, continental North American plate. The end of Laramide deformation is marked by an unconformity at the base of the Canoe Formation (Lehman, 1991).
- **Arc magmatism** – From approximately 65 Ma to 32 Ma, widespread alkalic magmatism occurred in Trans-Pecos Texas (Figure 7). This episode represents the easternmost occurrence of continental arc magmatism generated by subduction of the Farallon plate along the west coast of North America ~1000 km away. Abundant east-northeast-trending dikes suggest that Trans-Pecos Texas experienced residual compressive stress from Laramide deformation during this period; however, the regional trend of the dikes may be controlled by pre-existing structures in the

Ouachita thrust belt, which occurs less than 1 km below the surface in this region (Price et al., 1986; Henry et al., 1991).

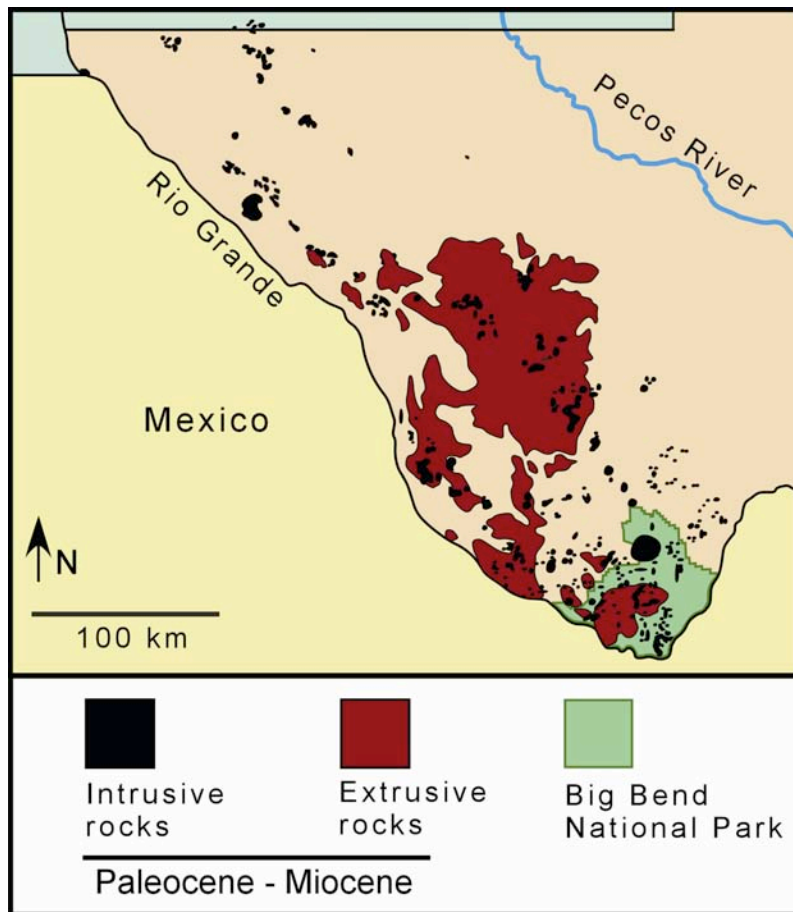


Figure 7: Regional map showing the extent of Tertiary igneous rocks formed by arc magmatism and during Basin and Range extension in Trans-Pecos Texas. Modified from Barker (1977).

- **Basin and Range** – Basin and Range extension began 31 Ma and continues today. This extensional tectonic environment was responsible for widespread regional normal faulting, silicic caldera-forming volcanism, and other ubiquitous, yet volumetrically minor, forms of alkalic magmatism. Extension is less than 10% in Trans-Pecos Texas. No magmatism younger than 17 Ma is known (Price et al., 1986; Henry et al., 1991).

Late Cretaceous volcanism

Busbey et al. (1998) and Breyer et al. (2005, and in review) described Upper Cretaceous phreatomagmatic deposits on the southern boundary of the Rosillos Mountains laccolith. These deposits represent the only Late Cretaceous igneous activity in the Big Bend area previously documented in the literature. The deposits crop out in a fault-bounded block on the southeastern flank of the Rosillos Mountains laccolith on the Pitcock Ranch (Figure 8), near the northern boundary of Big Bend National Park. The nature of the pyroclastic deposits is illustrated in Figure 9. These deposits were examined in detail during the present project, and the descriptions below come from this work together with observations reported in Breyer et al. (in review).

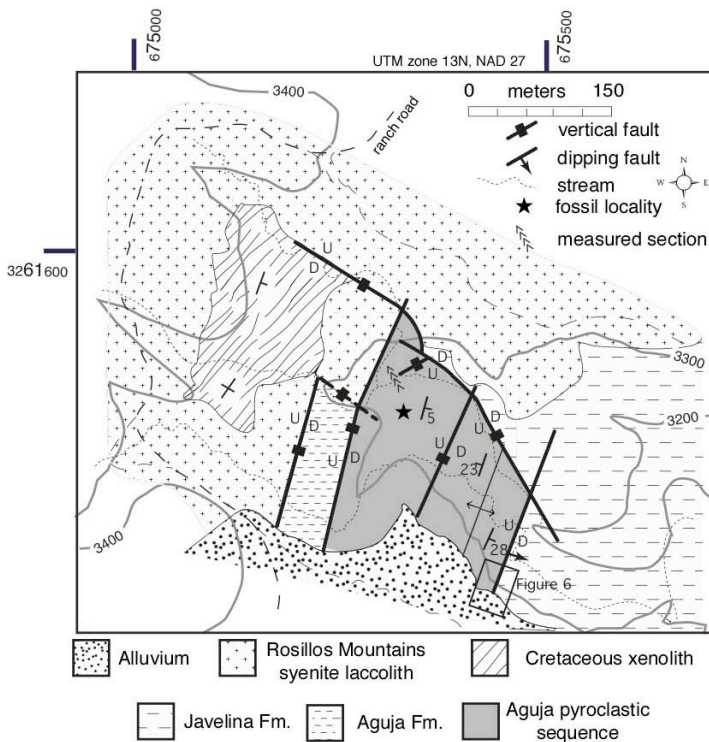


Figure 8: Geologic map of fault-bounded pyroclastic deposits on the Pitcock Ranch north of Big Bend National Park, from Breyer et al. (in review). Topographic contours shown in feet.

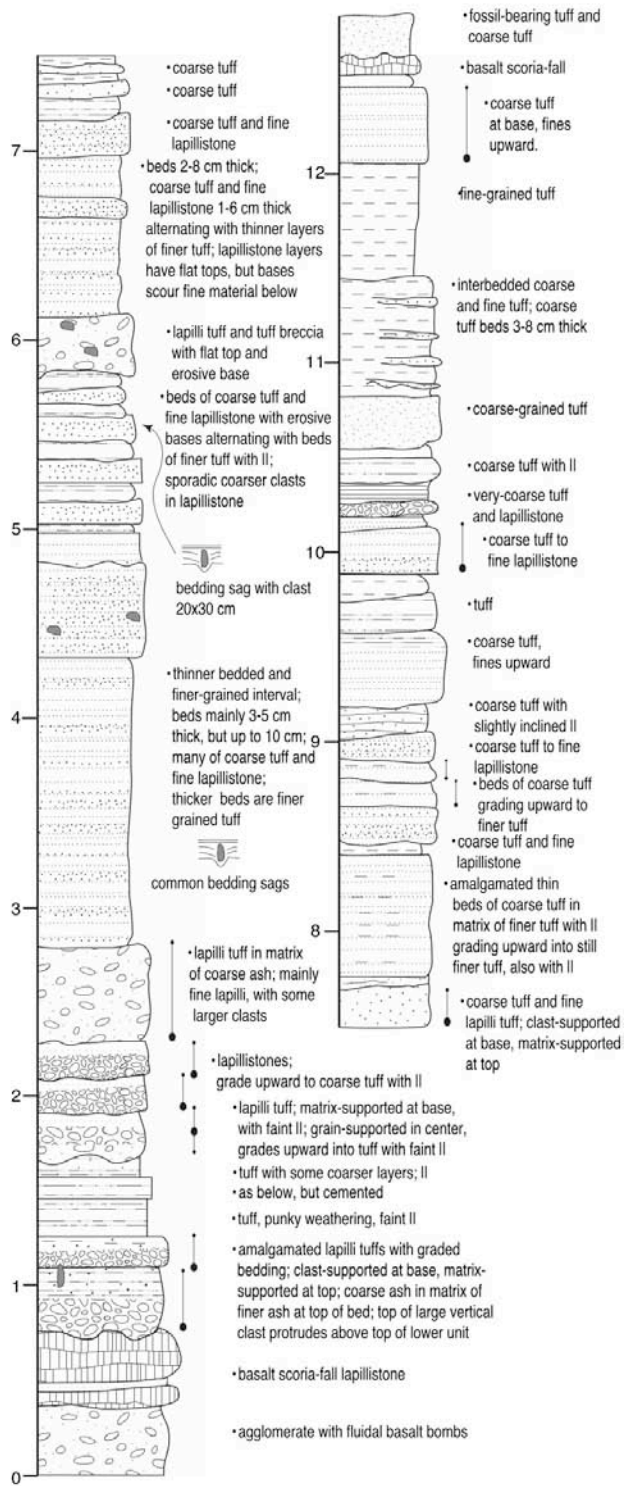


Figure 9: Measured section of pyroclastic deposits on the Pitcock Ranch north of Big Bend National Park, from Breyer et al. (in review). Vertical scale is in meters. II = parallel lamination.

A discontinuous, lenticular agglomerate composed of scoriaceous fluidal basalt bombs is located at the lowest level of exposure. The agglomerate is overlain by a well lithified, tachylite scoria lapillistone that is continuous across the fault-bounded block. The rest of the pyroclastic sequence overlies the agglomerate and lapillistone and records a shift in the style of volcanism from dominantly Strombolian to Surtseyan/phreatomagmatic eruptions. The pyroclastic deposits are composed of thin (1–10 cm) laterally continuous tuff and lapilli tuff beds with numerous blocks and bombs associated with impact sags. Basalt bombs tend to have fluidal shapes (Figure 10).



Figure 10: Fluidal basalt bomb with teardrop shape. Impact sag deforms at least four pyroclastic layers, which must have been wet and cohesive prior to impact. Axis of impact sag plunges at 46° toward 352° .

Lithic blocks are composed of gray mudstone, sandstone, felsic tuff, and basalt; ovoid mudstone blocks up to 80 cm across are flattened parallel to bedding. The abundance of

impact sags indicates the pyroclastic deposits were wet and cohesive after deposition and accumulated in a relatively near-vent environment. Highly asymmetric impact sags, like the one shown in Figure 10, can be used to triangulate the location of the vent. Unfortunately, few impact sags are exposed in three dimensions, but the example in Figure 10 suggests the vent was located to the southeast.

Tractional bed forms are rare in the pyroclastic deposits; however, antidunes, low-angle cross-bedding, and undulatory bed forms do occur. Chough and Sohn (1990) show that tractional bed forms are less common in strata within ~600 m of the vent in their study. The low number of bed forms in the pyroclastic strata on Pitcock Ranch suggests this sequence was located relatively close to the vent. This inference is consistent with the presence of ballistic blocks and bombs. Sparse carbonized wood clasts also occur in the pyroclastic strata, indicating some of the beds were deposited by dry, high-temperature base surges (Figure 11).

The uppermost part of the sequence contains petrified wood, dinosaur bone fragments, ubiquitous turtle bones, and freshwater invertebrates. These deposits are inferred to have accumulated in a pond. The deposits are constrained to be Late Campanian (to possibly early Maastrichtian) based on the turtle fossils (Busbey et al., 1998). This biostratigraphic constraint is consistent with a U–Pb SHRIMP-RG age of 72.6 ± 1.5 Ma from zircon extracted from a basalt block within the sequence (Breyer et al., 2005, and in review).



Figure 11: Clast of carbonized wood in base-surge deposit.

Chapter 3: Late Cretaceous phreatomagmatic volcanism at Peña Mountain, Big Bend National Park

Geological Setting

Cretaceous pyroclastic deposits ≤ 70 m thick occur on Peña Mountain in the southwestern portion of Big Bend National Park (Figure 12, Plate I). The pyroclastic deposits were first identified by Dr. Thomas Lehman in the 1980's while he was studying Cretaceous sedimentary rocks in the region. He interpreted the deposits to be phreatomagmatic in origin (Lehman, personal communication, 2005). The pyroclastic deposits occur within the upper shale member of the Aguja Formation and surround the Peña Mountain pluton (Plate 1). The pluton was previously described as an analcite-bearing syenodiorite sill intruded at a depth of ~ 1.5 km (Carman, 1994). However, observations from this study indicate the intrusion at least locally has discordant, high-angle intrusive contacts with the surrounding pyroclastic strata. The syenodiorite intrusion is petrographically similar to the nearby Rattlesnake Mountain sill, which has yielded a K–Ar biotite age of ~ 28 Ma (Henry et al., 1986).

At Peña Mountain, the upper shale member of the Aguja Formation is predominantly composed of gray, beige, and maroon mudstones and lenticular, cross-bedded sandstones containing limestone-cobble channel-lag conglomerates. Pyroclastic strata on the western side of Peña Mountain have a higher sedimentary component (based on visual estimation). The western contact between the upper shale member and the pyroclastic deposits is poorly exposed due to faults and the discordant intrusion of the pluton, which separates the pyroclastic strata into a northern and southern portion. Reconnaissance mapping in the Aguja Formation further west did not reveal any additional pyroclastic strata, although contact metamorphism has obscured original lithologies near the intrusion. An east-west-trending

normal fault with a down throw of ≤ 30 m to the north has been traced for ~ 300 m through the pyroclastic deposits on the northern side of Peña Mountain (Figure 12, Plate I).

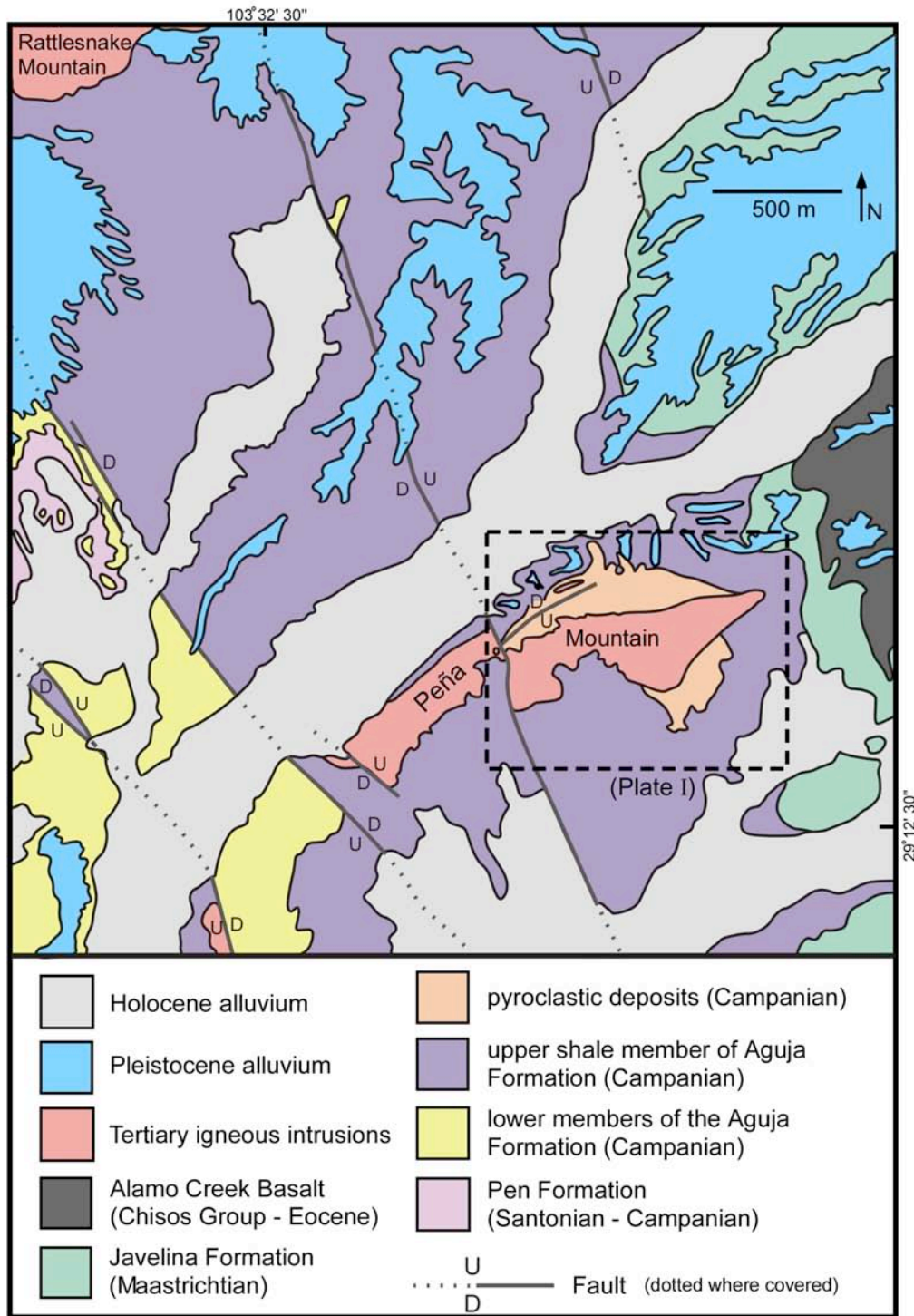


Figure 12: Geologic map of the area surrounding Peña Mountain, Big Bend National Park. Modified from Lehman (1985). Area of Plate I is indicated.

An intertonguing contact is mappable between the pyroclastic deposits and the upper shale member along the northern and eastern sides of Peña Mountain; however, the contact could only be located within a few meters because it is obscured by Pleistocene gravels (Figure 13). The lateral relations between the upper shale member and pyroclastic strata on the southern side of Peña Mountain are complicated by a volcanic crater and are described in detail in a later section.

General features of the pyroclastic strata

Pyroclastic deposits are composed of tuff, lapilli tuff, and grain-supported lapillistone (Figure 14) that are interpreted to have been deposited by air-fall and base-surge processes. There is no intravent lava lake of the type that is present in some phreatomagmatic volcanoes; however, bombs in the pyroclastic deposits are basaltic in composition. In thin section, the basalt contains euhedral olivine phenocrysts (~1–2 mm) replaced by carbonate but recognized by characteristic crystal habit. These are set in an intersertal groundmass, in which mafic minerals and glass have been altered to smectite (Figure 15). Thin-section examination of lapilli tuff shows fluidal to angular basaltic pyroclasts (Figure 16) and are set within an altered, fine-grained matrix rich in disaggregated sediment (up to 70% accidental, sand-sized quartz, feldspar, and lithic grains). It is difficult to accurately estimate the percentage of the accidental component in the pyroclastic deposits because it is difficult to discern mud from very fine-grained ash or to differentiate between igneous and detrital plagioclase derived from underlying sandstones.

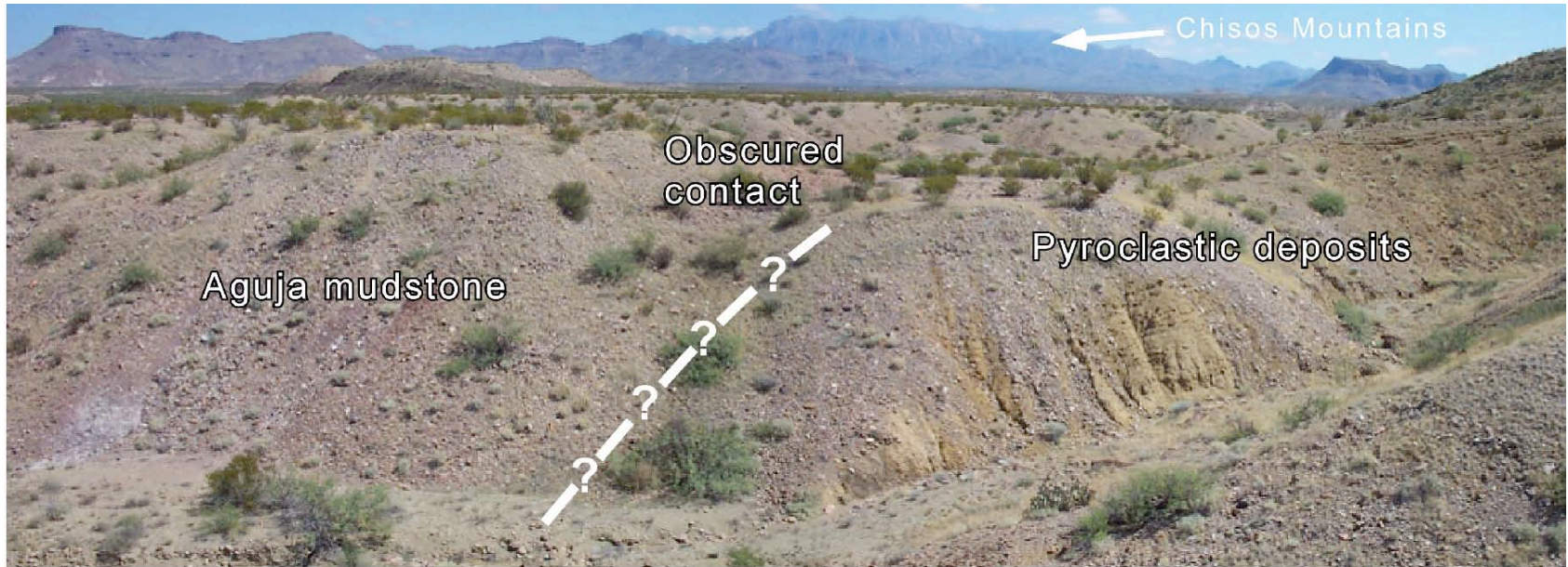
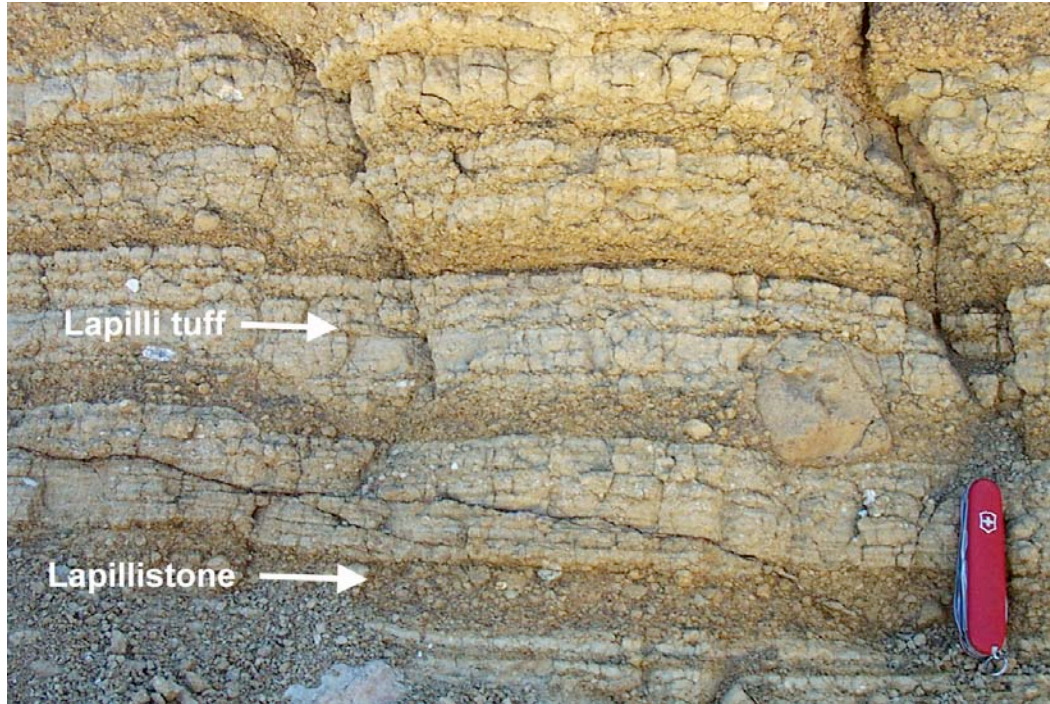


Figure 13: View looking east at the covered contact between Aguja mudstone and Upper Cretaceous pyroclastic deposits on the northeastern side of Peña Mountain. Pleistocene gravels cover the contact.

(A)



(B)



(C)



Figure 14: Typical views of pyroclastic deposits. **(A)** Alternating beds of lapillistone and lapilli tuff with an outsized clast (above and to the left of knife) draped by overlying lapilli tuff. **(B)** View of steeply dipping lapilli-tuff beds. Note the numerous mudstone clasts and single outsized basalt clast with impact sag (arrowed). The pencil is vertical. **(C)** Outcrop view of steeply dipping strata on the northern side of Peña Mountain.

Lapillistone deposits are calcite-cemented and consist of fluidal to angular basalt lapilli and less common lithic clasts. Basaltic pyroclasts are poorly to moderately vesicular and contain abundant sideromelane/palagonite altered to smectite. Quartz xenocrysts are common in basalt bombs and smaller pyroclasts. Sparse armored lapilli occur in the deposits. Scattered lithic blocks of Aguja mudstone, sandstone, and conglomerate ≤ 1 m in diameter and basalt bombs ≤ 1 m in diameter with impact sags occur within the deposits (Figure 17). Conglomerate blocks contain well-rounded paleocaliche nodules ≤ 3 cm in diameter and small amounts of plant detritus supported by a sand-sized matrix of angular to subrounded grains of quartz, feldspar, and volcanic rock fragments. Sandstone blocks contain abundant

oyster shells and are cemented by carbonate and minor amounts of oxide. Many mudstone blocks are highly flattened parallel to bedding, which indicates they were semi-consolidated when erupted.

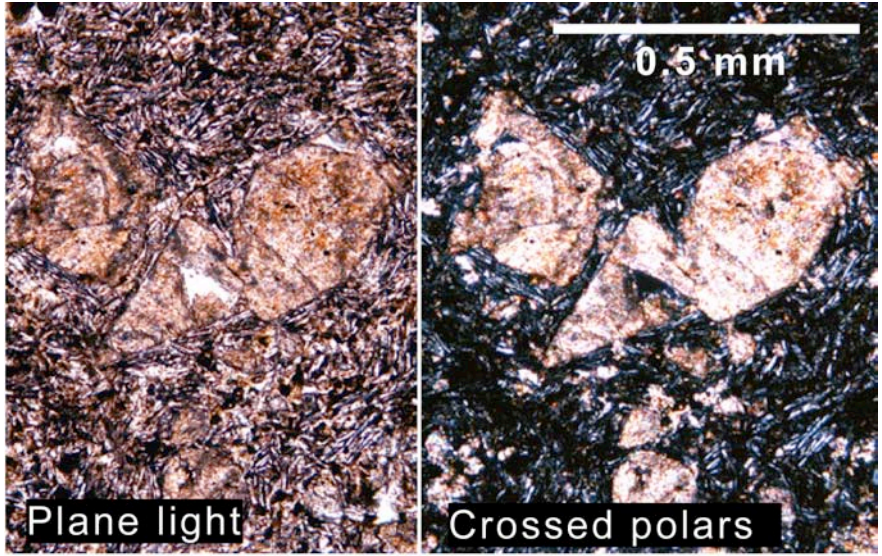


Figure 15: Photomicrographs of basalt from a bomb. Olivine phenocrysts replaced by carbonate are set in an intersertal groundmass.

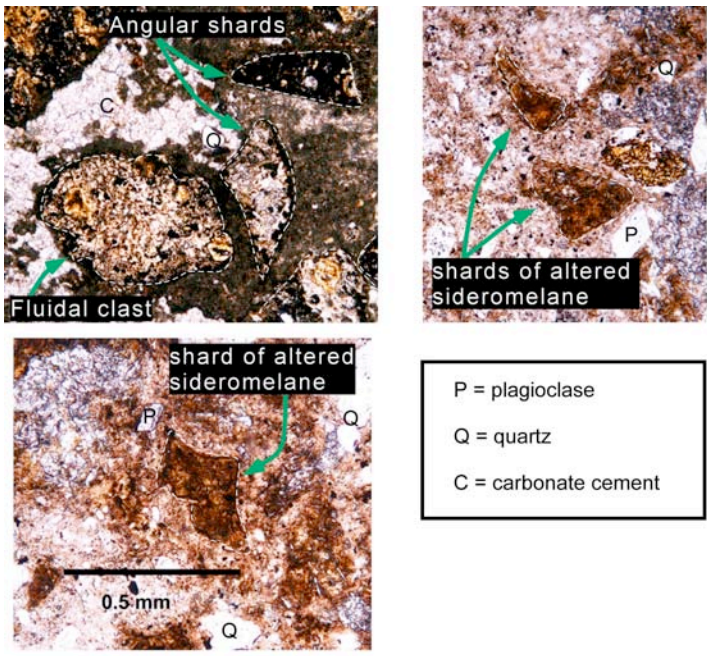


Figure 16: Photomicrographs of angular to fluidal basaltic ash particles in lapilli tuff, set within a matrix of finer ash, mud, and quartz grains. Plane light; scale is the same in each view.



(A)



(B)



(C)

Figure 17: Lithic blocks in the pyroclastic deposits at Peña Mountain. **(A)** Block of mudstone flattened parallel to bedding. Knife for scale. **(B)** Block of sandstone with oyster impressions. Hammer for scale. **(C)** Block of channel-lag conglomerate with impact sag deforming lapillistone and lapilli-tuff deposits. Knife for scale.

A centimeter-scale measured section of a typical portion of the pyroclastic strata was made on the northern side of Peña Mountain (Figure 18) to examine strata in detail and evaluate vertical facies relationships within the deposits, which may also have a bearing on lateral facies patterns (cf., Chough and Sohn, 1990). This representative section consists of the following packages comprising groups of related beds:

- **Package 1** – 20-cm-thick, clast-supported lapilli tuff with vague reverse grading and dispersed basaltic bombs and lapilli with impact sags; draped by a thin tuff bed.
- **Package 2** – 10-cm-thick, reversely graded, well-sorted, open-framework lapillistone with subrounded basalt clasts; draped by a thin tuff bed.
- **Package 3** – 3–5-cm-thick, reversely graded, well-sorted lapillistone at base; grades into a poorly sorted tuff with discrete laminae of finer ash; thin, finer grained tuff bed with a basaltic lapillus with impact sag rests with sharp base on poorly sorted tuff.

- **Package 4** – 35-cm-thick package composed of bedded tuff and lapillistone with well-defined, planar to undulatory layers; sparse lapilli with impact sags occur within the package.
- **Package 5** – 15–20-cm-thick, normally graded lapillistone (fine to medium lapilli), which gradually fines into Package 6; distinct scour features (up to 10 cm deep) at base.
- **Package 6** – 15-cm-thick, planar laminated, fine to coarse tuff.
- **Package 7** – 12-cm-thick, massive, poorly sorted lapillistone overlain by 8-cm-thick interval of poorly sorted lapilli-tuff beds with thin lapillistone interbeds.
- **Package 8** – 10-cm-thick, normally graded, open-framework lapillistone at base composed of subrounded basalt clasts; grades into 40-cm-thick, thinly bedded, fine tuff with coarse tuff to fine lapillistone interbeds; a ~10-cm-thick undulatory lapilli-tuff interbed contains a high percentage of accidental lithic clasts and one spindle-shaped mudstone block.
- **Package 9** – 20-cm-thick poorly sorted, open-framework lapillistone bed with angular to subangular basalt clasts; distinct scour features (up to 8 cm deep) at the base.

Pyroclastic deposits on the northern side of Peña Mountain

The total original thickness of the pyroclastic strata exposed on the northern side of Peña Mountain is unknown because the base of the sequence is covered and the pluton intrudes the top of the succession. A representative measured section is shown in Figure 19, where the exposed succession is > 40 m thick. The succession is thicker elsewhere on the northern side of the mountain, but some of these areas are less accessible. A truncation surface separates the pyroclastic deposits into two different sequences (cf., Leat and Thompson, 1998; Sohn and Park, 2005). The truncation surface is a well-defined angular unconformity (Figure 20). Pyroclastic strata in the sequence below the truncation surface have irregular bedding attitudes (Plate I), with dips that vary in direction and amount (cf., Leat and Thompson, 1988). Dips of up to 80° are present in places, in contrast to undeformed

tuff-ring and tuff-cone deposits, which typically have dips of $\leq 30^\circ$ (Wohletz and Sheridan, 1983).

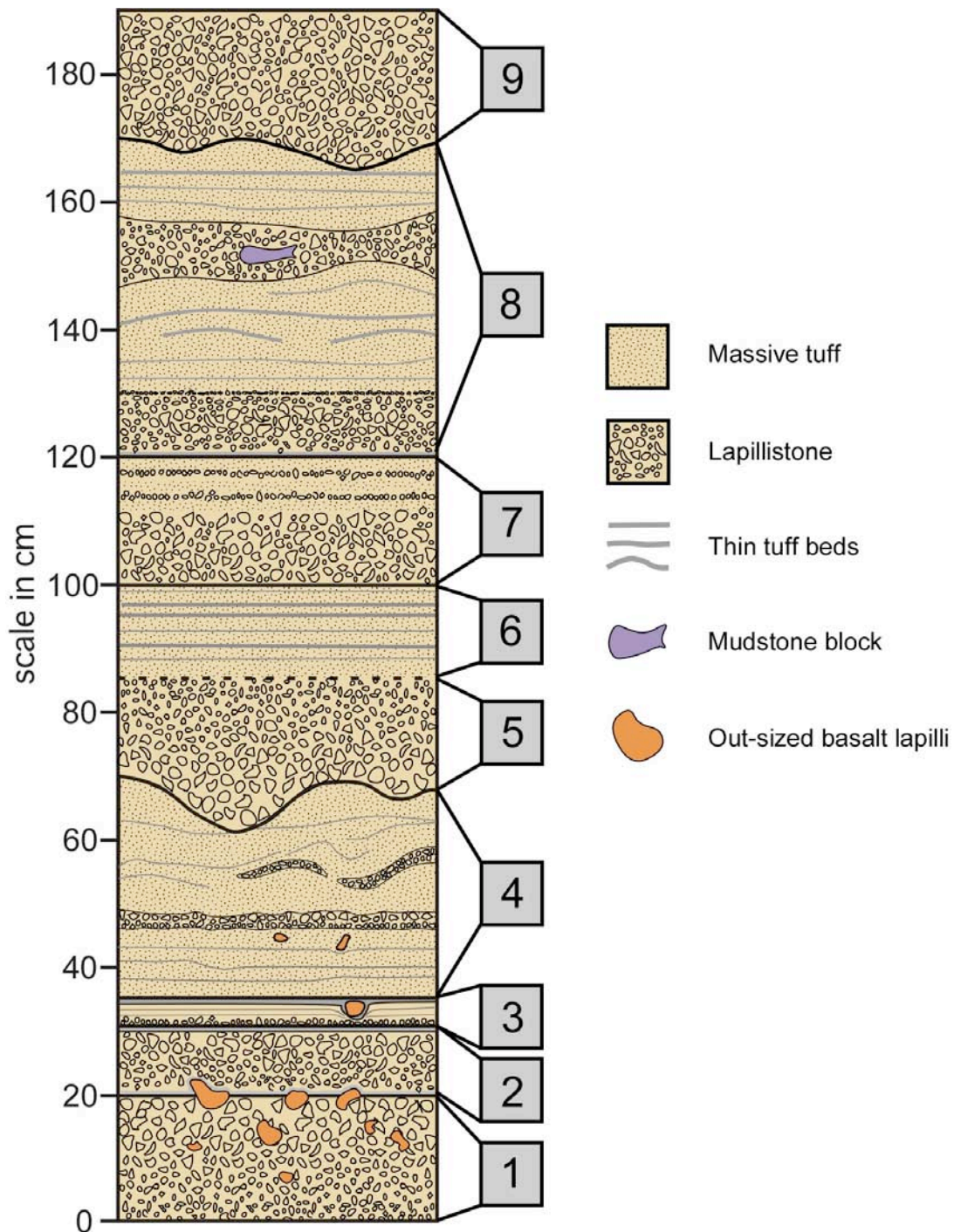


Figure 18: Centimeter-scale measured section of pyroclastic strata from the northern side of Peña Mountain, divided into packages. Location of section is labeled A in Plate I. Coarser clasts are shown to scale.

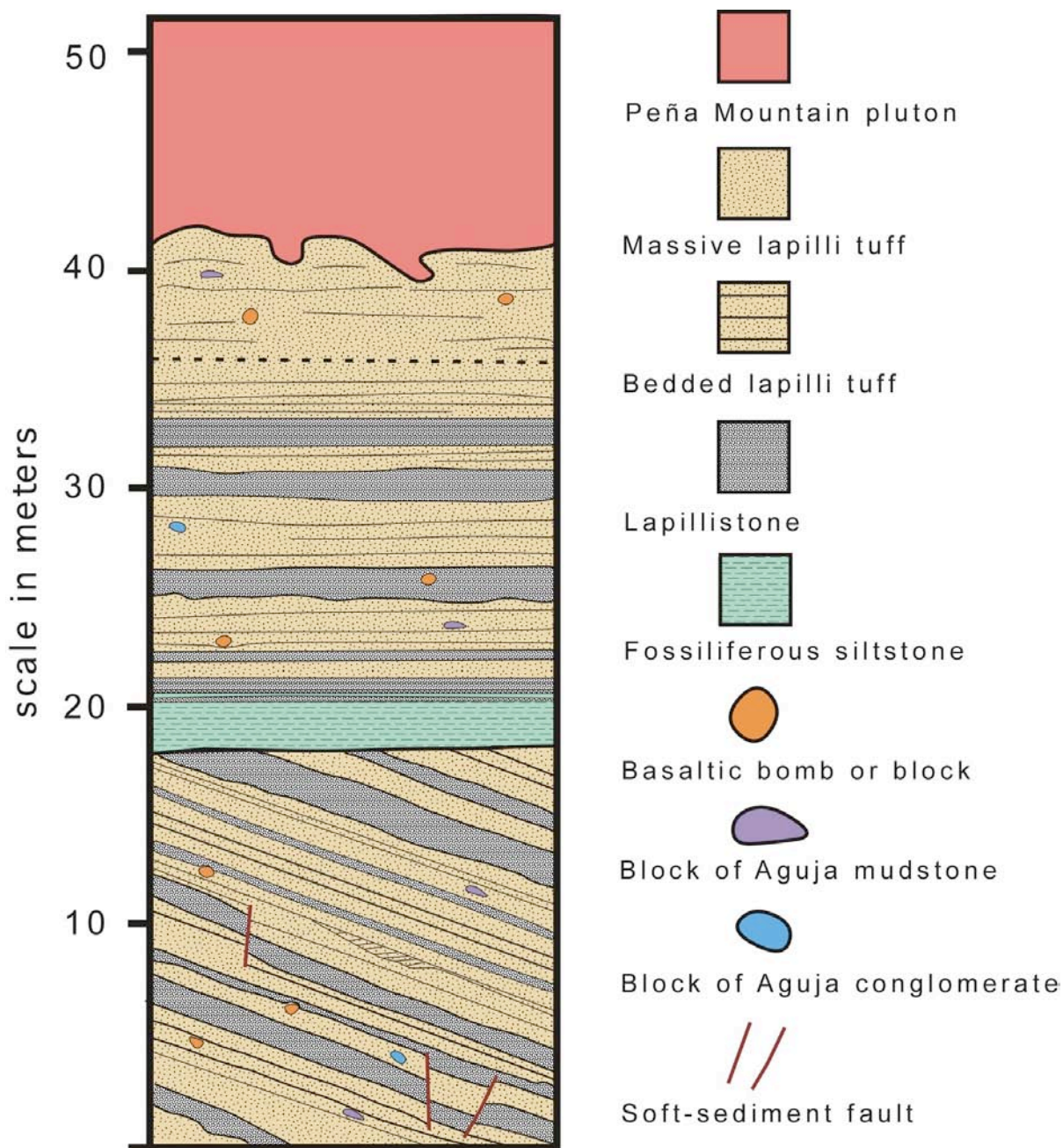


Figure 19: Measured section of lower and upper pyroclastic sequences on the northern side of Peña Mountain. Base of section is labeled point B in Plate I.

Locally abundant syndepositional normal faults with displacements from 10 cm to 2 m cut the pyroclastic deposits in the lower sequence and form minor grabens up to a few meters across (Figure 21). The amount of offset across the faults decreases upward within

individual grabens. Some faults are marked by zones up to 20 cm thick filled with disaggregated volcanoclastic material, which appears to have been injected as soft sediment. All of the small-scale normal faults terminate against the truncation surface.



Figure 20: Truncation surface (dashed) separating upper and lower pyroclastic sequences on the northern side of Peña Mountain.

A planar bedded to laminated, fine-grained sedimentary unit ≤ 2 m thick composed of alternating layers of mudstone and siltstone overlies the truncation surface (Figure 22). Some layers are calcareous and contain fossil bivalves, gastropods, and charophyte algae, pointing to a lacustrine origin. Upper portions of the lacustrine unit show increasing amounts of pyroclastic material due to renewed volcanic activity. The unit shows variable dips of $10\text{--}25^\circ$ to the southeast, which are relatively minor compared to variations in dip in the lower sequence.

The lacustrine unit is discontinuous and crops out for ~250 m on the north-central side of Peña Mountain. It forms two smaller outcrops on the northwestern side of the mountain that are each ~30 m long. Where the lacustrine unit is absent, the truncation surface is planar and is marked solely by an angular unconformity, with no evidence of faulting or sliding. In all locations the truncation surface is overlain by a second pyroclastic sequence. In some places, lapilli-tuff beds interpreted to represent base-surge deposits at the base of the second sequence show erosional scour into the lacustrine unit (Figure 23). The upper pyroclastic sequence is similar to the lower sequence, although the beds typically dip at 10–15° toward the southeast, with little variation. The uppermost 10 m of the upper sequence are altered to hornfels near the contact with the Peña Mountain pluton; however, bedding and bombs are still visible.

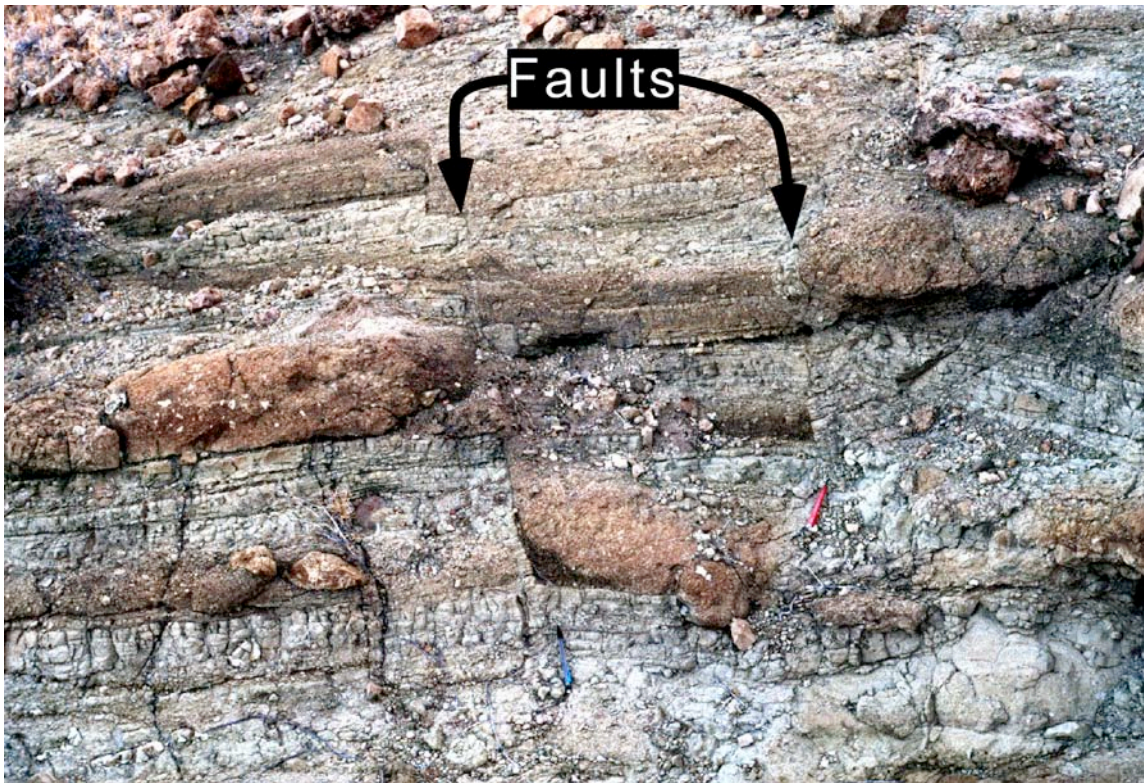


Figure 21: Syndepositional normal faults cutting pyroclastic deposits in the lower sequence. Pencils are for scale.



Figure 22: Planar bedded to laminated, calcareous lacustrine strata that mark the truncation surface in some locations.

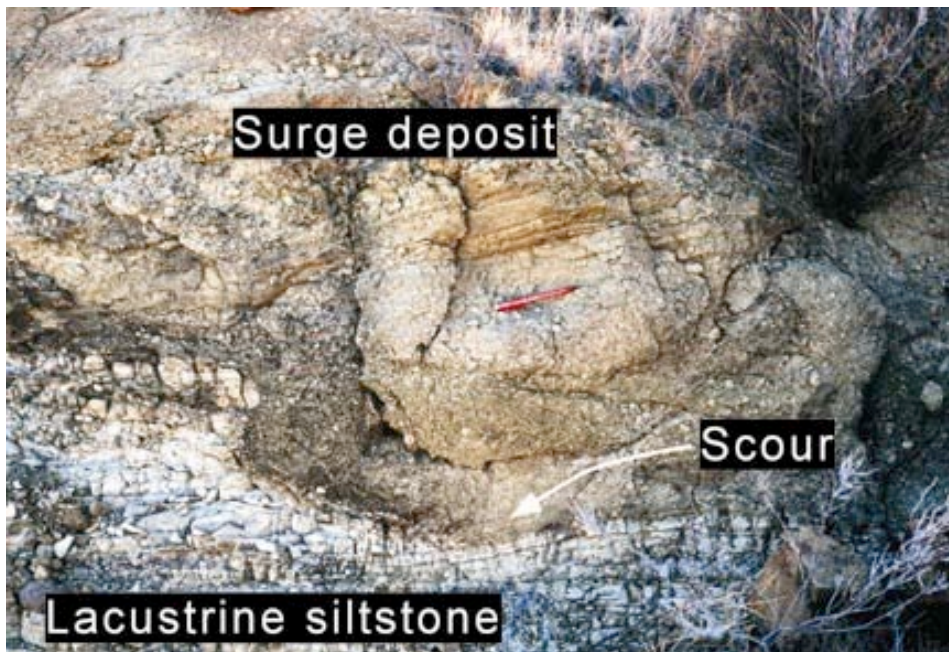


Figure 23: Bedded, lacustrine deposit overlain by a base-surge deposit at base of upper pyroclastic sequence. Note erosional scour at base of surge deposit and low-angle cross-bedding above pencil.

Fragments of non-carbonized, petrified wood ≤ 30 cm long occur sparsely throughout the pyroclastic deposits along the northern side of Peña Mountain. In addition, a trunk of an araucarioid conifer 1.2 m tall and 23 cm in diameter plunges at 43° toward 340° . Rotation of the adjacent beds to horizontal would make the trunk essentially vertical. The trunk is buried within and cuts through multiple base-surge deposits on the northwestern side of Peña Mountain (Figure 24). Dr. Thomas Lehman discovered this trunk. Its location is shown in Plate I. The roots of the petrified conifer trunk are not exposed; therefore it is impossible to resolve whether the tree is in situ. However, the tree occurs ~ 15 cm above the contact between pyroclastic strata and underlying Aguja mudstone. A fragment of petrified wood derived from the trunk is 56 cm long and 13 cm in diameter, and plunges at 4° toward 247° . The fragment is a portion of a larger fragment that was at least 2 m long but has weathered away, leaving an impression that lies on a bedding plane above the exposed base of the trunk.

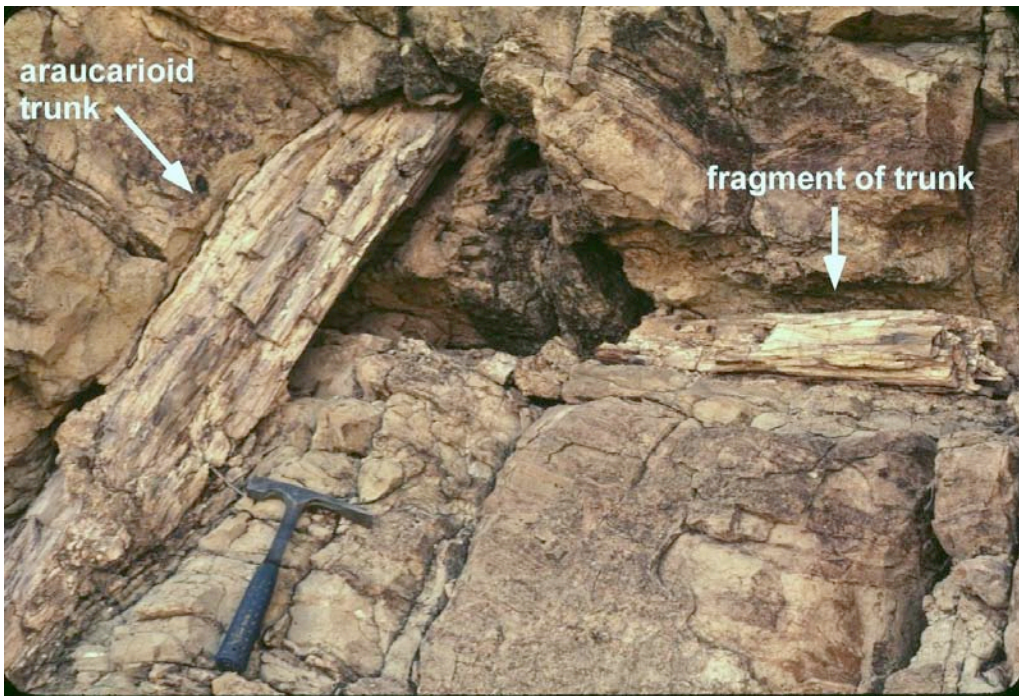


Figure 24: Araucarioid trunk in pyroclastic strata on the northwestern side of Peña Mountain. The fragment broken from the trunk is aligned southwest-northeast (west is to the right in this view). Photograph from Thomas Lehman.

Pyroclastic deposits on the southern side of Peña Mountain

Pyroclastic deposits on the southern side of Peña Mountain are predominantly composed of lapillistone, lapilli tuff, and tuff similar to those on the northern side; massive layers rich in bombs and blocks are also present. A zone of strongly disturbed pyroclastic deposits and nonvolcanic Aguja strata ≤ 60 m across marks the outer edge of the pyroclastic deposits to the south and southeast (Figures 25 and 26). Spatial and stratigraphic relationships between less disturbed pyroclastic strata, the intensely disturbed zone, and undisturbed nonvolcanic Aguja strata described below suggest the deposits are remains of a crater wall and crater-filling tephra.

Less disturbed pyroclastic sequence. Less disturbed pyroclastic strata ≥ 65 m thick are exposed on the southern side of Peña Mountain, below the contact with the syenodiorite intrusion. The strata typically dip at $25\text{--}60^\circ$ to the north (toward the intrusion), and stratigraphically higher deposits generally have steeper dips. A characteristic section of the less disturbed pyroclastic deposits on the southern side of Peña Mountain is shown in Figure 27. The lowest pyroclastic unit (unit *a* in Figure 27) is a 30-cm-thick lapilli tuff that is generally massive to planar bedded and rests upon disturbed Aguja mudstone. The basal 5 cm of the lapilli tuff contains up to 40% randomly oriented, angular mudstone clasts (Figure 28) derived by erosional scour of the underlying Aguja mudstone. Upper portions of the lapilli-tuff bed contain decreasing percentages of accidental lithic clasts and show poorly defined, low-angle cross-bedding. The lapilli tuff is overlain by a diffusely bedded, open-framework lapillistone ~ 4 m thick (unit *b* in Figure 27) containing sparsely to moderately

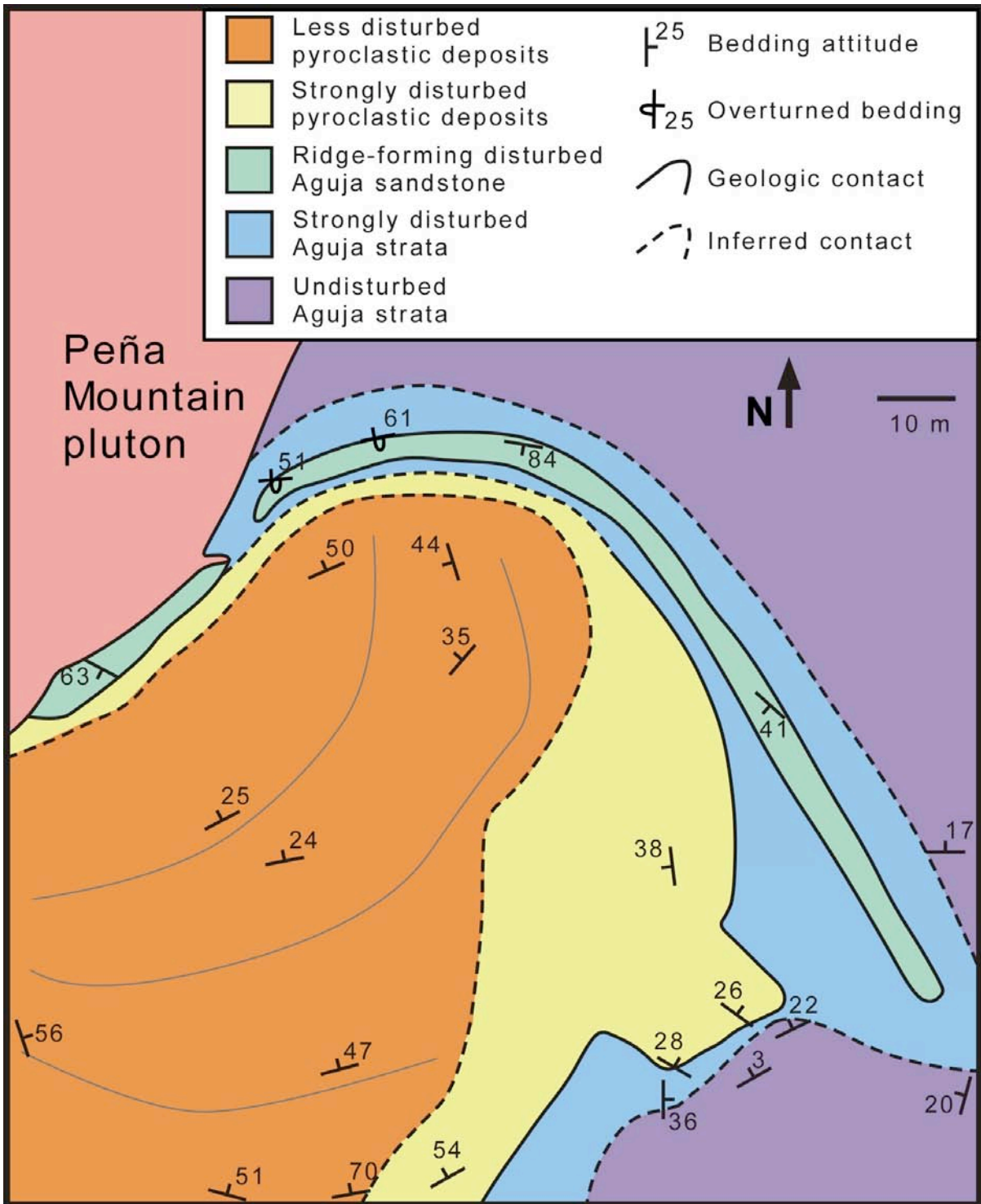


Figure 25: Tape-and-compass map of part of the southeastern side of Peña Mountain. Note the arcuate trend of the disturbed zone defined by the ridge-forming sandstone. Gray lines represent typical trends of less disturbed pyroclastic strata (see text for discussion). Location shown in Plate I.

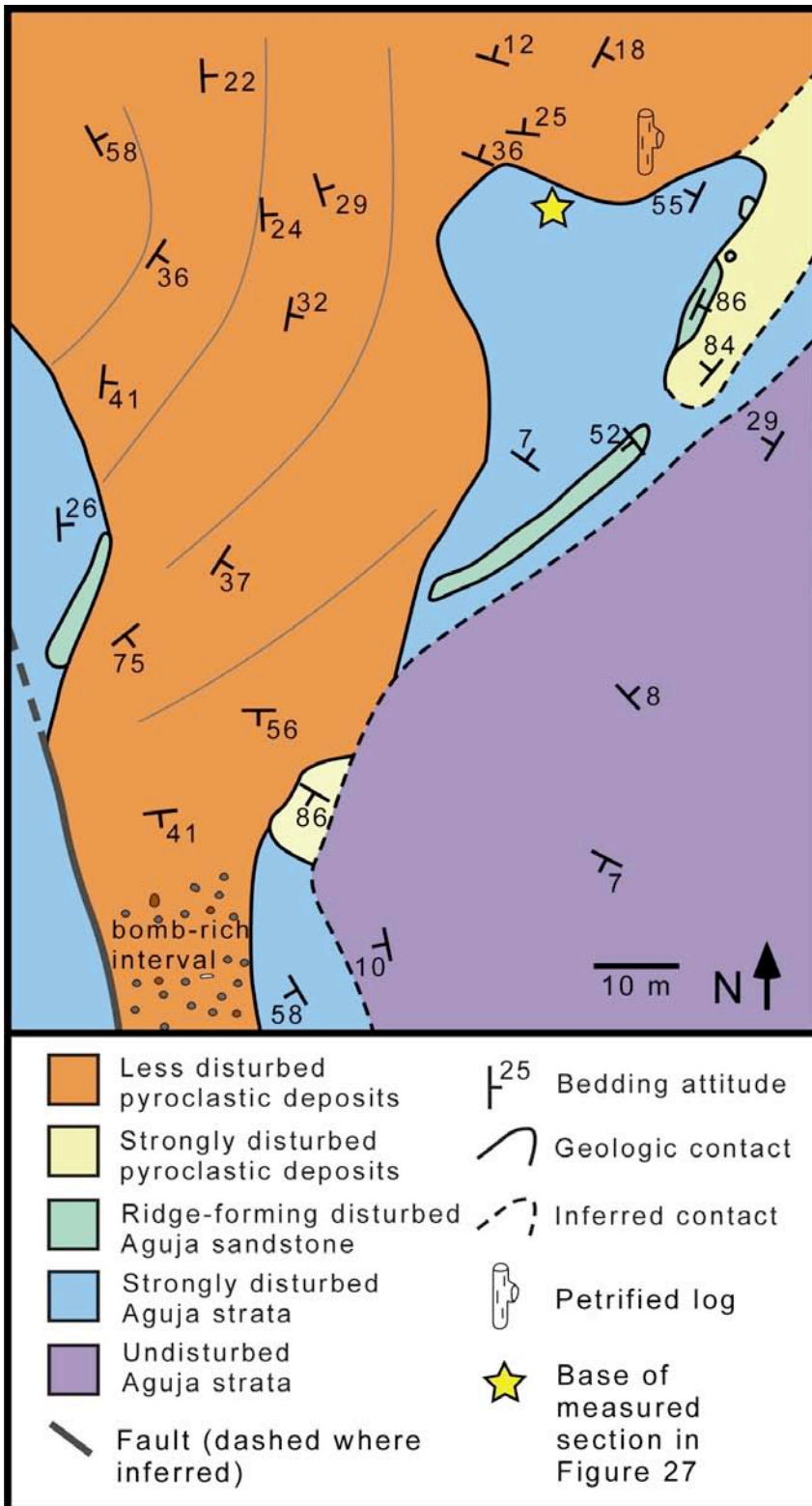


Figure 26: Tape-and-compass map of part of the southern side of Peña Mountain. Location of the measured section in Figure 27 is indicated. Gray lines represent typical trends of less disturbed pyroclastic strata. Location shown in Plate I.

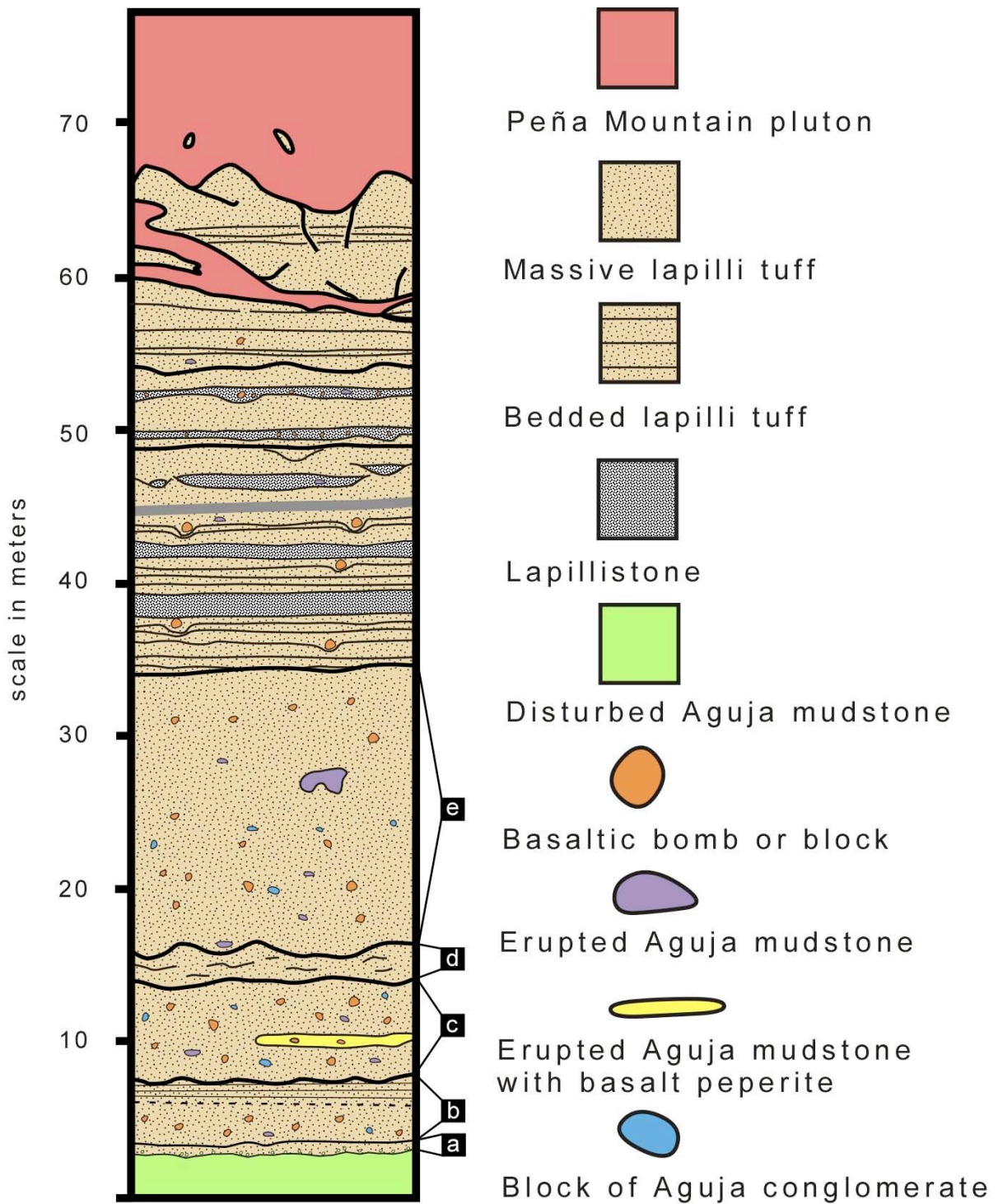


Figure 27: Measured section of less disturbed pyroclastic strata on the southern side of Peña Mountain. Small letters refer to individual units that are discussed in the text. Base of section is shown in Figure 26 and is labeled C in Plate I. Coarser clasts are shown schematically, as are beds in the upper 35 m of the section.

vesicular basalt clasts and up to 15% white mudstone clasts ≤ 2 cm in diameter. A flat-lying, non-carbonized, petrified log 30 cm in diameter occurs ~ 20 m along strike to the east in this lapillistone unit (Figure 26). The lapillistone grades into a 7-m-thick, massive, very poorly sorted, matrix-supported lapilli tuff (unit *c* in Figure 27) containing up to 50% accidental lithic clasts, as well as abundant blocks and bombs. Angular blocks of sandstone ≤ 30 cm across are present, together with partially broken and flattened blocks of mudstone with irregular margins. Basalt blocks and bombs are typically ≤ 10 cm across. A 3-m-long tabular mass of white mudstone containing fluidal to subangular basalt clasts is also present within this interval (Figure 29). Basalt clasts up to 10 cm in diameter in this mass have fluidal margins with millimeter-scale irregularities (Figure 30).

This thick, massive, block-and-bomb-rich unit is overlain by an interval 1–2 m thick of planar bedded lapilli tuff with sparse low-angle cross-bedding (unit *d* in Figure 27), which in turn is overlain by a 19-m-thick, poorly exposed, massive, matrix-supported lapilli tuff containing 5% blocks and poorly vesicular cauliflower bombs up to 1 m in diameter associated with impact sags (unit *e* in Figure 27). One bomb shows evidence of having broken upon impact with the ground (Figure 31).

The upper 35 m of the undisturbed pyroclastic sequence on the southern side of Peña Mountain consist of monotonous, planar bedded, fine lapilli tuff intercalated with tuff with sparse impact sags. Open-framework lapillistone beds 15–30 cm thick, which show basal scour, become more abundant in the upper portions of the section. Basalt bombs and blocks of Aguja channel-lag conglomerate are locally abundant in the lapillistone; however, mudstone blocks are sparse ($< 10\%$). Dark, chilled, aphanitic dikes from the Peña Mountain pluton intrude the upper portions of the sequence near the intrusive contact.



Figure 28: Lapilli tuff overlying disrupted Aguja mudstone along an erosional contact.



Figure 29: Tabular mass of erupted mudstone mixed with fluidal basalt clasts.



Figure 30: Close-up of fluidal basalt clasts within tabular mass of erupted mudstone. Field of view is 27 cm across.



Figure 31: Basaltic cauliflower bomb, ~1 m across, with irregular lower contact that formed as the bomb shattered upon impact.

Strongly disturbed zone. Less disturbed pyroclastic deposits on the southern side of Peña Mountain are rimmed by zones of strongly disturbed pyroclastic and nonvolcanic Aguja strata, which have a total width of 60 m. Figures 25 and 26 show two tape-and-compass maps of the disturbed zone, which separates less disturbed tephra described earlier and undisturbed Aguja strata. Both pyroclastic and nonvolcanic strata in the strongly disturbed zone form laterally discontinuous beds that can be traced for only a few meters and are marked by small faults and disharmonic soft-sediment folding with wavelengths of 1–2 m. Depositional contacts between disturbed pyroclastic strata and underlying, more steeply dipping sandstone bodies occur locally (Figure 32), showing that some of the disruption and rotation of the sandstone occurred prior to deposition of the pyroclastic strata.

In the southeastern part of Peña Mountain (Figure 25), the strongly disturbed zone follows an arcuate trend surrounding less disturbed pyroclastic strata. The trend of the strongly disturbed zone is best marked by a continuous, erosion-resistant, cross-bedded sandstone ≤ 3 m thick that has steep to overturned dips (Figures 25 and 33). Undisturbed Aguja sandstone strata nearby typically have relatively shallow dips ($< 30^\circ$).

A less regular contact relationship is shown in Figure 26. Disturbed, erosion-resistant Aguja sandstones mark the strongly disturbed zone in this location as well; however, here the sandstones form discontinuous bodies with generally steep to subvertical dips. The field relationships within the strongly disturbed zone are complex. Small masses of disturbed Aguja strata are intermixed with strongly disturbed pyroclastic deposits, which are in contact with less disturbed pyroclastic and nonvolcanic strata. In one location, less disturbed pyroclastic strata are in direct contact with undisturbed Aguja deposits. In the western part of

the area shown in Figure 26, a late, high-angle, brittle fault juxtaposes less disturbed pyroclastic deposits and disturbed Aguja strata.

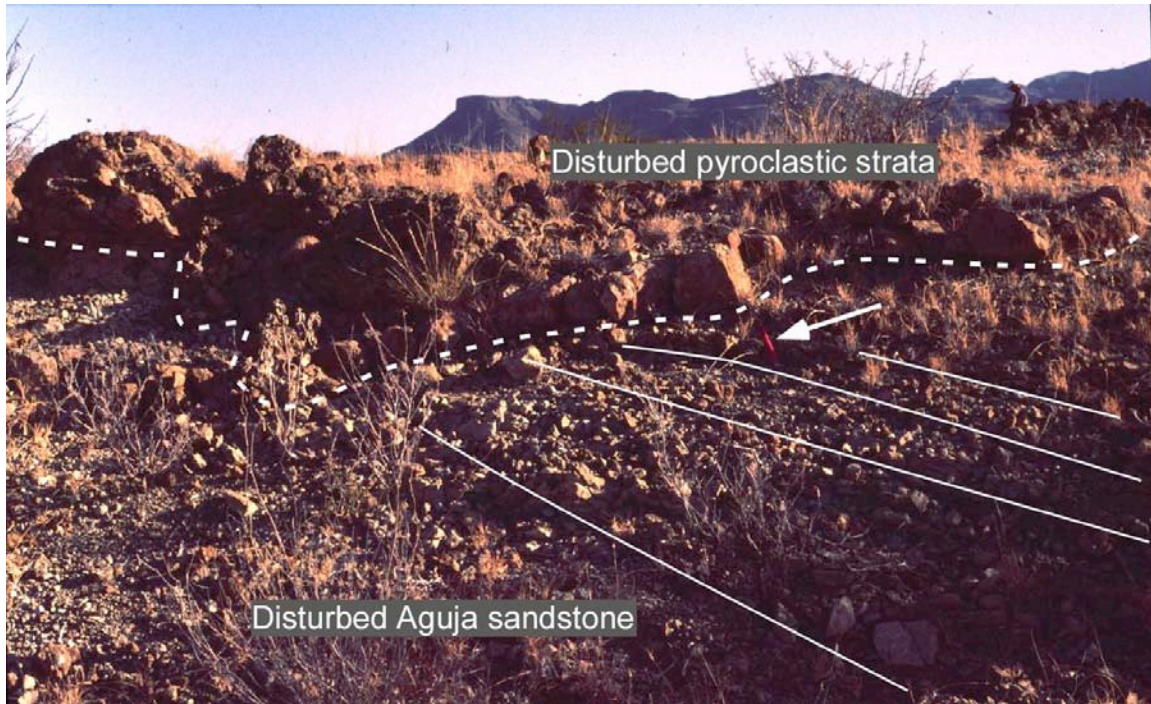


Figure 32: Irregular depositional contact (dashed) between strongly disturbed pyroclastic strata and more steeply dipping, disrupted Aguja sandstone. Solid white lines approximate bedding planes in sandstone. Pencil (arrowed) for scale.

Geochemistry

Three basalt bombs were collected from pyroclastic deposits at Peña Mountain for major- and trace-element geochemistry. Sample B4 was collected in the lower pyroclastic sequence on the northern side of Peña Mountain, whereas samples C29 and C30 were collected within 5 m of one another from a single horizon in the less disturbed pyroclastic strata on the southern side of Peña Mountain. Sample A19c was collected from a bomb within the Upper Cretaceous pyroclastic strata located on the Pitcock Ranch and was analyzed for comparison with the Peña Mountain samples. Data are shown in Table 2.

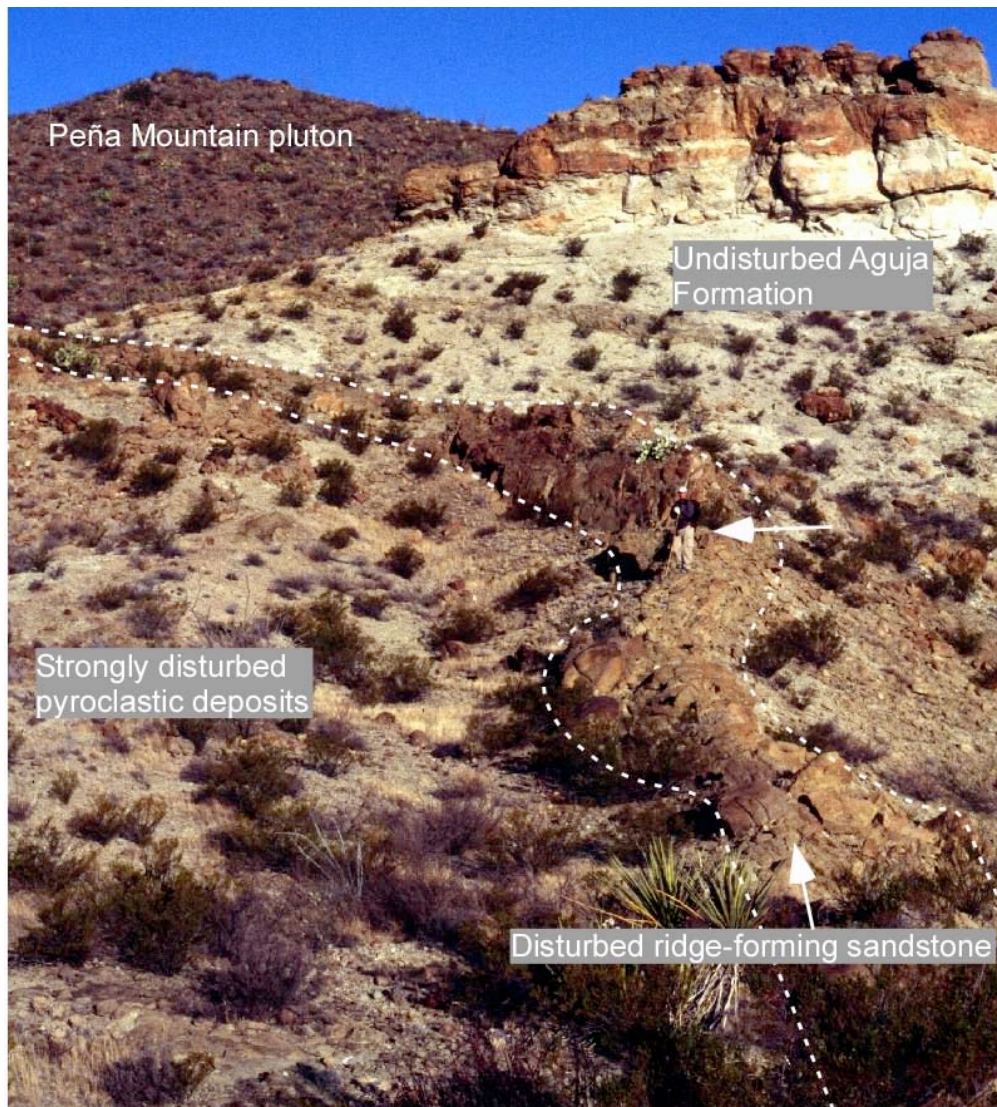


Figure 33: Ridge-forming disturbed Aguja sandstone mass (outlined) that rims the northeastern portion of the strongly disturbed pyroclastic strata on the southern side of Peña Mountain. Author (arrowed) for scale. View is toward the north.

The three samples from Peña Mountain plot in the basalt (B4), tephrite/basanite (C29), and basaltic trachyandesite (C30) fields on the TAS diagram (Figure 34). This classification cannot be rigorously accepted due to the high degree of alteration evident in thin section in each sample, which likely led to significant amounts of major-element

Table 2: Geochemical data for volcanic samples.

Normalized major elements (wt. %)*					CIPW norms				
	B4	C29	C30	A19c		B4	C29	C30	A19c
SiO ₂	46.61	48.65	54.77	43.41	Q	-	-	-	-
TiO ₂	1.482	1.546	1.606	3.538	or	1.83	9.46	9.10	0.04
Al ₂ O ₃	19.35	18.15	20.93	17.66	ab	15.56	9.66	45.66	17.93
FeO	7.30	2.59	3.84	14.29	an	32.90	19.62	29.93	25.19
MnO	0.133	0.097	0.098	0.24	ne	10.96	20.48	1.44	13.76
MgO	3.74	1.82	3.33	4.83	di	27.71	11.86	5.03	17.30
CaO	15.34	19.29	7.53	10.16	wo	-	23.81	-	-
Na ₂ O	4.23	5.61	5.71	5.12	ol	4.08	-	6.58	15.81
K ₂ O	0.31	1.60	1.54	0.06	mt	2.15	2.24	2.33	5.13
P ₂ O ₅	1.499	0.638	0.639	0.702	il	2.81	2.94	3.05	6.72
LOI	10.54	12.50	5.93	9.76	ap	3.47	1.48	1.48	1.63
Total**	88.00	85.90	92.31	86.64	Total	101.50	101.50	101.60	103.50
					AN	67.89	66.99	37.1	58.42

Trace elements (ppm)									
	B4	C29	C30	A19c		B4	C29	C30	A19c
Ni	130	117	123	303	Er	4.97	3.10	3.33	2.35
Cr	330	322	366	748	Tm	0.69	0.41	0.43	0.30
V	210	160	242	304	Yb	4.21	2.38	2.45	1.73
Ga	18	14	18	24	Lu	0.65	0.36	0.36	0.25
Cu	40	75	97	90	Ba	403	740	913	266
Zn	99	28	46	123	Th	2.59	2.60	2.89	3.61
Bi	0	0	0	3	Nb	10.03	9.27	11.01	34.86
La	39.74	32.94	34.70	28.86	Y	55.82	36.04	36.09	24.00
Ce	72.62	68.53	69.47	58.20	Hf	2.93	2.39	3.20	4.80
Pr	8.68	8.79	8.42	7.35	Ta	0.63	0.61	0.70	2.27
Nd	37.78	38.72	36.73	32.58	U	38.55	1.17	0.94	1.05
Sm	8.44	9.06	8.51	7.81	Pb	6.84	10.42	7.38	4.13
Eu	2.58	2.62	2.54	2.65	Rb	1.9	21.5	24.1	1.2
Gd	8.78	8.53	8.15	6.77	Cs	0.15	0.32	0.34	0.17
Tb	1.43	1.23	1.24	0.99	Sr	969	938	1122	500
Dy	8.91	6.77	7.11	5.40	Sc	36.9	31.9	47.7	29.8
Ho	1.86	1.25	1.36	0.95	Zr	100	79	107	178

*Normalized to 100% on a volatile-free basis.

**Total before normalization.

mobility. Furthermore, loss on ignition (LOI) values are high in each sample (Table 2), which is consistent with extensive secondary alteration. All of the samples are nepheline normative; however, data are not plotted on CIPW diagrams or major-element variation

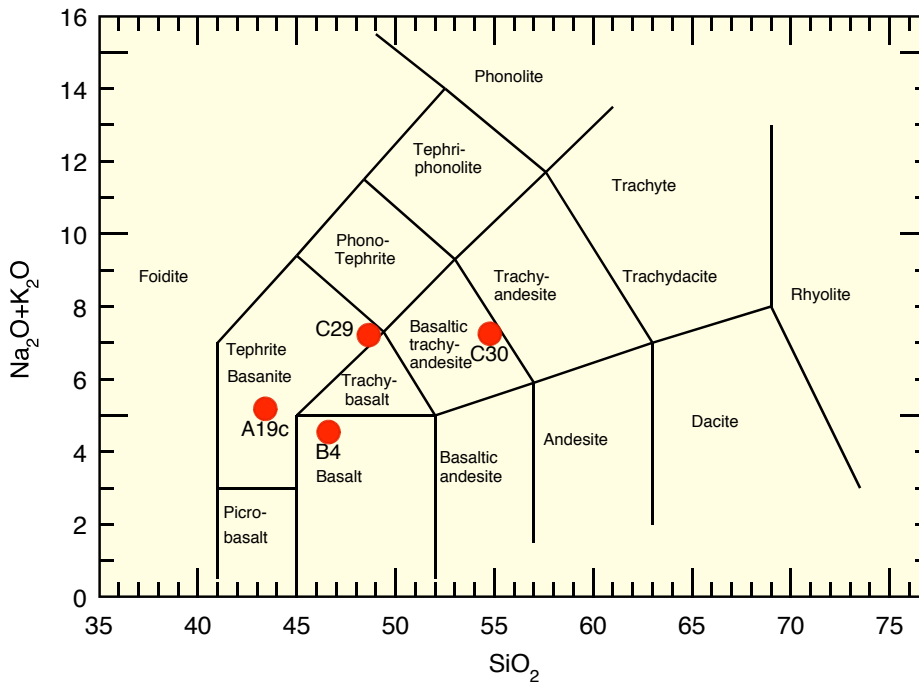


Figure 34: Analyses of basalt bombs plotted on total alkalis vs. silica (TAS) diagram (Le Bas et al., 1986).

diagrams due to the high degree of alteration and small number of samples that were collected. Sample C30 appears the least altered in this section and has the lowest LOI value. Therefore, it is reasonable to conclude that this analysis is closest to the original magmatic composition. The samples are more tightly clustered and plot in the subalkaline basalt field on the Zr/TiO_2 vs. Nb/Y trace-element discrimination diagram (Figure 35), which uses elements generally considered to be immobile during low-temperature alteration (Winchester and Floyd, 1977). The samples tend to plot within arc or MORB fields in several standard trace-element discrimination diagrams using supposedly immobile trace elements (Figures

36, 37, 38). However, the samples plot in the field for alkaline ocean-island basalt in Figure 36B and in the alkali basalt field in Figure 37B. The samples clearly do not have affinities with MORB, as shown in Figures 39, 40, and 41. They do not show the depletion in LIL elements that is typical of MORB, and they show significant LREE enrichment, again dissimilar to MORB (Figure 39). They also show negative anomalies in HFSE (especially Ta, Nb) (Figures 40 and 41). This feature is typical of arc basalts; however, similar negative HFSE anomalies occur in some intraplate basalts and are interpreted to indicate significant interaction between the magma and continental lithosphere (Wilson, 1989).

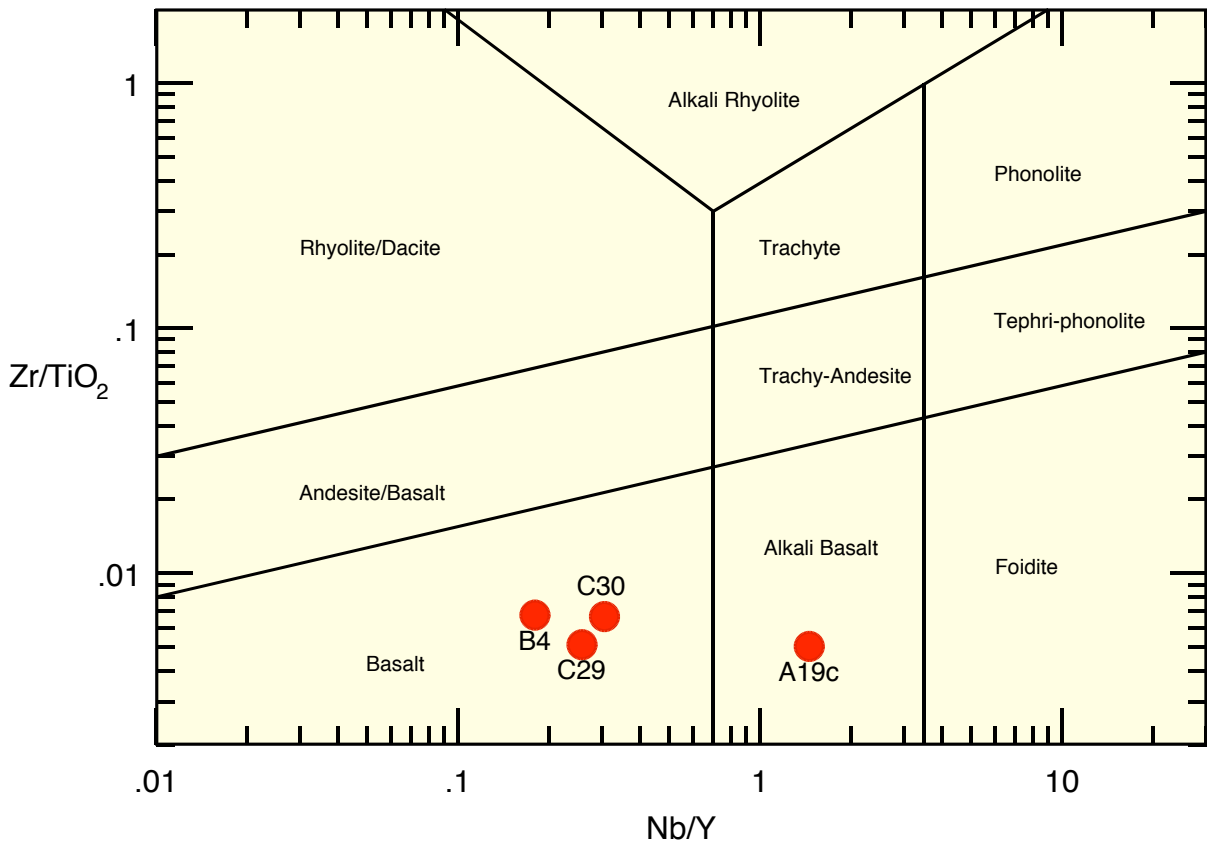


Figure 35: Analyses of basalt bombs plotted on Zr/TiO₂ vs. Nb/Y discrimination diagram (Winchester and Floyd, 1977; revised by Pearce, 1996).

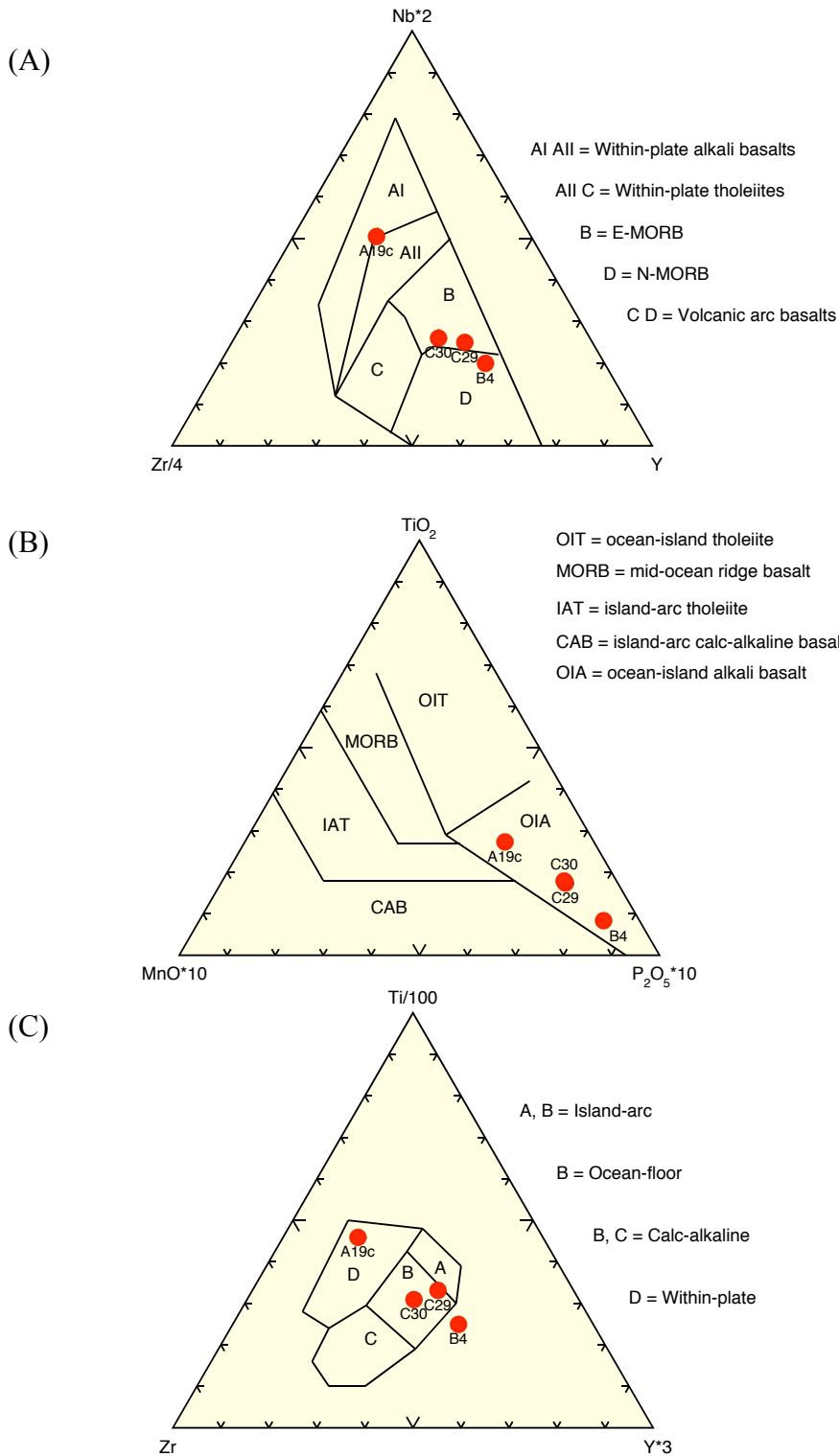


Figure 36: Analyses of basalt bombs plotted on standard trace-element discrimination diagrams. A from Meschede (1986), B from Mullen (1983), C from Pearce and Cann (1973).

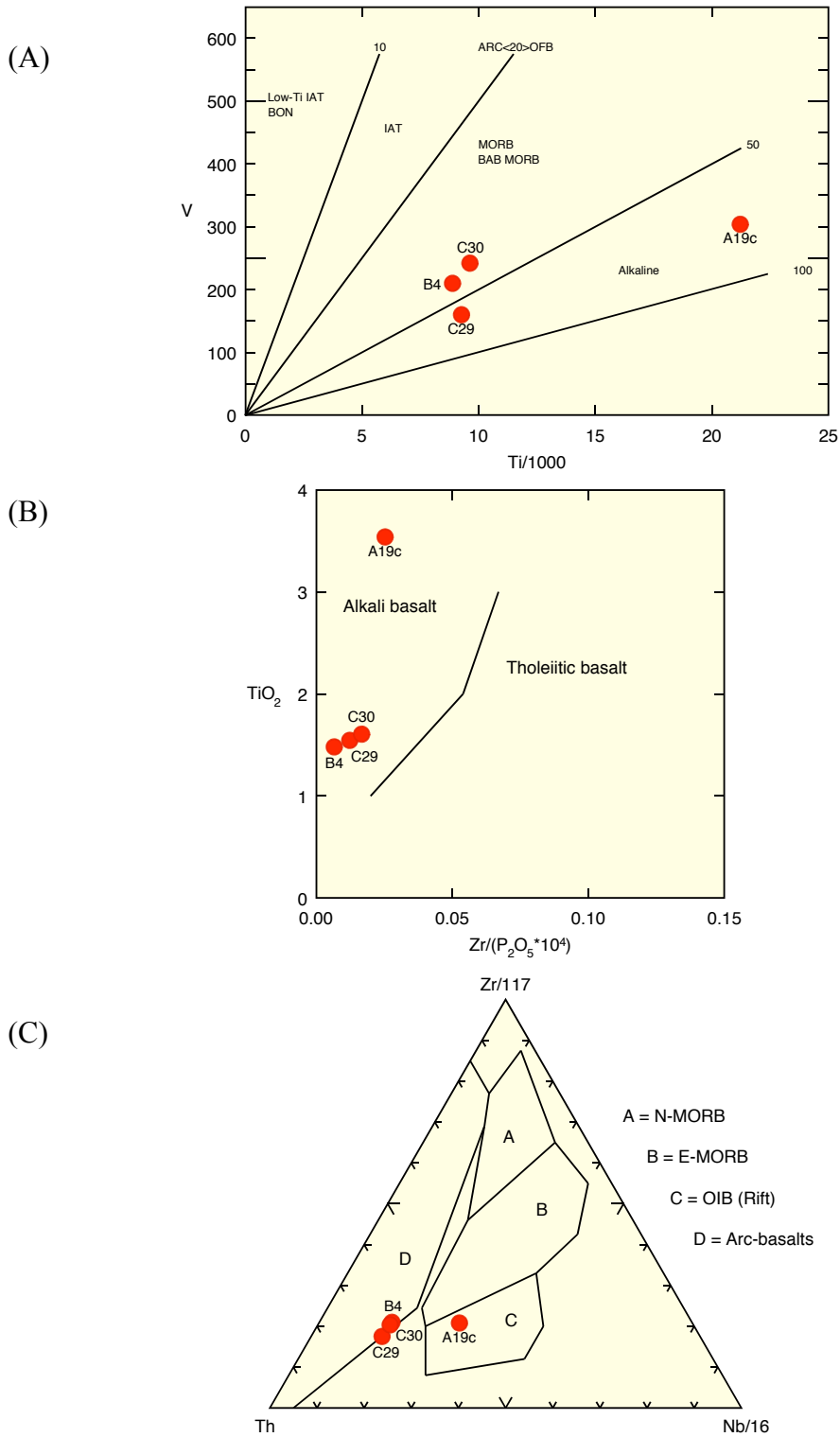


Figure 37: Analyses of basalt bombs plotted on other standard discrimination diagrams. A from Shervais (1982), B from Winchester and Floyd (1976), C from Wood (1980).

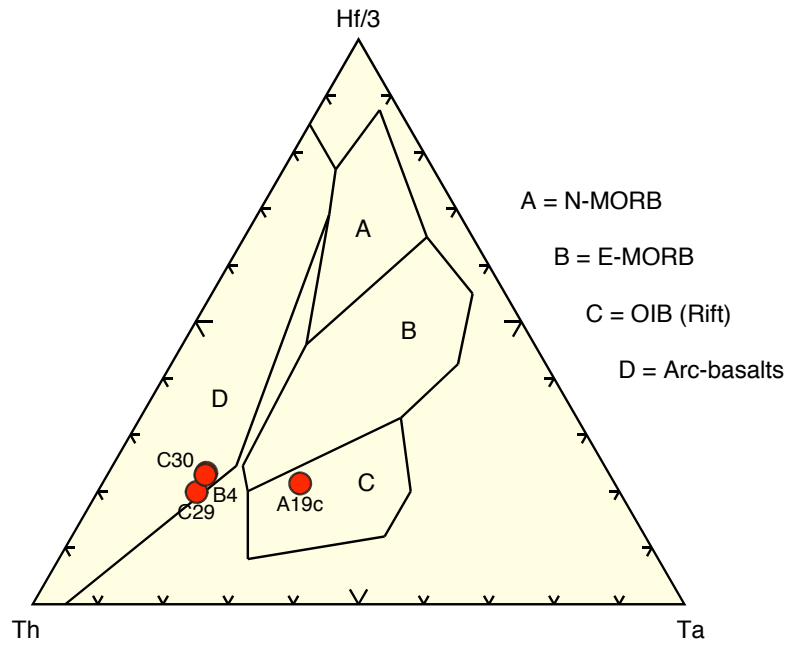


Figure 38: Analyses of basalt bombs plotted on Th–Hf–Ta discrimination diagram from Wood (1980).

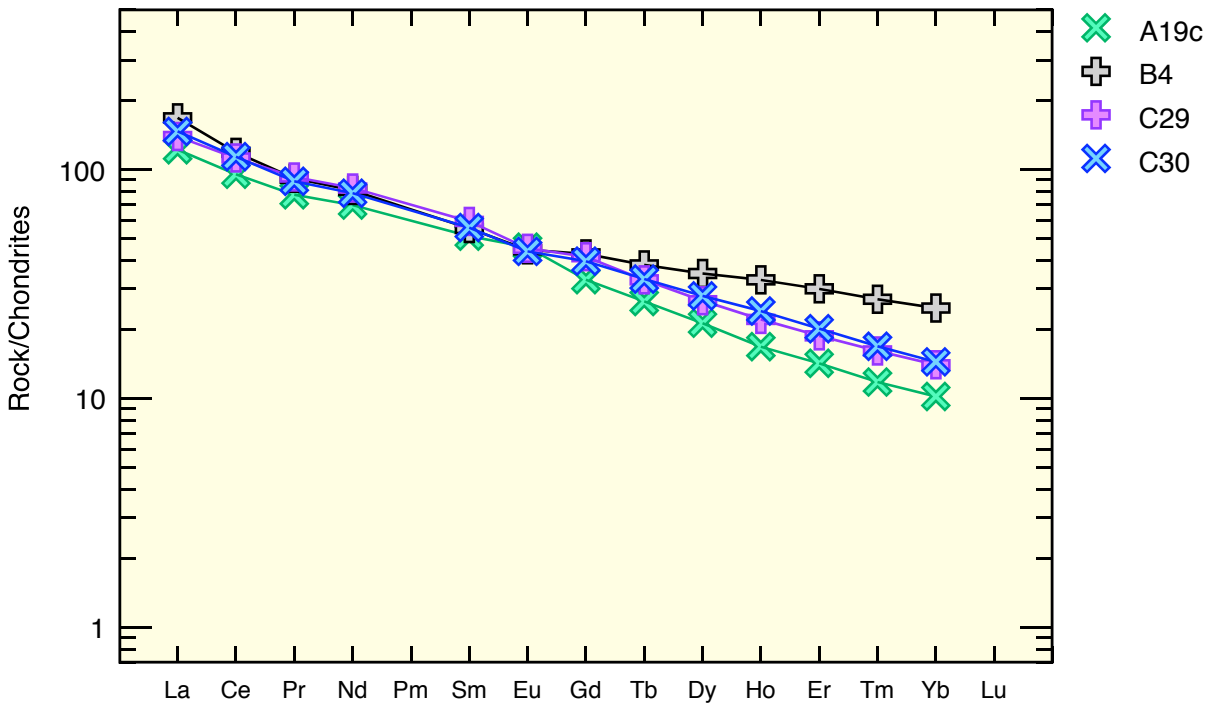


Figure 39: Chondrite-normalized REE patterns for samples of basalt bombs. Normalizing values from Sun and McDonough (1989).

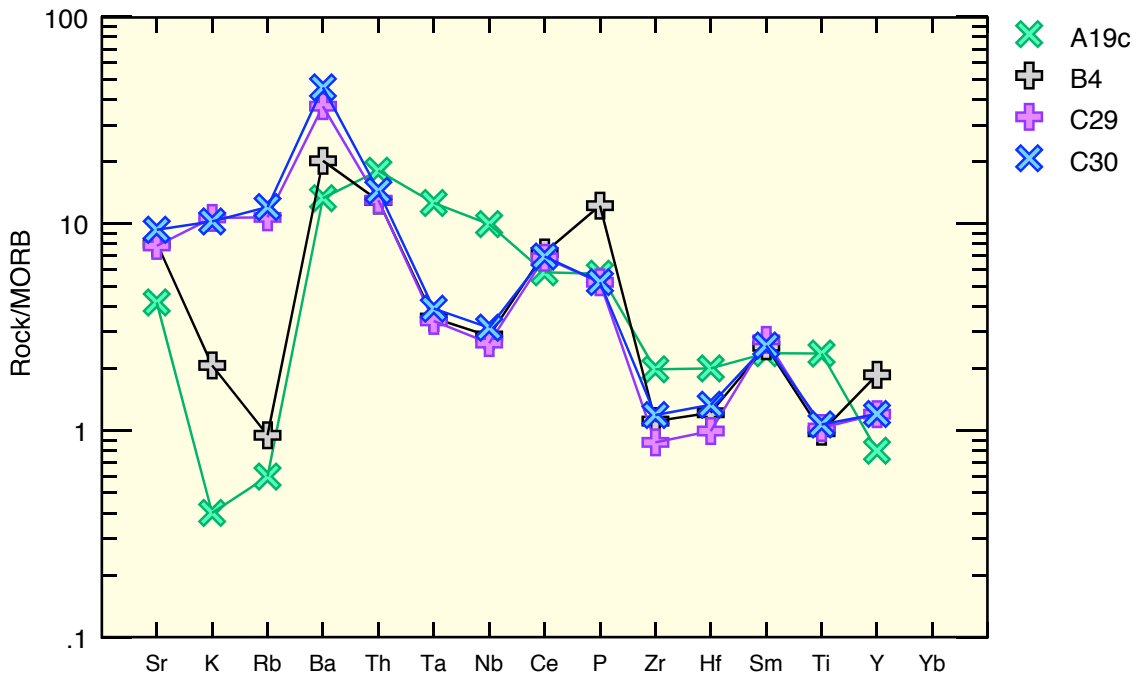


Figure 40: Multi-element diagram normalized to MORB (Pearce, 1982) for samples of basalt bombs.

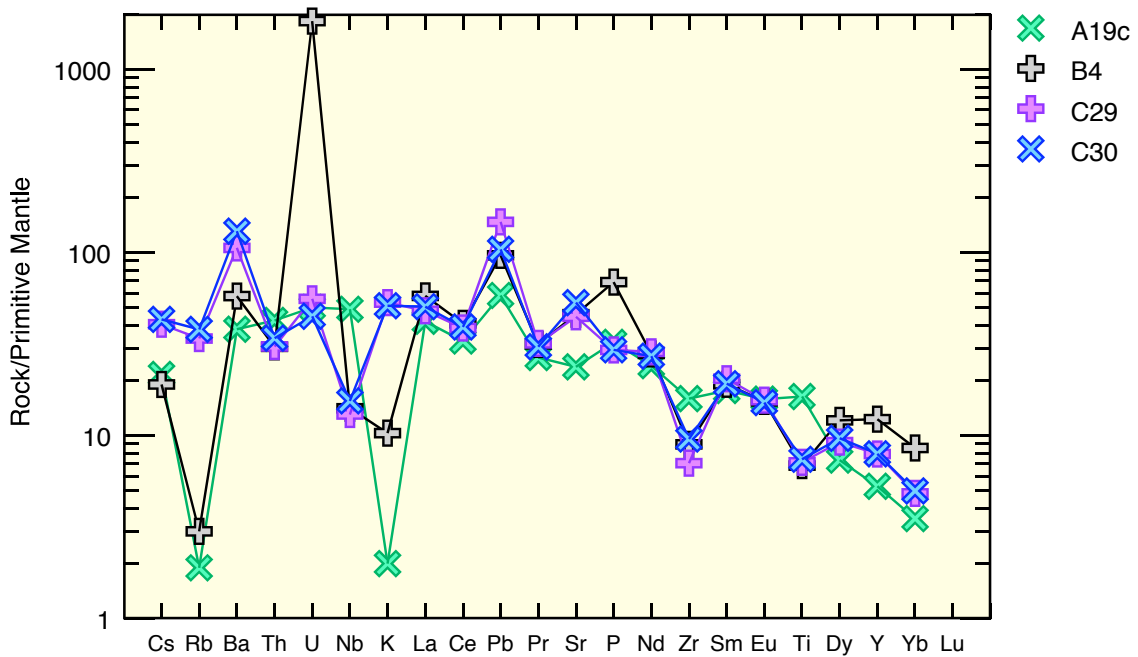


Figure 41: Multi-element diagram normalized to primitive mantle (Sun and McDonough, 1989) for samples of basalt bombs.

Sample B4 shows anomalously low Rb and K concentrations, whereas samples C29 and C30 do not show this feature (Figures 40 and 41). This result directly correlates with the degree of alteration evident in thin section, which clearly resulted in substantial loss of these mobile elements. Sample B4 also has a positive U anomaly that is not shown by the other samples, and this feature is also inferred to be the result of alteration. Use of supposedly immobile trace elements in classifying these rocks leads to ambiguous results, which may be due to alteration. More work is required in order to better understand the magmatic affinities of these rocks.

Sample A19c from Cretaceous pyroclastic deposits on the Pitcock Ranch shows similar LREE enrichment to the Peña Mountain samples; however, it plots separately from those samples in the discrimination diagrams and falls in alkaline or within-plate fields. It also shows a distinctly different pattern on the normalized multi-element diagrams in that it lacks negative Nb and Ta anomalies, which is typical of alkaline basalts (Wilson, 1989). This was not an expected result because the samples share a similar tectonic setting, age, and style of volcanism. Sample A19c has a similar degree of alteration to the Peña Mountain samples, and reasons for the differences in geochemistry between the samples are unclear. More geochemical data are needed from both areas to resolve this problem.

Geochronology

The three basalt bombs collected for geochemistry from Peña Mountain were also subjected to U–Pb zircon SHRIMP-RG isotopic studies. Data are shown in Table 3 on page 70.

Sample B4. Fourteen spot analyses were made on zircon grains from this sample and are plotted on U–Pb concordia diagrams in Figures 42 and 43. Concordant or nearly concordant analyses yielded ages as old as ~1400 Ma, indicating most of the grains are xenocrysts. As shown in a Tera-Wasserburg concordia diagram (Figure 43; Tera and Wasserburg, 1972), the two youngest concordant analyses have overlapping error ellipses and yield a weighted mean age of 77.9 ± 1.4 Ma.

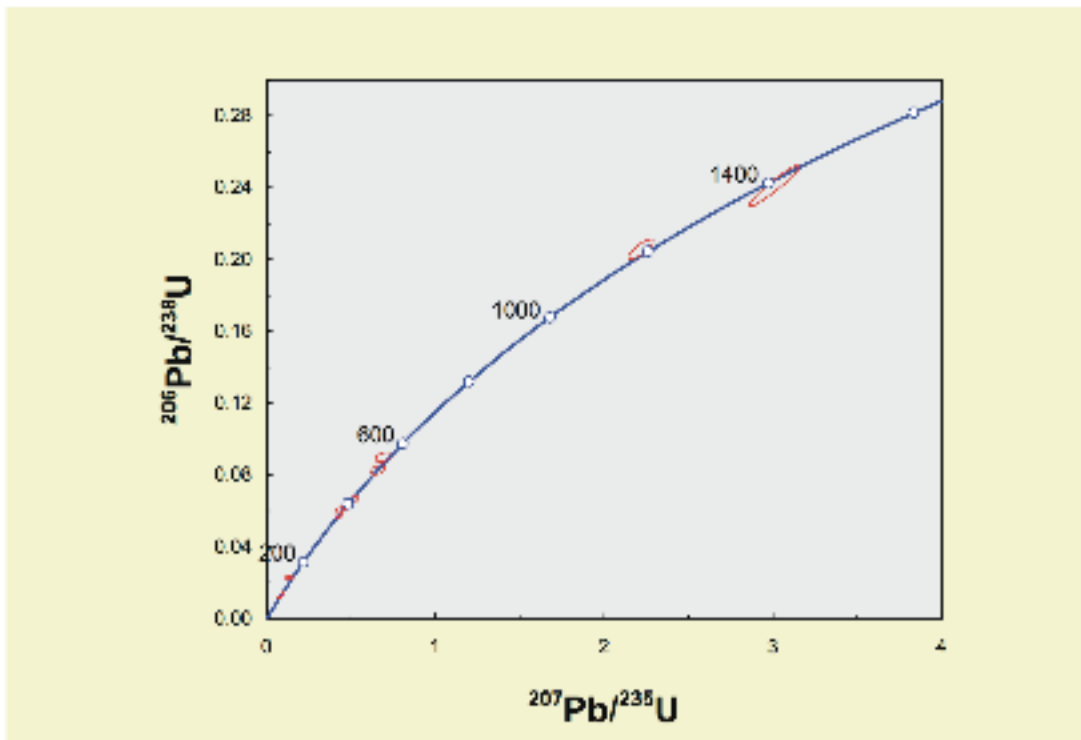


Figure 42: Concordia diagram for Sample B4. Analyses of individual spots on zircon grains are depicted as 2σ error ellipses.

Sample C29. Twelve spot analyses were made on zircon grains from this sample, and results are shown in Figures 44 and 45. As in the previous sample, the majority of the spot analyses yielded a range of ages back into the Proterozoic, which indicates many of these zircon grains are xenocrysts. The youngest analysis is concordant (Figure 45) and gives an

age of 77 ± 2 Ma, which is within error of the weighted mean of the two youngest concordant analyses from sample B4.

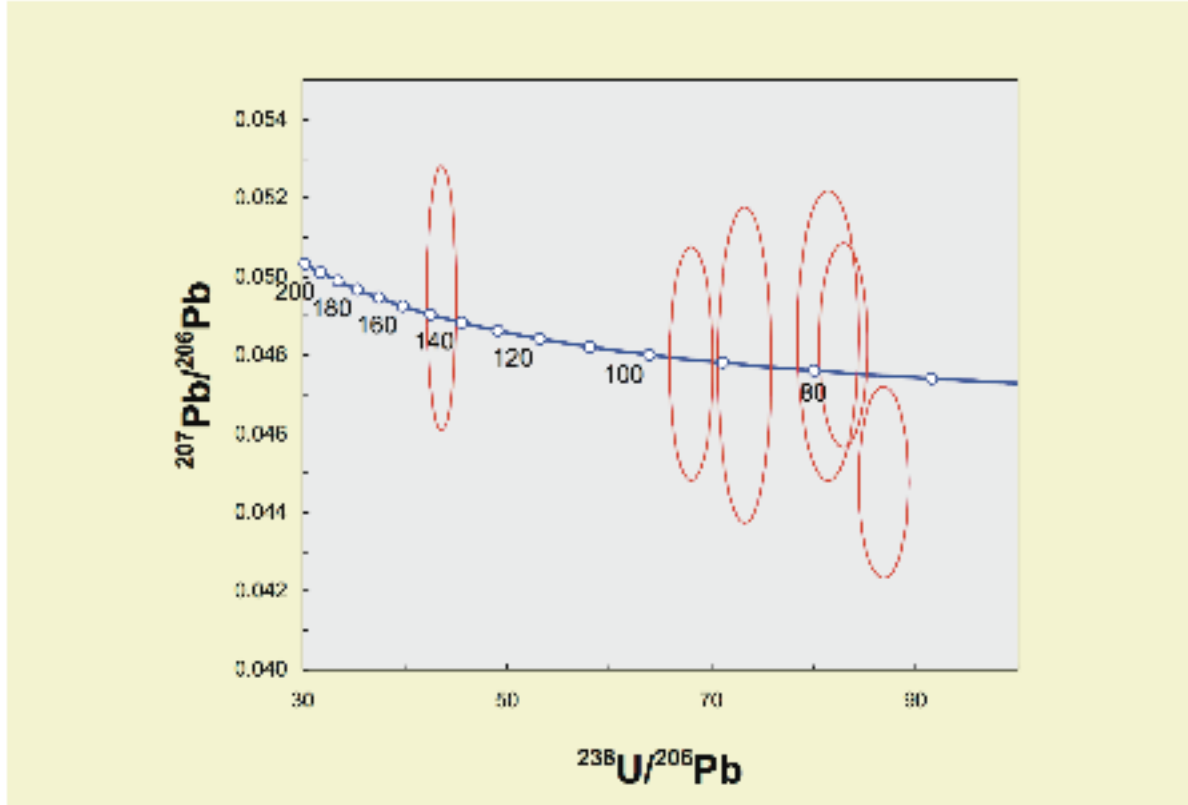


Figure 43: Tera-Wasserburg concordia diagram for analyses yielding younger ages for Sample B4. Analyses of individual spots on zircon grains are depicted as 2σ error ellipses.

Sample C30. Fifteen spot analyses were made on zircon grains from this sample, and results are shown in Figures 46 and 47. Again, many of the grains are clearly xenocrysts, as indicated by ages which range back to > 1000 Ma. The four youngest concordant analyses have overlapping error ellipses (Figure 47). The weighted mean age of these four analyses is 76.1 ± 2.1 Ma. An older population of concordant, overlapping analyses yields a weighted mean age of 96.7 ± 2.1 Ma.

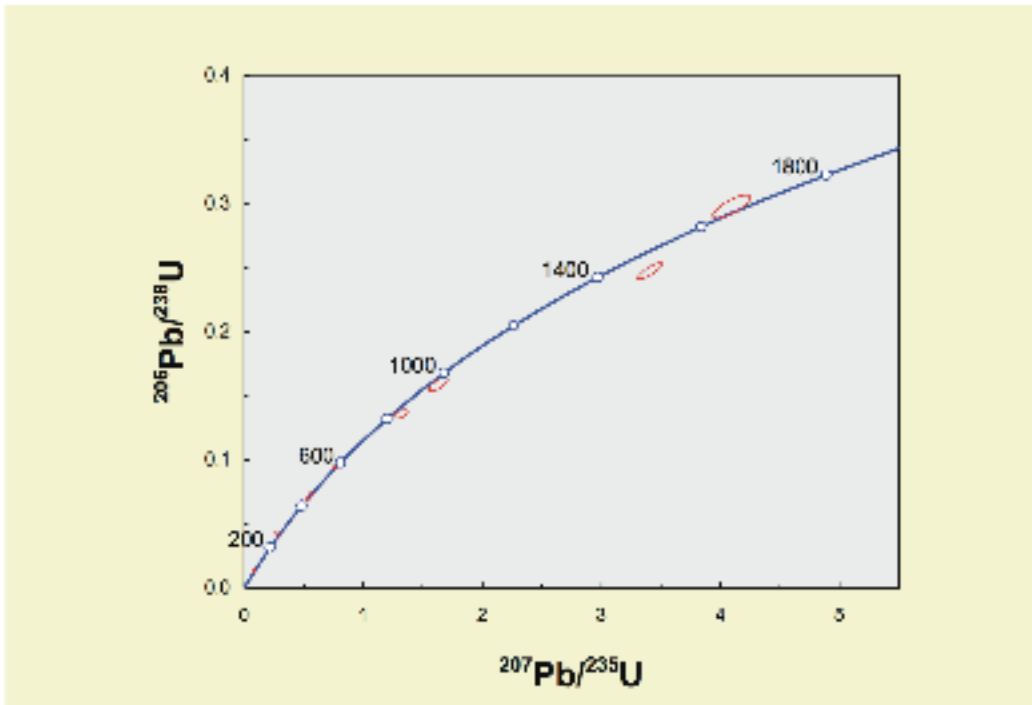


Figure 44: Concordia diagram for Sample C29. Analyses of individual spots on zircon grains are depicted as 2σ error ellipses.

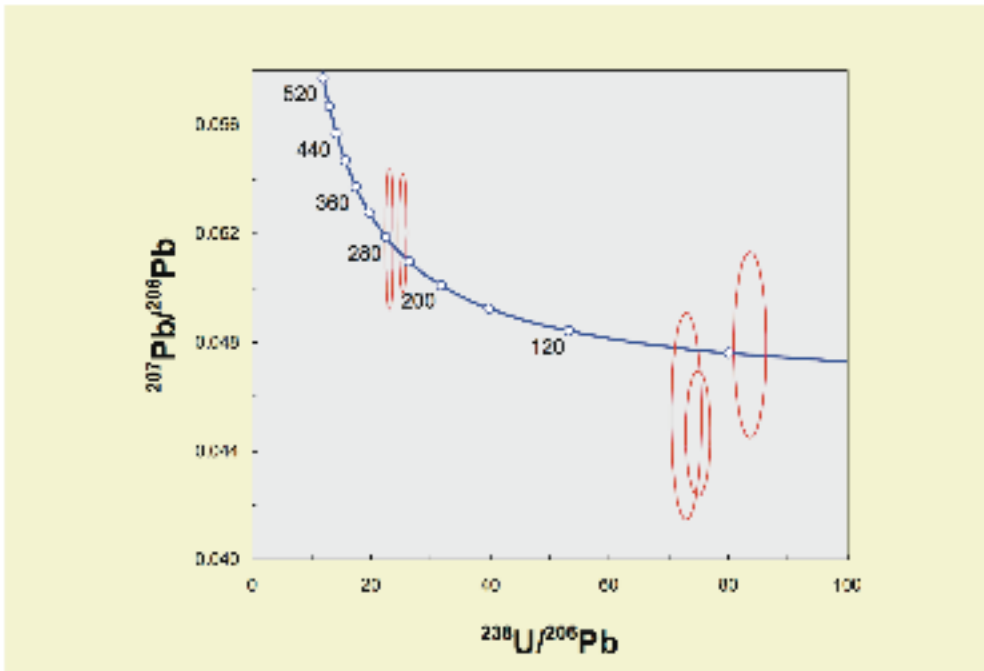


Figure 45: Tera-Wasserburg concordia diagram for analyses yielding younger ages for Sample 29. Analyses of individual spots on zircon grains are depicted as 2σ error ellipses.

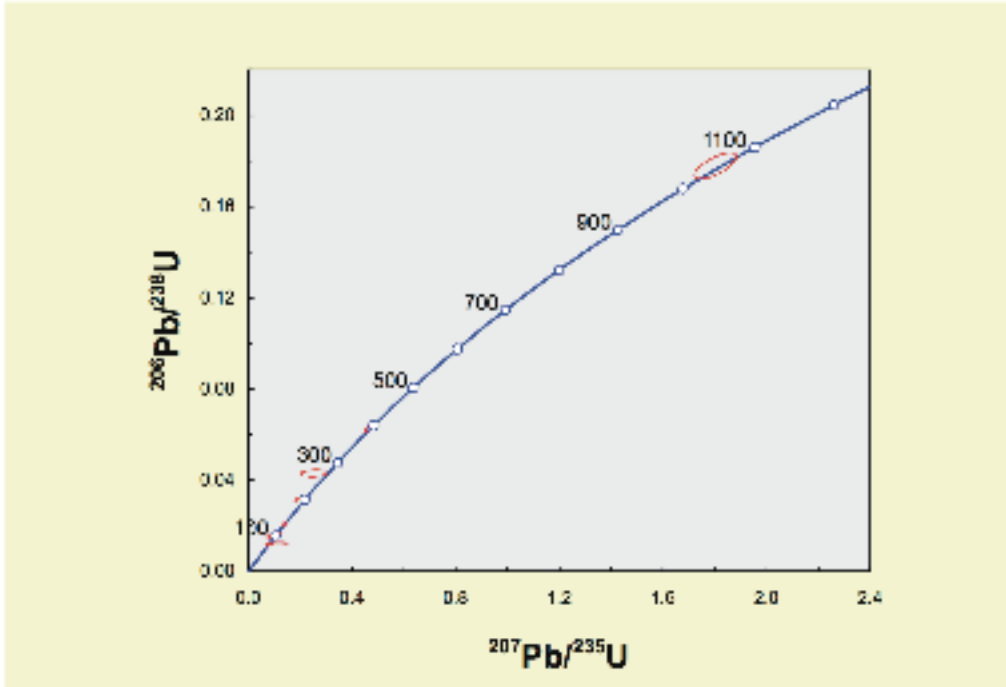


Figure 46: Concordia diagram for Sample C30. Analyses of individual spots on zircon grains are depicted as 2σ error ellipses.

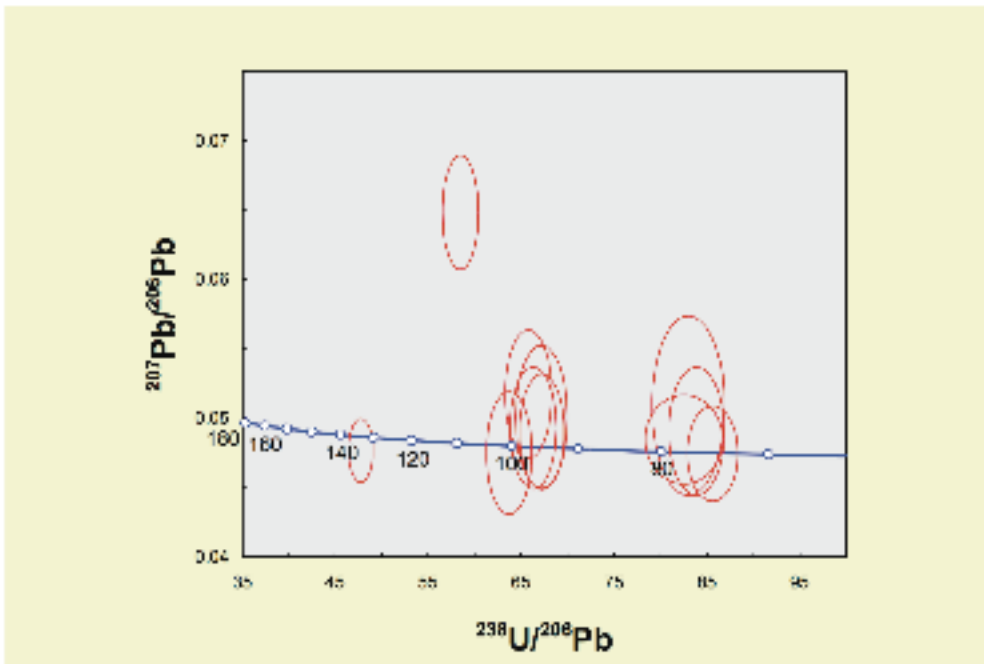


Figure 47: Tera-Wasserburg concordia diagram for analyses yielding younger ages for sample C30. Analyses of individual spots on zircon grains are depicted as 2σ error ellipses.

Table 3: Analytical and calculated data from SHRIMP-RG analyses of zircon grains extracted from basaltic bombs in pyroclastic deposits at Peña Mountain, Big Bend National Park.

Grain No.	Comm. ²⁰⁶ Pb (%)	U (ppm)	Th (ppm)	²³² Th/ ²³⁸ U	²⁰⁷ Pb-corrected		²⁰⁴ Pb-corrected		Total		Total		²⁰⁴ Pb-corrected		²⁰⁷ Pb/ ²³⁵ U		Error corr. coeff.*		
					²³⁸ U/ ²⁰⁶ Pb	1σ error (Ma)	²⁰⁷ Pb/ ²⁰⁶ Pb	1σ error (Ma)	²³⁸ U/ ²⁰⁶ Pb	% error	²⁰⁷ Pb/ ²⁰⁶ Pb	% error	²³⁸ U/ ²⁰⁶ Pb	% error	²⁰⁷ Pb/ ²⁰⁶ Pb	% error		²⁰⁷ Pb/ ²³⁵ U	% error
B4-5	0.05	299	62	0.21	1209.7	12.8	1147	16	4.86	1.1	.0784	0.7	4.86	1.1	.0780	0.8	2.21	1.3	.812
B4-6	0.16	247	135	0.56	412.2	4.9	444	63	15.10	1.2	.0572	1.7	15.13	1.2	.0558	2.8	0.51	3.1	.396
B4-7	0.00	423	224	0.55	358.6	4.1	377	32	17.47	1.2	.0541	1.4	17.47	1.2	.0541	1.4	0.43	1.8	.641
B4-8	0.30	262	201	0.79	378.7	4.5	280	67	16.52	1.2	.0545	1.7	16.57	1.2	.0519	2.9	0.43	3.2	.383
B4-9	0.00	621	105	0.18	94.1	1.2	89	60	68.01	1.3	.0478	2.5	68.01	1.3	.0478	2.5	0.10	2.8	.446
B4-10	0.36	253	134	0.55	557.9	6.3	433	58	11.06	1.2	.0586	1.4	11.10	1.2	.0555	2.6	0.69	2.9	.408
B4-11	0.01	327	19	0.06	1389.9	26.0	1433	12	4.15	1.9	.0905	0.6	4.15	1.9	.0904	0.6	3.01	2.0	.954
B4-12	0.18	152	65	0.44	513.3	6.6	491	52	12.05	1.3	.0586	1.9	12.07	1.3	.0570	2.4	0.65	2.7	.486
B4-13	0.00	330	191	0.60	87.4	1.3	87	82	73.24	1.5	.0478	3.4	73.24	1.5	.0478	3.4	0.09	3.7	.389
B4-14	1.01	313	68	0.23	146.3	2.0	-317	249	43.55	1.4	.0495	2.8	43.99	1.4	.0405	9.7	0.13	9.8	.144
C29-1	0.04	811	79	0.10	816.1	8.2	931	31	7.37	1.0	.0705	1.5	7.38	1.0	.0701	1.5	1.31	1.8	.559
C29-2	0.13	325	166	0.53	1408.6	14.5	1621	12	4.04	1.1	.1009	0.6	4.04	1.1	.0998	0.7	3.40	1.2	.852
C29-3	0.16	121	58	0.50	1685.4	20.5	1616	19	3.36	1.2	.1009	0.9	3.36	1.2	.0996	1.0	4.08	1.6	.771
C29-4	0.03	369	156	0.44	587.9	6.2	564	25	10.48	1.1	.0592	1.1	10.48	1.1	.0589	1.1	0.77	1.6	.687
C29-5	0.00	355	176	0.51	88.1	1.3	-40	83	72.89	1.4	.0453	3.4	72.89	1.4	.0453	3.4	0.09	3.7	.384
C29-6	0.00	517	244	0.49	76.6	1.0	95	69	83.60	1.3	.0479	2.9	83.60	1.3	.0479	2.9	0.08	3.2	.412
C29-7	0.00	116	39	0.35	947.2	12.3	1042	28	6.29	1.3	.0740	1.4	6.29	1.3	.0740	1.4	1.62	1.9	.695
C29-8	0.00	336	834	2.56	457.5	5.0	421	30	13.61	1.1	.0552	1.3	13.61	1.1	.0552	1.3	0.56	1.7	.640
C29-9	0.07	418	223	0.55	249.9	2.8	260	44	25.28	1.1	.0520	1.7	25.29	1.1	.0514	1.9	0.28	2.2	.513
C29-10	0.49	294	128	0.45	273.9	3.3	76	112	23.03	1.2	.0518	2.1	23.15	1.2	.0475	4.7	0.28	4.9	.256
C29-11	-0.06	1017	462	0.47	85.8	1.0	-46	52	74.89	1.1	.0447	2.1	74.84	1.1	.0452	2.2	0.08	2.4	.464
C29-12	0.05	361	127	0.36	437.3	4.8	438	33	14.24	1.1	.0560	1.4	14.25	1.1	.0556	1.5	0.54	1.8	.606
C30-1	0.03	1024	544	0.55	392.3	3.8	342	20	15.95	1.0	.0536	0.8	15.96	1.0	.0533	0.9	0.46	1.3	.743
C30-2	0.48	517	167	0.33	74.9	1.0	-151	135	85.58	1.3	.0475	2.9	85.99	1.3	.0433	5.4	0.07	5.6	.236
C30-3	0.00	116	59	0.53	1056.9	13.3	1020	26	5.62	1.3	.0732	1.3	5.62	1.3	.0732	1.3	1.80	1.8	.709
C30-4	0.32	237	187	0.82	96.9	1.5	147	127	65.77	1.6	.0518	3.7	65.98	1.6	.0490	5.4	0.10	5.6	.279
C30-5	0.18	561	363	0.67	77.6	1.6	45	85	82.51	2.1	.0485	2.7	82.66	2.1	.0469	3.6	0.08	4.1	.502
C30-6	0.00	311	119	0.39	95.1	1.4	150	81	67.22	1.5	.0490	3.5	67.22	1.5	.0490	3.5	0.10	3.8	.387
C30-7	0.62	231	88	0.39	100.5	1.6	-227	199	63.69	1.6	.0475	3.8	64.09	1.6	.0420	7.9	0.09	8.1	.197
C30-8	0.45	165	92	0.58	199.9	3.0	-5	161	31.77	1.5	.0499	3.2	31.91	1.5	.0460	6.7	0.20	6.8	.223
C30-9	0.79	196	106	0.56	95.0	1.6	-159	291	67.17	1.7	.0501	4.2	67.70	1.8	.0431	11.7	0.09	11.9	.149
C30-10	0.00	359	165	0.47	76.3	1.1	152	90	83.84	1.5	.0491	3.8	83.84	1.5	.0491	3.8	0.08	4.1	.355
C30-11	0.00	251	148	0.61	96.4	1.5	163	85	66.29	1.5	.0493	3.6	66.29	1.5	.0493	3.6	0.10	3.9	.388
C30-12	1.07	218	166	0.79	274.8	3.6	-226	228	22.97	1.3	.0514	2.3	23.22	1.4	.0420	9.0	0.25	1.4	.150
C30-13	0.00	671	266	0.41	133.9	1.5	84	46	47.71	1.1	.0477	1.9	47.71	1.1	.0477	1.9	0.14	1.1	.504
C30-14	-1.28	163	79	0.50	76.9	1.5	673	259	82.98	1.9	.0509	5.2	81.93	2.1	.0620	12.1	0.10	2.1	.170
C30-15	3.11	343	97	0.29	107.3	1.5	-540	546	58.45	1.3	.0648	2.6	60.32	1.6	.0372	20.3	0.09	1.6	.078

* Error correlation coefficient between ²⁰⁷Pb/²³⁵U and ²⁰⁶Pb/²³⁸U.

Interpretation of pyroclastic deposits at Peña Mountain

The Upper Cretaceous pyroclastic deposits at Peña Mountain are inferred to be the erosional remnants of at least two maar volcanoes. Both on the northern and southern sides of the mountain, the deposits are interpreted to be composed primarily of base-surge and air-fall deposits formed from pulsatory phreatomagmatic eruptions. Individual beds of lapilli tuff and lapillistone either formed by pyroclastic fall or relatively high-energy base surges, whereas thin tuff interbeds are air-fall deposits or formed from low-energy, dilute portions of base surges. Armored lapilli and impact sags indicate the deposits were wet and cohesive. In some deposits, blocks and bombs show no impact sags, which suggests they were transported laterally by base surges. Base-surge deposits, in some cases, show erosional scour along their base. Sparse bed forms indicate that tractional transport occasionally became an important process in near-vent base surges. Non-carbonized, petrified wood in the deposits indicates some surges were emplaced at relatively low temperature.

The lapilli tuff present at the base of the less disturbed part of the succession on the southern side of Peña Mountain contains angular mudstone clasts, and represents the depositional boundary zone of an erosive base surge. The base surge ripped up and incorporated mudstone clasts as it traveled over the partially consolidated Aguja mudstone. Thick, massive, block-and-bomb-rich intervals may represent a combination of deposition from high-particle-concentration base surges and rapid accumulation of unsorted ballistic pyroclasts in a near-vent setting.

Angular pyroclast shards represent pieces of quenched and shattered magma, whereas fluidal clasts were erupted as fluid droplets of magma. Flattened mudstone blocks in the pyroclastic strata were erupted as semi-consolidated masses of mudstone from underlying

Aguja strata. Intimate magma-sediment interaction is indicated by the tabular mass of mudstone that contains fluidal basalt clasts and occurs within one of the bomb-and-block-rich intervals. This mass may represent an erupted sample of some of the phreatomagmatic slurry which formed in the vent (cf., White, 1991), or may represent peperite formed in the diatreme root zone. Ubiquitous quartz xenocrysts within basaltic lapilli also imply intimate magma-sediment interaction within the vent or the diatreme root zone. Lorenz et al. (2002) described lapilli containing quartz xenocrysts, which were incorporated from unconsolidated sediment during magma-sediment interaction within the diatreme root zones of maars in West Eifel, Germany. Those authors concluded that this type of magma-sediment interaction could not be termed peperite because unfragmented magma encloses clastic material. Such features do, however, record intimate magma-sediment interaction, indicating the formation of peperite within the root zone. This process is clearly important in the formation of phreatomagmatic volcanoes (cf., Hanson and Elliot, 1996; Lorenz et al., 2002).

Highly variable bedding attitudes in the lower sequence on the northern side of Peña Mountain are not attributable to Laramide folding because neither the upper pyroclastic sequence nor laterally equivalent parts of the Aguja Formation show similar variations. Deformation during the emplacement of the syenodiorite intrusion seems unlikely, because strata in the upper sequence near the intrusive contact show no deformation. It is also unlikely that the variable bedding attitudes in the lower sequence are controlled by pre-existing topography because the upper portions of the upper shale member represent inland floodplain deposits (Lehman, 1985), which likely had low relief. The variable bedding attitudes are inferred to represent different degrees of disturbance during slumping. Soft-

sediment injections along normal faults in the lower pyroclastic sequence are consistent with syneruptive slumping of the strata.

The truncation surface between the two pyroclastic sequences on the northern side of Peña Mountain is overlain by a thinly bedded lacustrine unit, which indicates a period of eruptive quiescence that may have lasted for a significant length of time. Individual laminae within the lacustrine unit may in part represent varve-like layers that record yearly deposition. The upper pyroclastic sequence rests unconformably upon the lower pyroclastic sequence or the intervening lacustrine unit. Changes in bedding attitude across the truncation surface indicate the upper and lower pyroclastic sequences were generated from different but adjacent vents.

The presence of the araucarioid conifer just above the contact between pyroclastic strata and Aguja mudstone suggests the conifer may have grown from the mudstone and was killed by base surges generated from eruptions during deposition of the first pyroclastic sequence. In addition, the fragment of wood derived from the trunk indicates a southwesterly flow direction for at least some of the base surges during accumulation of the lower sequence. The occurrence of this trunk is interesting because araucarioid conifers are rare in the Aguja Formation, and current araucariacean species are known to favor volcanic soils (Wheeler and Lehman, 2005).

The lower portion of the pyroclastic succession on the southern side of Peña Mountain preserves a crater margin developed in the Aguja Formation, as indicated by detailed field relations in that area. A strongly disturbed zone of nonvolcanic Aguja strata and overlying tephra showing discontinuous bedding that locally dips steeply into the crater

defines the crater margin. This zone is inferred to have formed by slumping into the crater during and after an initial episode of explosive volcanism.

In places the crater margin is highly irregular (Figure 26), suggesting piecemeal collapse of parts of the rim. Bedding attitudes in the less disturbed pyroclastic strata on the southern side of Peña Mountain are too variable and too steep to be controlled solely by constructional volcanic topography. In places, the less disturbed strata strike into the irregular edge of the crater (Figures 25 and 26). Therefore, the less disturbed pyroclastic strata are interpreted to have been deposited after significant subsidence and slumping had occurred, but were then affected by a subsequent episode of subsidence. Outward expansion of crater margins and extensive slumping have been documented from other phreatomagmatic volcanoes (White and McClintock, 2001). Lateral vent migration, controlled by collapse of unstable country rock and structure within the country rock, is also a common feature of such volcanoes (Sohn and Park, 2005).

The lower pyroclastic sequence on the northern side of Peña Mountain is inferred to correlate with the entire pyroclastic succession to the south. The distance between the inferred crater on the southern side of the mountain and the lower pyroclastic sequence to the north is consistent with lateral facies relationships compiled by Chough and Sohn (1990), and with typical dimensions of maar craters and associated tuff rings (Wohletz and Sheridan, 1983). The work of Chough and Sohn (1990) provides a framework for understanding the origin and distance from source of the pyroclastic deposits at Peña Mountain, which are predominantly composed of massive to stratified strata that contain few tractional bed forms. These deposits represent proximal, near-vent facies according to the lateral facies model

shown in Figure 2. In addition, numerous basalt bombs and lithic blocks indicate emplacement in a relatively near-vent setting.

The upper pyroclastic sequence on the northern side of Peña Mountain is inferred to record construction of a new vent after a period of quiescence and lacustrine sedimentation. Lateral facies relationships and impact sags indicate this second vent was nearby the first one and was within one kilometer of it.

Examination of the facies described in the detailed measured section (Figure 18) provides additional information about the nature of the pyroclastic deposits at Peña Mountain. Reversely graded, clast-supported lapilli tuff in Package 1 either results from rapid deposition from a high-particle-concentration base surge or from pyroclastic fall processes. Impact sags indicate ballistic emplacement of at least some lapilli. The thin tuff that drapes the lapilli tuff is interpreted to have been deposited from the low-particle-concentration tail of the surge or from fallout of ash from the eruption column. Open-framework, poorly to well-sorted lapillistone beds in Packages 2, 3, and 7 may represent air-fall deposits. The lapillistone beds in packages 3 and 7 grade into overlying tuff or lapilli-tuff beds. Open-framework, well-sorted lapillistone beds in packages 5 and 9 resemble air-fall deposits; however, these packages are marked by basal scour. They are inferred to have formed from erosive base surges that scoured into underlying beds. Package 5 is overlain by planar laminated tuff in Package 6, which may record deposition from low-energy base surges or portions of base surges (White, 1991), or may have formed by air-fall processes. Packages 4 and 8 contain undulatory beds of lapilli and ash, which are inferred to have formed as the result of upper flow-regime tractional processes in base surges.

In general, thinly stratified beds at Peña Mountain with undulatory bed forms are inferred to represent dilute, low-particle-concentration base surges. According to the lateral facies model of Chough and Sohn (1990), fine-grained lapilli tuffs with tractional, upper flow-regime bed forms occur in distal surges due to down-current surge transformations. However, at Peña Mountain, undulatory bed forms occur in a near-vent environment. The vertical facies relationship model by Chough and Sohn (1990) explains this discrepancy. Distinct separation of coarse and fine beds in some surge deposits is interpreted to represent particle segregation in the base surges. The base surges were composed of a particle-rich basal portion overridden by a turbulent, low-particle-concentration ash cloud. The lack of separation in some massive surge deposits shown in the detailed measured section (e.g., packages 5 and 9) indicates significant grain-size segregation only occurred in some base surges. Since base surges form by column collapse, the nature of the base surge is ultimately controlled by the nature of the eruption column and degree of collapse. In the deposits at Peña Mountain, varying properties of the eruption column and the manner of collapse formed surges of different velocity and carrying capacity in a near-vent setting, leading to the formation of tractional bed forms in some relatively dilute proximal surges.

The high number of lithic blocks that occur in the pyroclastic deposits indicates downward quarrying by the eruption into underlying Aguja strata. Based on descriptions of members in the Aguja Formation by Lehman (1985), sandstone blocks with abundant oyster shells are clearly derived from the Rattlesnake Mountain Sandstone Member, which is located ~150 m below the upper shale member in the Peña Mountain area. The lack of limestone blocks in the pyroclastic deposits indicates that the eruptions did not excavate into the underlying Pen Formation, which contains abundant limestone and is estimated to be >

300 m stratigraphically beneath the pyroclastic deposits, based on stratigraphic sections shown in Lehman (1985). Thus, the eruptions excavated down at least 150 m into surrounding country rock but did not reach depths of ~300 m. A high percentage of the pyroclastic strata are composed of accidental lithic clasts and sand-sized detritus, which also suggests downward excavation occurred during formation of the maars.

Figure 48 illustrates the inferred eruptive processes at Peña Mountain, which are similar to the processes described by White (1991) at Teshim Maar in the Hopi Buttes field. The upper shale member would likely have been a poor contributor of free water needed to drive phreatomagmatic eruptions because the unit is dominantly composed of impermeable mudstone. Channel sandstones would have made good aquifers; however, the scarcity of these units in the upper shale member makes it unlikely that they contributed significant amounts of water to eruptions. Following White (1991, 1996), I infer that a mud-water slurry acted as the coolant in phreatomagmatic explosions driven by fuel-coolant interactions in this part of the stratigraphic sequence. The Rattlesnake Mountain Sandstone Member may have been a significant source of free water once downward excavations by the eruptions quarried to that depth.

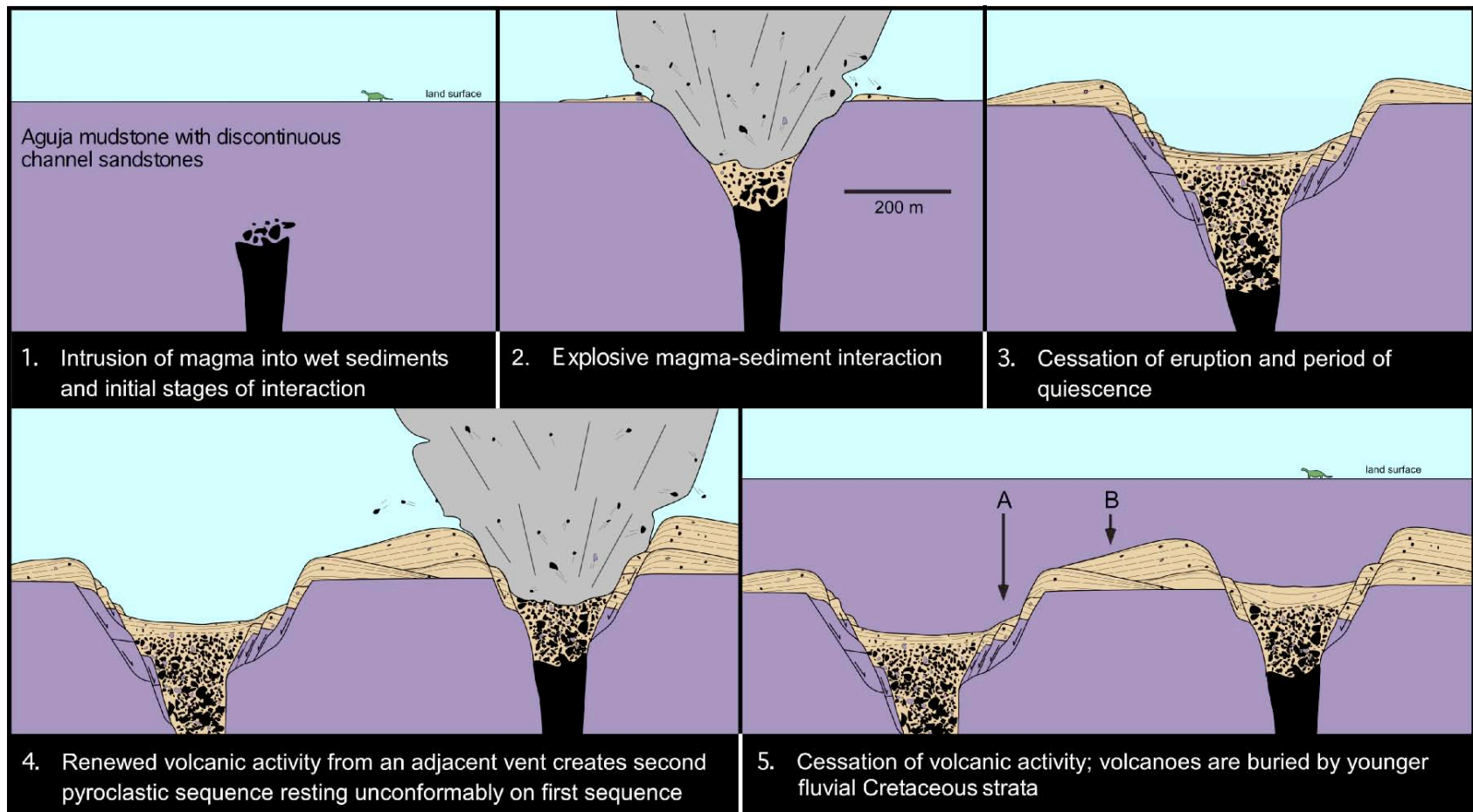


Figure 48: Model of two overlapping maar volcanoes at Peña Mountain. A = approximate location of exposures on the southern side of Peña Mountain. B = approximate location of exposures on the northern side of Peña Mountain.

Interpretation of geochronology

U–Pb zircon SHRIMP-RG analyses from pyroclastic deposits at Peña Mountain yield a range of ages from Proterozoic to Late Cretaceous. Most of the ages clearly come from xenocrysts. The source of the xenocrysts remains enigmatic. Lenticular sandstones in the upper shale member of the Aguja Formation contain detritus derived from Cretaceous arc terranes further west (Lehman, 1991), and therefore it is possible that some zircons are detrital grains incorporated into the basalt when the magma intruded into Aguja strata. Air-fall tuffs within lower parts of the Aguja generated by continental arc magmatism far to the west might be another possible source, but the absence of documented tuffs in lower levels of the Aguja Formation is a problem with this interpretation.

If the youngest concordant analyses in all of the samples are considered together, they yield a weighted mean age of 76.6 ± 1.3 Ma (Figure 49). A reasonable interpretation of the data is that these concordant analyses represent the igneous age of the basalt, which would provide an absolute age for the upper shale member of the Aguja Formation at Peña Mountain. However, the youngest zircon grains look similar to the other grains under cathodoluminescence and could conceivably be xenocrysts derived in a similar fashion to those discussed above. It is therefore necessary to see if a crystallization age of 76.6 ± 1.3 Ma for the basalt is consistent with available stratigraphic evidence.

The upper shale member at Peña Mountain is Upper Campanian to possibly Lower Maastrichtian (Lehman, 1985; Schiebout et al., 1987). Other age constraints on the upper shale member are based on the following lines of evidence (paraphrased from a written communication from Dr. Thomas Lehman, 2006):

- The lower age limit of the upper shale member is constrained to be ~80 Ma by the youngest ammonite zone, *Baculites maclearni*, present in the lower, marine portion of the Aguja Formation.
- Fossil vertebrates in the upper shale member have similarities to Judithian (~79–73 Ma) vertebrate fauna in the Judith River Group in Montana and Alberta, as well as to dinosaur fossils in the later part of the Judithian (~76–73 Ma) Kirtland Formation in New Mexico and Dinosaur Park Formation in Alberta, suggesting the upper shale member is equivalent in age to these units.
- A fossil mammal, *Paleomolops langstoni*, found in the Aguja Formation is closely related to species found elsewhere solely in Aquilan vertebrate faunas (pre-Judithian, ~84–79 Ma), consistent with an earliest Judithian age for the upper shale member.
- The upper age limit of the upper shale member is constrained by a tuff bed within the conformably overlying Javelina Formation, which yielded a U–Pb monazite age of 69 ± 1 Ma (McDowell et al., 2004).

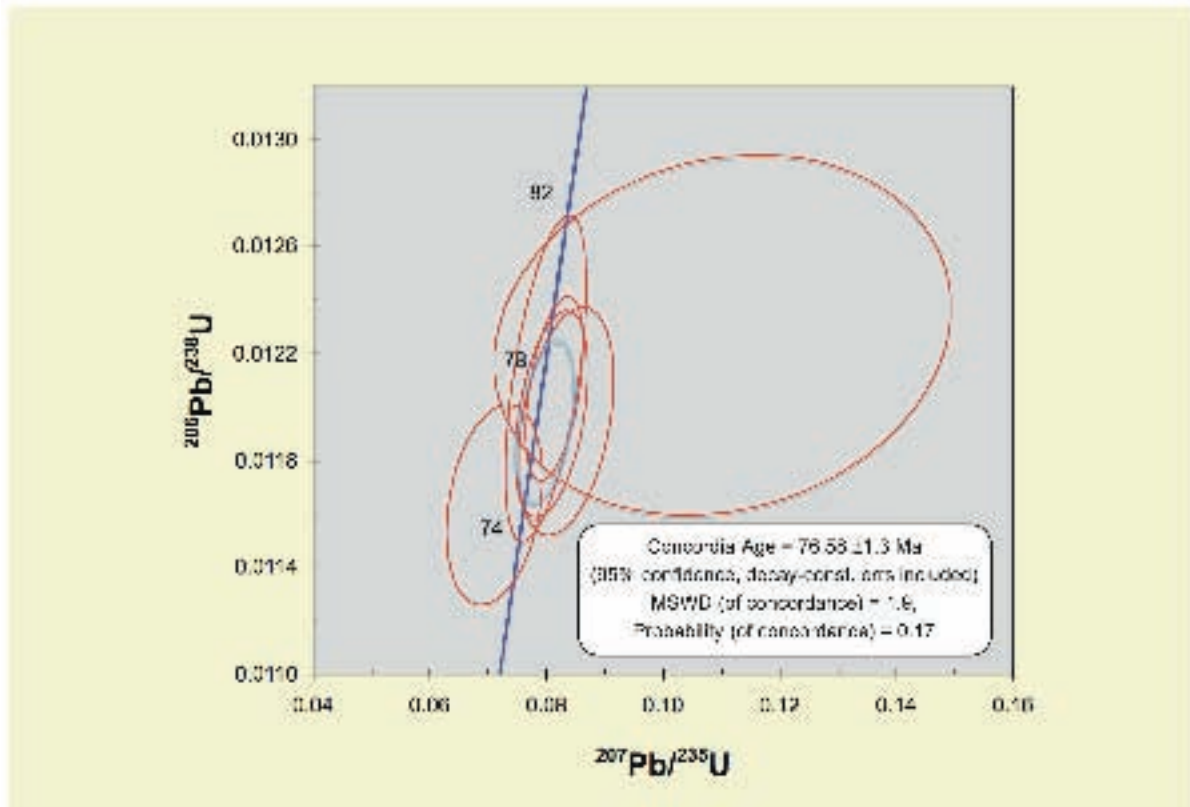


Figure 49: Concordia diagram for the youngest concordant analyses for all three samples from Peña Mountain. Analyses of individual spots on zircon grains are depicted as 2σ error ellipses. The blue error ellipse indicates weighted mean age for all analyses.

These lines of evidence are consistent with the U–Pb isotopic age of 76.6 ± 1.3 Ma for the pyroclastic deposits in the upper shale member of the Aguja Formation. This age is also consistent with the time scale of Ogg et al. (2004), who place the upper boundary of the Campanian at 70.6 ± 0.6 Ma. However, a magnetic polarity sequence from the upper shale member near Talley Mountain has been correlated with polarity chron C32, which has an age range of ~ 73 – 70 Ma. This correlation may conflict with an age of 76.6 ± 1.3 Ma for the pyroclastic deposits at Peña Mountain. However, it is possible that the paleomagnetic correlation is inaccurate, because emplacement of nearby Tertiary intrusions may have overprinted the original Late Cretaceous detrital magnetism in the section (Thomas Lehman, written communication, 2006).

The age of 76.6 ± 1.3 Ma for the pyroclastic deposits at Peña Mountain is broadly consistent with a U–Pb SHRIMP-RG age of 72.6 ± 1.5 Ma from zircon extracted from a block of basalt within the Cretaceous pyroclastic sequence at the Pitcock Ranch 43 km to the north (Breyer et al., 2005, and in review). When error bars are taken into account, the ages could be as little as 1.2 Ma apart. These new age data show that the upper shale member may be somewhat time-transgressive across this area of the Tornillo basin.

Chapter 4: Eocene intrusions and magma-sediment interaction

Introduction

Tertiary basaltic to intermediate dikes and other igneous bodies intrude into and interact with strata of the Cretaceous Javelina Formation and Paleogene Black Peaks and Hannold Hill Formations on the Pitcock Ranch and adjacent parts of Big Bend National Park (Figure 50). Most of the dikes described in this study are exposed in a single drainage in the eastern portion of the Pitcock Ranch. Dr. Arthur Busbey initially identified them. Murray (1999) subsequently mapped two of the dikes and noted the presence of intrusive pillows along the dike margins. Other dikes have been identified in the present study (Figure 50). Individual dikes are exposed for up to 250 m along strike in the drainage. A single east-west-trending dike crops out for several kilometers in the southwestern portions of the Pitcock Ranch and adjacent areas and has been mapped by previous authors (Maxwell et al., 1967; Henry et al., 1989; Murray, 1999). The present study provides geochemical data and field descriptions of the long east-west-trending dike and other less extensive dikes on the Pitcock Ranch. All of the dikes examined during the course of this study have intrusive contacts marked by billows and/or intrusive pillows. Like the long east-west-trending dike, the less extensive dikes intruded through unconsolidated mudstones and trend east-northeast.

The trend of the dikes is similar to the dominant trend of Tertiary dikes emplaced in the Trans-Pecos region prior to the onset of Basin and Range extension. In particular, the dikes in the study area are inferred to have been emplaced during the formation of the Eocene Christmas Mountains intrusive complex located farther to the west (Figure 51) (Henry et al., 1989). In discussing magma-sediment interaction during emplacement of these intrusions, it

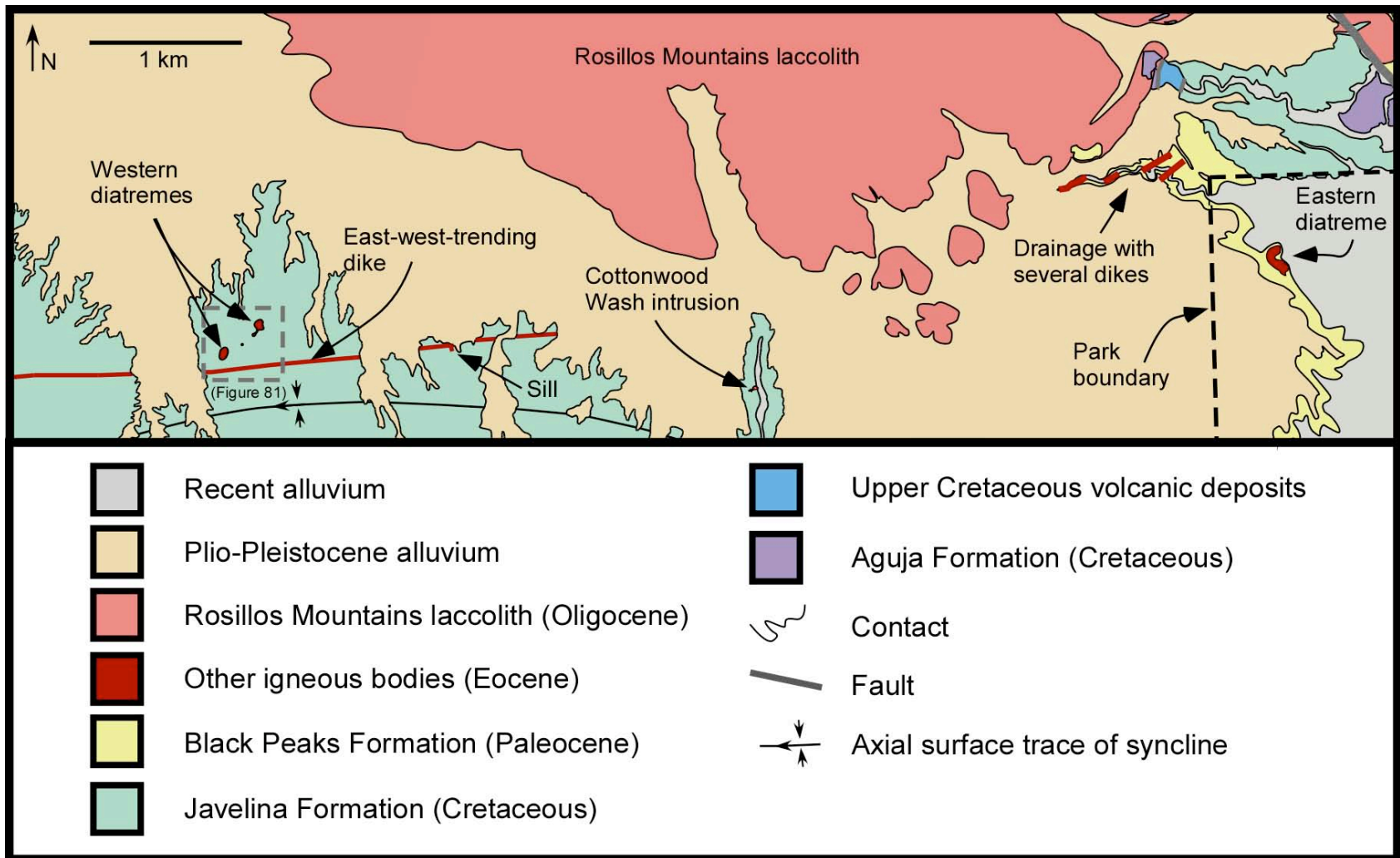


Figure 50: Geologic map of the southern flank of the Rosillos laccolith showing locations of all Tertiary intrusions. General geology after Murray (1999) and Horton (2006). Thickness of dikes not to scale. Location shown in Figure 6. Sill mapped by Murray (1999) and is associated with the east-west-trending dike.

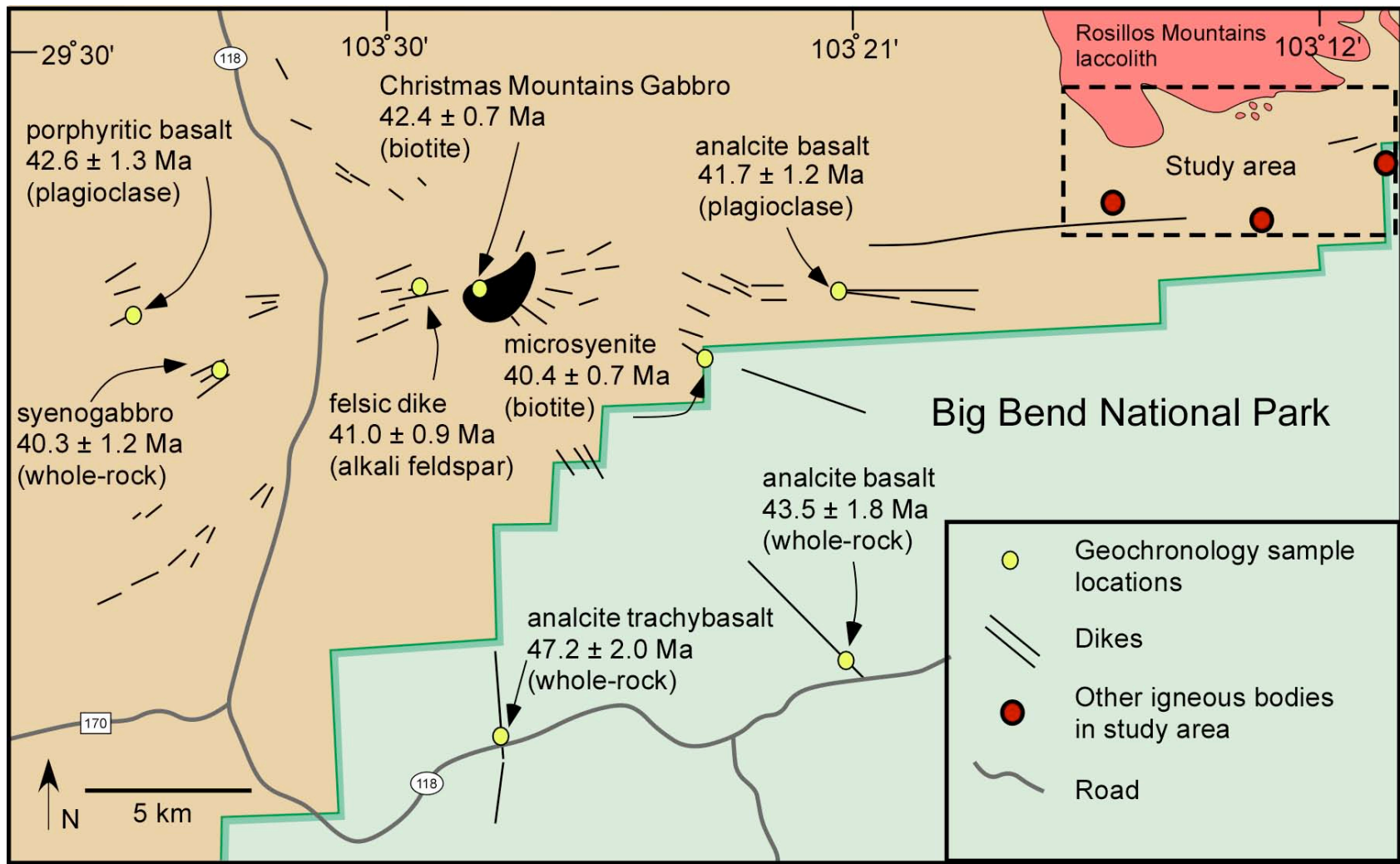


Figure 51: K–Ar ages and trends of dikes associated with the emplacement of the Christmas Mountains intrusive complex (modified from Henry et al., 1989). According to Henry et al. (1989), the trachybasalt dike with an age of 47.2 ± 2.0 Ma may not be related to the Christmas Mountains dike swarm.

is important to note that during the Eocene, Trans-Pecos Texas experienced a wet, subhumid to temperate climate (see Chapter 2), suggesting that strata in the Javelina, Black Peaks, and Hannold Hill Formations likely contained abundant groundwater.

Four other igneous intrusions are described in this chapter. Three of these are interpreted to be hypabyssal intrusions related to diatreme root zones, whereas the other intrusion is a coherent basaltic mass that crops out in Cottonwood Wash on the Pitcock Ranch. The largest intrusion is interpreted as a diatreme root zone and occurs in Big Bend National Park to the southeast of the Pitcock Ranch. It was mapped and described by Maxwell et al. (1967) as two dike-like masses of porphyritic olivine diabase. The other two diatreme root zones occur in the southwestern area of the Pitcock Ranch. Murray (1999) identified one of the diatreme root zones with remote sensing, and briefly described well-developed peperite at this location. The third diatreme root zone has not been previously mapped or described.

Chemical analyses and CIPW norms for each of these intrusions are shown in Table 4 on pages 110 and 111. Most of the intrusions are nepheline-normative, although the values for some of the samples must be treated with caution due to extensive alteration. Mafic intrusions related to the Christmas Mountains intrusive complex are also typically nepheline-normative, as are many other mafic intrusions throughout the region (Henry et al., 1989).

Dikes and Cottonwood Wash intrusion

The dikes and Cottonwood Wash intrusion on the Pitcock Ranch generally contain phenocrysts of resorbed plagioclase up to 0.5 mm long set within a pilotaxitic to intergranular groundmass. Other phenocryst and groundmass minerals have been heavily

altered in most samples. Carbonate occurs in amygdules in many of the samples and partially replaces plagioclase in the more heavily altered rocks. Brown and green phyllosilicate minerals have replaced primary ferromagnesian minerals in heavily altered rocks.

Phenocrystic and groundmass olivine is generally completely replaced by carbonate and secondary oxides but is recognizable by crystal shape. The long east-west-trending dike to the southwest of the other intrusions is less altered and has a lower color index. It is composed of phenocrysts of zoned plagioclase, titanite, and euhedral olivine, with the latter mineral replaced by brown phyllosilicates. The phenocrysts are set within a coarse-grained intergranular groundmass (transitional to barely phaneritic). The presence of titanite suggests alkaline affinities, but nepheline does not appear in the norm (Table 4).

Long east-west-trending dike

A well-exposed dike, much larger than any of the other dikes in the study area, forms a ridge at least 10 km long that is well defined on 1:24,000 topographic maps. It is 5–10 m thick and intrudes the Javelina Formation. Aphanitic margins ≥ 3 cm thick are composed of clear sideromelane glass altered to extremely fine-grained zeolites and contain hyalopilitic plagioclase microlites showing swallowtail forms indicative of rapid aqueous quenching (Bryan, 1972). The amount of microlites in the margins increase inwards, and the chilled margins grade into a barely phaneritic center. In places, secondary gypsum crystals cover the outer surface of the dike. Fine-scale contraction cracks occur along the chilled margin. The baked zone in the host mudstone is ≤ 50 cm thick. In some locations, the typically white to purple mudstone is green in the baked zone, presumably reflecting a reduction of Fe^{3+} to Fe^{2+} .

during baking. The baked zone also shows crude, centimeter-scale columnar jointing developed perpendicular to the dike surface.

The margins of the dike are well exposed in three dimensions. Billows and cusped invaginations on the surface of the dike (Figure 52) are larger than those seen in the other dikes discussed in this study. Billows are on average 1 m across; however, they tend to be elongate parallel to the trend of the dike, with long axes of up to 5 m (Figure 53). Cusped invaginations filled with tendrils of baked mudstone separate billows and penetrate ≤ 50 cm into the dike (Figure 52). Some tendrils contain chilled, angular igneous clasts up to 1 cm across that are intermixed with mudstone, which is a feature indicative of quench fragmentation.

Murray (1999) mapped a sill several meters thick at one locality adjacent to the dike. Field study during the present project indicates that the sill extends directly from the dike and is lithologically identical to it. The sill, however, is much more heavily altered than the dike. Because of the alteration, evidence for interaction with sediment along the margin of the sill is lacking.

Dikes in the drainage on the southeastern portion of Pitcock Ranch

Six dikes intruding the Black Peaks Formation are exposed in the drainage in the southeastern portion of the Pitcock Ranch. All of the dikes show evidence of magma-sediment interaction along their margins. Two well-exposed dikes showing important examples of various features formed by magma-sediment interaction are discussed separately in this section.

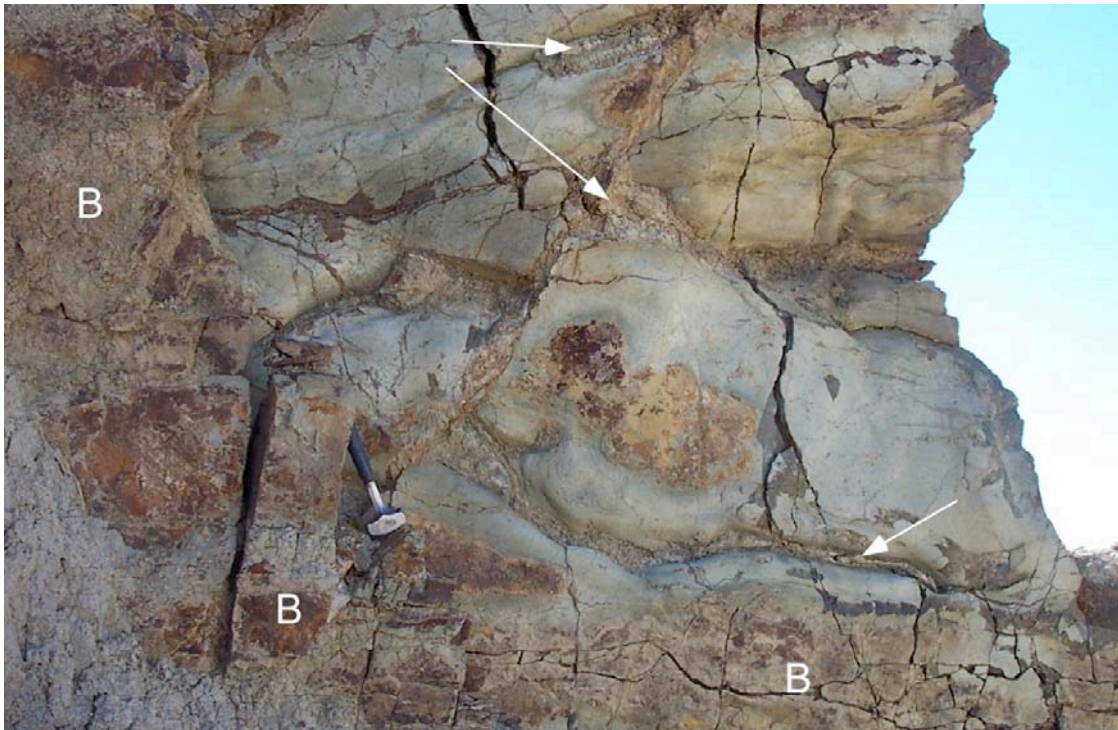


Figure 52: Billowed margin of the east-west-trending dike. Hammer rests on baked mudstone, which is also labeled “B.” Arrows point to invaginations filled with baked mudstone.

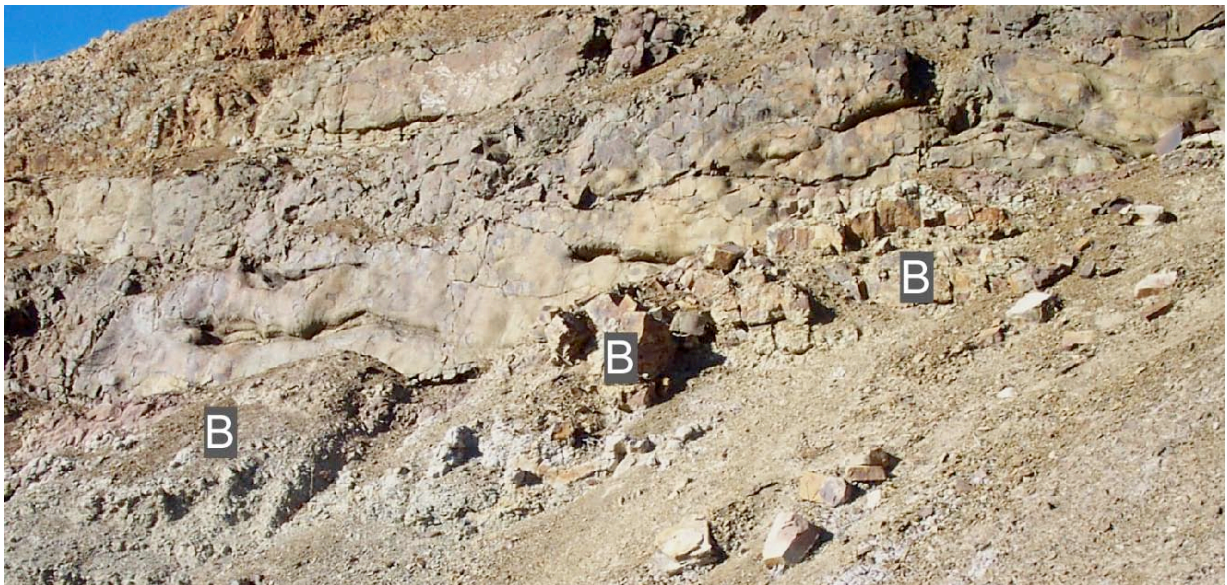


Figure 53: Elongate billows up to ≤ 5 m long on exposed margin of east-west-trending dike. B= baked mudstone.

Dike A is exposed for 250 m along a gully wall in the Black Peaks Formation (Figure 54). It generally trends east-northeast, although its trend is locally irregular. The main body

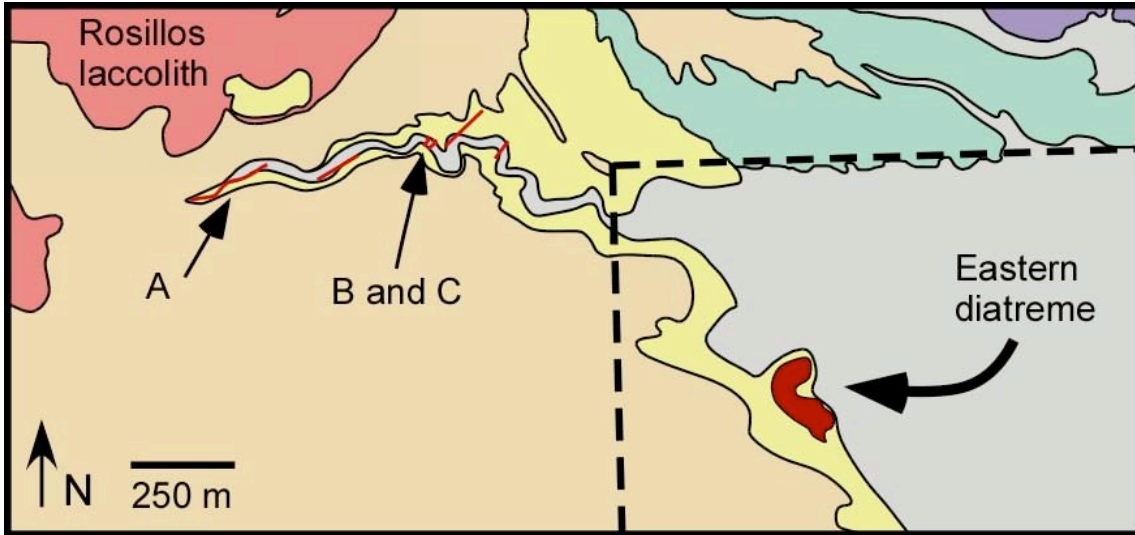


Figure 54: Map of southeastern part of Pitcock Ranch showing the drainage where six dikes occur. Thickness of dikes is not to scale. Dashed line shows the boundary between the ranch and Big Bend National Park. Individual dikes discussed in the text are labeled. See Figure 50 for an explanation of the geologic units.

of the dike pinches and swells and ranges between 1 to 4 m in thickness. It has variable dips either toward the north or south. In places, small fingers bifurcate from the main body and extend for less than a meter into the surrounding sediment. The contact between the dike and the host sediment is typically billowed and is marked by a baked zone 10–50 cm thick. Cusped invaginations 5–10 cm deep occupied by sediment separate billows that are 30–60 cm across. The dike has an aphanitic, vesicle-poor chilled margin nearly 5 cm thick, and thin-section study of the margin indicates it is marked by millimeter-scale billows developed between sediment and basalt (Figure 55). The cusped, fluidal margin is composed of palagonite altered to zeolites and green clay minerals. The quenched palagonite rim grades into a zone of tachylite, which subsequently grades into an intersertal groundmass texture.

This zonation is analogous to zones described in rims of extrusive pillow lavas (cf., Bryan, 1972; Melson and Thompson, 1973; Moore, 1975). In fact, Bryan (1972) suggested that thin dikes and sills might show similar zones to extrusive pillow lavas. Plagioclase microlites are flow-aligned parallel to the margin of the dike in the palagonite zone; however, their orientation becomes more irregular farther from the margin. Some of the plagioclase microlites in the palagonite and tachylite zones show swallowtail forms indicative of rapid aqueous quenching (Bryan, 1972).

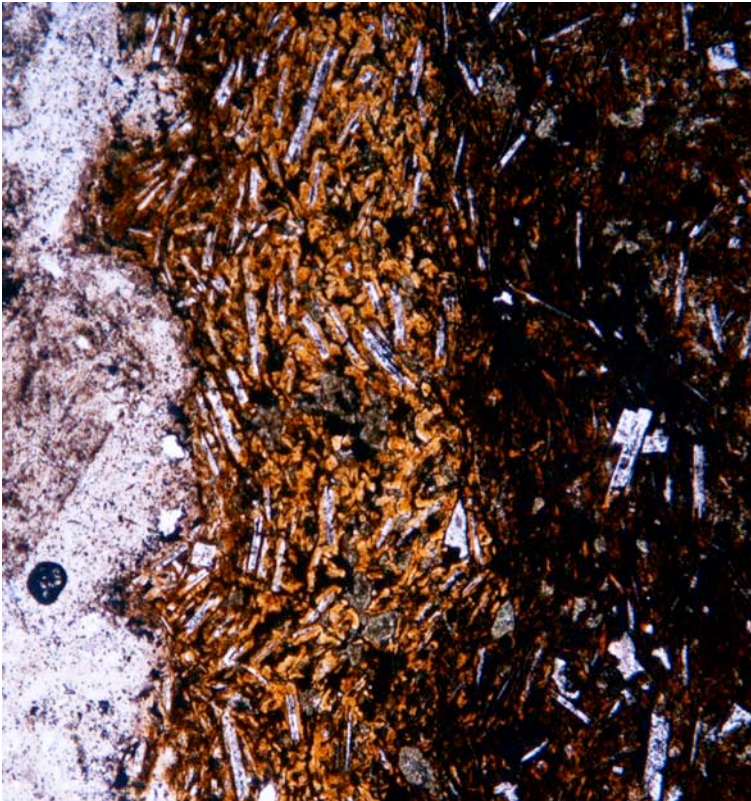


Figure 55: Photomicrograph of billowed margin of long east-west-trending dike. Host sediment is visible to the left. Palagonite rim (orange) grades into tachylite (dark). Note the flow-aligned plagioclase microlites, some showing swallowtail morphologies. Field of view is ~2 mm across.

In its easternmost outcrops, the dike becomes less discordant and changes into a pillowed sill before it is lost under Plio-Pleistocene alluvium. The pillowed area is ~10 m² in

areal extent and is composed of intrusive pillows that are in direct contact or are separated by tendrils or tongues of sediment 5–20 cm thick (Figures 56 and 57). The pillows are 20 cm to 2 m in diameter, and they decrease in size toward the periphery of the intrusion. Intrusive pillows show quenched margins 5–10 mm thick marked by distinct changes in color and subtle decreases in grain size of the groundmass. These margins likely consisted originally of sideromelane that has now been altered to fine-grained clay minerals. Pipe vesicles and amygdules up to 3 cm long are locally present and extend inward from the chilled margins (Figure 58). Small domains of blocky peperite composed of altered, angular hyaloclastite shards contained within disturbed mudstone are present along quenched pillow margins (Figure 59). Blocky peperite domains have jigsaw texture, and the hyaloclastite shards in the peperite are clearly derived by fragmentation of adjacent pillow rims.

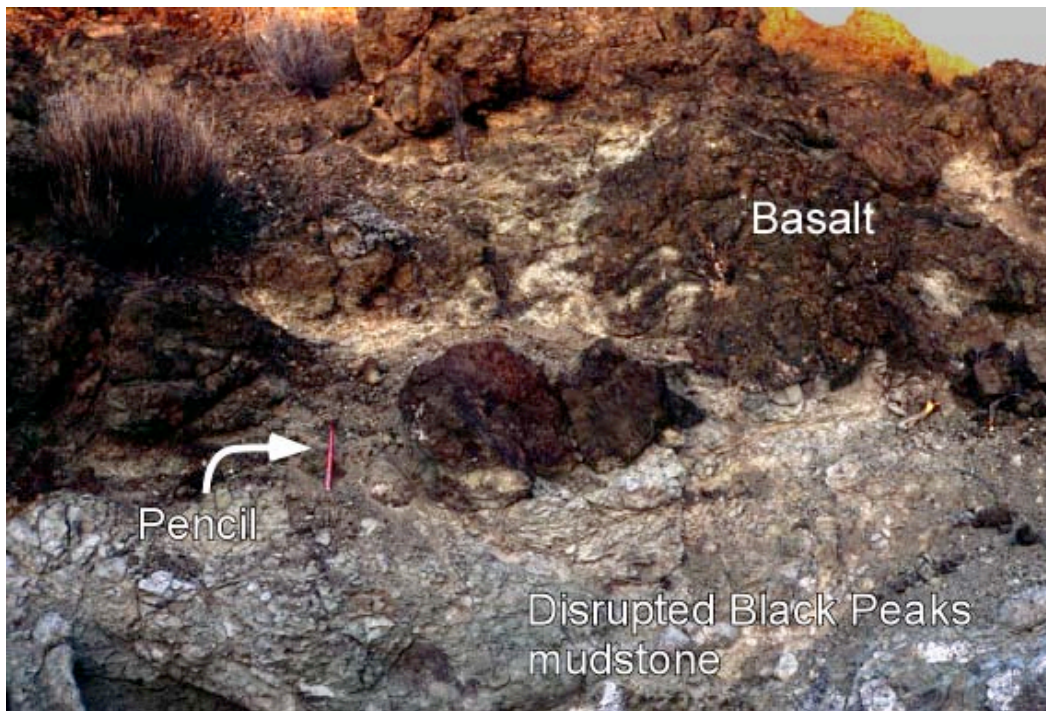


Figure 56: Pillowed area at the eastern outcrop of Dike A. Note well-defined intrusive pillow to the right of the pencil.

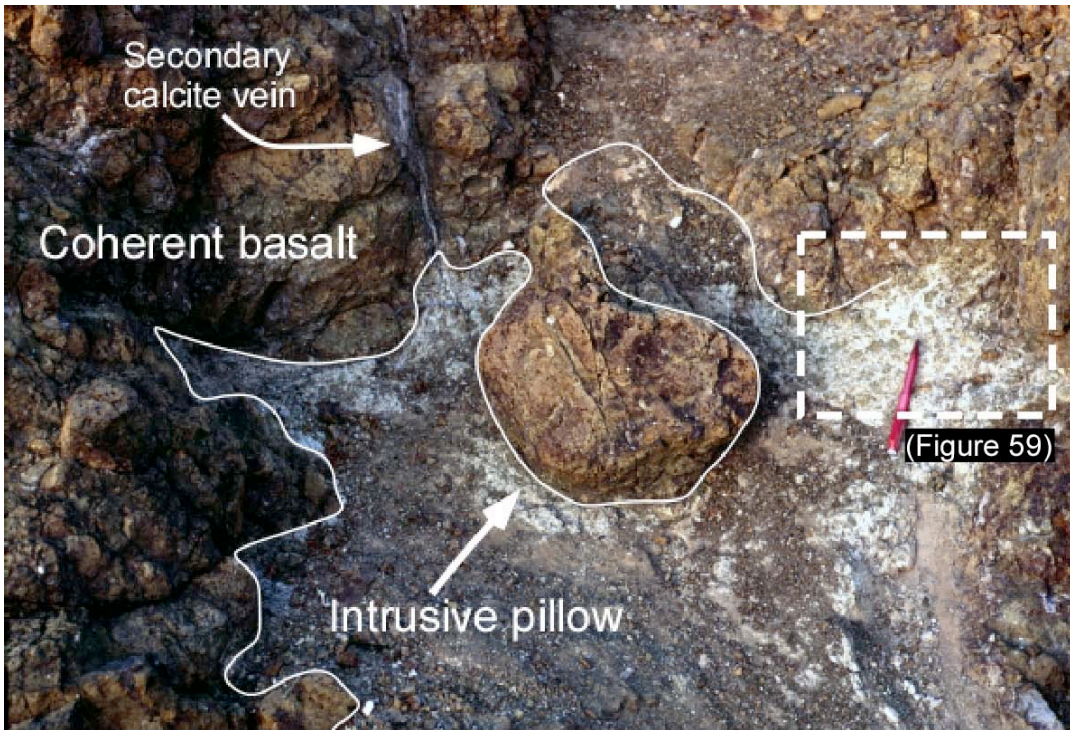


Figure 57: Small intrusive pillow visibly connected to coherent basalt. The intrusive pillow is surrounded by blocky peperite composed of mudstone and basalt. Pencil rests on well-exposed peperite shown in Figure 59.



Figure 58: Pipe vesicles developed along intrusive pillow margin.

Within the dike interior approximately 100 m west of the intrusive pillows, there is a zone of chaotically brecciated basalt ~50 cm across that shows only minor amounts of jigsaw-fit texture. This brecciated area is surrounded by coherent basalt and shows no apparent connection to the dike margins, although exposure is locally poor in this area. Near the brecciated area, irregular masses of white siltstone up to 30 cm across are isolated within the dike. The siltstone in these masses is also locally brecciated, as is the surrounding basalt.

Along the length of the dike, there are no major differences in properties of the host sediment, although intrusive geometries range from planar to billowed margins, and then to intrusive pillows associated with domains of blocky peperite. Blocky peperite within cusped invaginations between intrusive pillows formed primarily by quench fragmentation of basalt. Chaotic brecciation of pods of siltstone and some basalt indicates minor steam explosions disrupted material and may have contributed to the formation of small domains of peperite in some locations.

Two parallel basaltic dikes, labeled B and C (Figures 54 and 60) occur ~350 m downstream of the previously described dike. They are only exposed for a short distance before trending under cover but show excellent examples of features characteristic of all the dikes in the region. The billowed contact of the eastern dike (Dike C) is very well exposed due to recent erosion in the drainage. The southern contact between the dike and Black Peaks mudstone forms a 3-m-tall dry waterfall (Figure 61), which clearly shows the chilled margin of the dike, its billowed contact, and the adjacent baked zone in the mudstone.



Figure 59: View of blocky peperite composed of altered, angular hyaloclastite shards (green) and disturbed mudstone (white) present along quenched pillow margin (brown). Location shown in Figure 57.

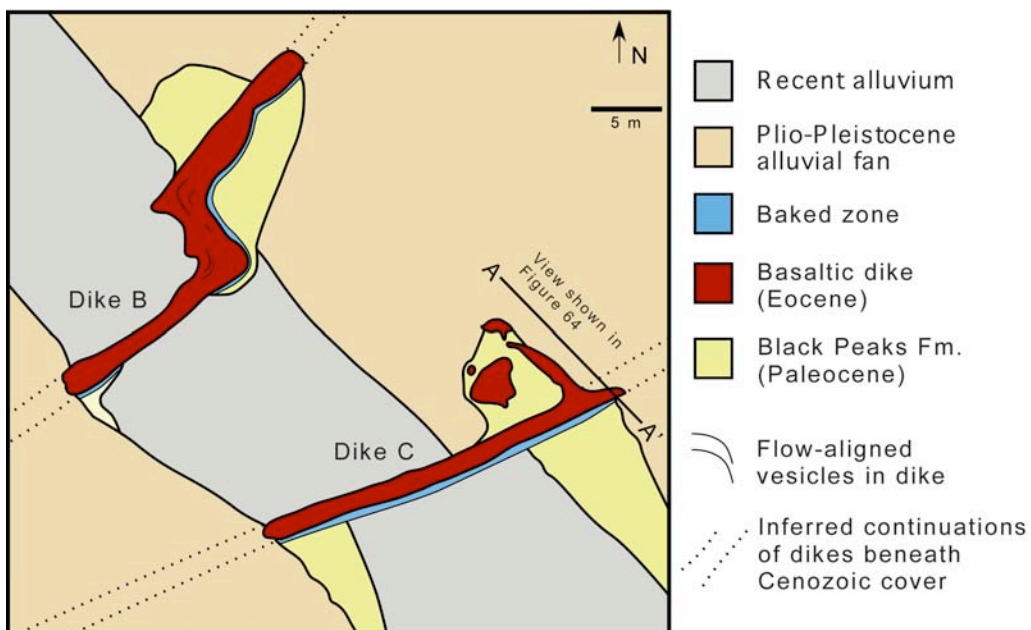


Figure 60: Tape-and-compass map of parallel Dikes B and C showing the irregular margins of the dikes, including a crook-shaped apophysis extending from Dike C.

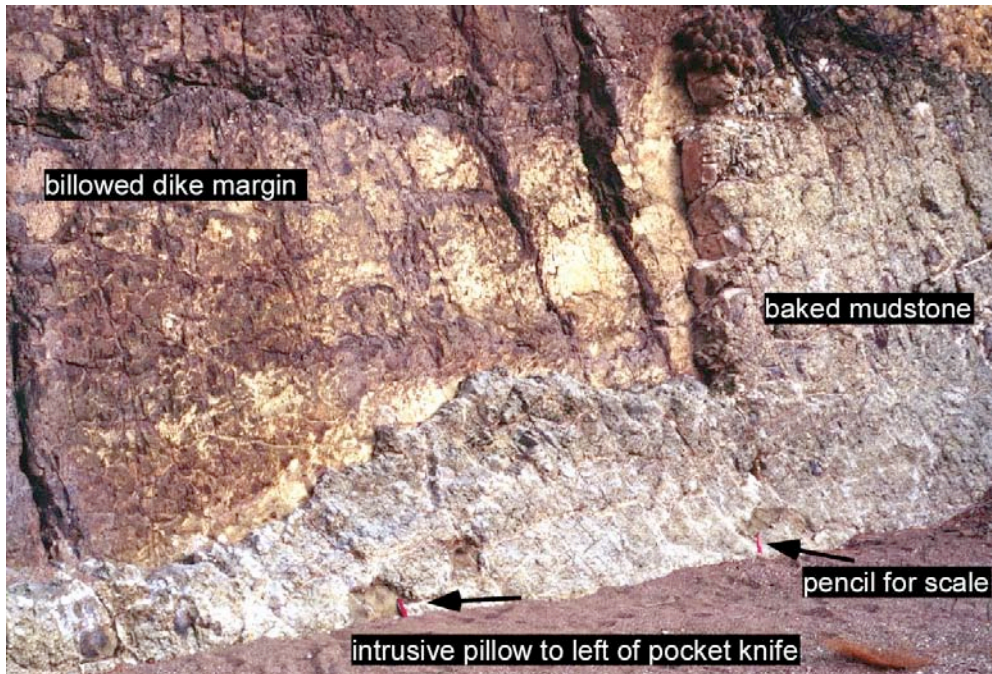


Figure 61: View of the dike margin exposed in the drainage showing the billowed margin of the dike, intrusive pillow extending from the dike, and baked mudstone.

Three orders of billows are visible on this exposed surface. First-order billows are approximately 1 m across and are separated by cusped invaginations 5–15 cm deep, which are filled with baked mudstone. These first-order billows are similar in size and shape to billows seen on many of the other dikes present in the study area. Second-order billows are superimposed upon first-order billows. Second-order billows are elongate parallel to the trend of the dike and tend to plunge gently to the east. They are on average 10 cm x 30 cm across and are separated by cusped invaginations 2–5 cm deep (Figure 62). Finally, third-order billows are superimposed on both first- and second-order billows (Figure 62). In some cases, they are elongate parallel to the trend of the dike, but in general they are equidimensional. The third-order billows are 5–10 cm in diameter and are separated by cusped invaginations 1–2 cm deep (Figure 63).

The baked zone is 20–30 cm thick and grades into poorly consolidated Black Peaks mudstone. The baked mudstone shows poorly developed columnar jointing perpendicular to the dike surface. Black Peaks mudstone is homogenous in this area and shows no internal stratification besides thick color banding; therefore, there is no evidence for destruction of bedding within a fluidized carapace along the contact (cf., Kokelaar, 1982).

Rare lobes of basalt up to 30 cm in diameter intrude up to 50 cm into the baked mudstone. The baked zone obscures the three-dimensional shapes of lobes. Nevertheless, these lobes are clearly intrusive pillows propagating away from the dike. A crook-shaped apophysis from Dike C intrudes the mudstone (Figures 60 and 64). The main body of the dike continues along strike for another 2 m until it is obscured by cover, which demonstrates that the entire dike does not bend at this point. The unusual curved shape of this apophysis is inferred to have formed when a sill-like tongue intruded into unconsolidated mudstone.



Figure 62: View of the billowed contact showing third-order billows superimposed upon second-order billows. Invaginations between some second-order billows are dashed. Pencil for scale.



Figure 63: View of third-order billows. Pencil for scale resting on baked mudstone (B) in cusped invagination between second-order billows.

Intrusive pillows occur near the sill-like tongue and have billowed, cusped margins with surrounding mudstone. Mudstone in these cusped invaginations is locally brecciated against the intrusive pillows. There is no evidence of mixing between mudstone and juvenile basaltic clasts; however, cusped intrusive contacts with brecciated mudstone may represent a precursor to the development of peperite. The unusual shape of the apophysis suggests that unconsolidated mudstone could not support the weight of the intruding basalt. The basalt subsided more rapidly the farther it was from the main body of the dike, until individual basaltic pods began to separate from the apophysis to form intrusive pillows. The pillows may, however, be connected to the apophysis in three dimensions.

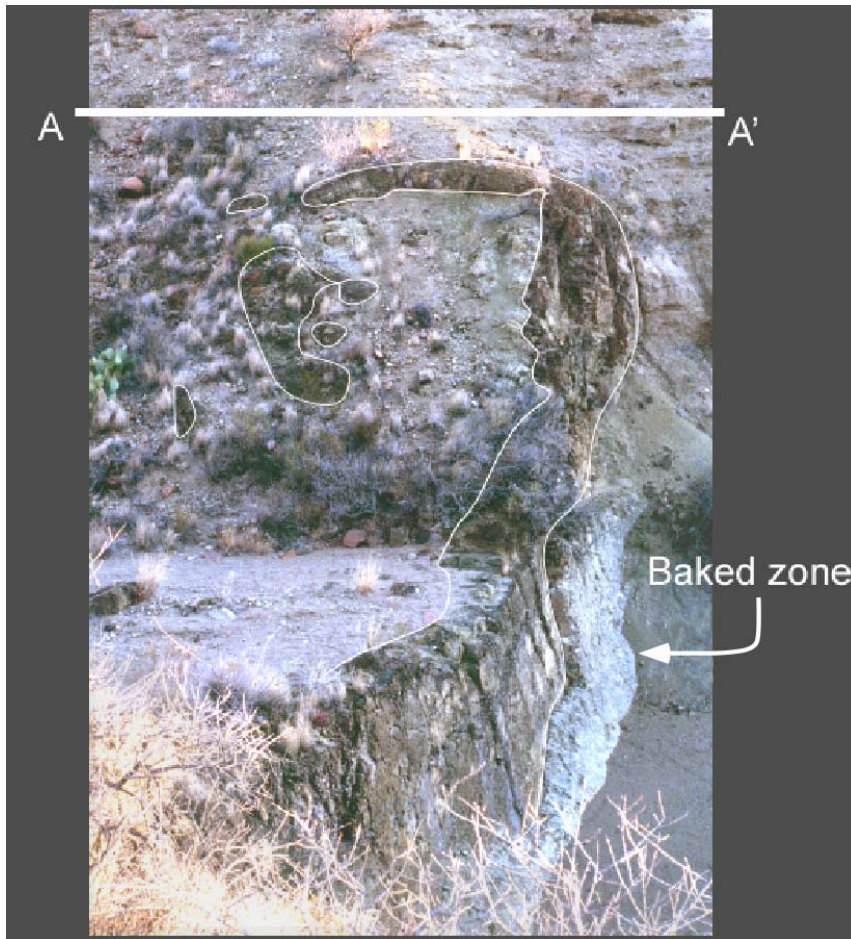


Figure 64: Irregular intrusive relationship, with a crook-shaped apophysis that extends from Dike C into Black Peaks mudstone. Position of line A–A' is shown on the tape-and-compass map in Figure 60. Dike margin and intrusive pillows are outlined.

Cottonwood Wash intrusion

An ellipsoidal, discordant basaltic intrusion crops out as a small hill 60 m by 15 m across in Cottonwood Wash on the Pitcock Ranch just north of Big Bend National Park (Figures 50 and 65). The presence of this intrusion was noted by Murray (1999) and Dennie (2001). The intrusion cuts color-banded Javelina mudstones but is surrounded by recent alluvium in Cottonwood Wash to the north, south, and east. It does not continue into the valley walls to the east or the west.

The intrusion is composed of coherent basaltic rock containing up to 10% calcite amygdules ≤ 1 cm in diameter. In the freshest basalt, phenocrysts of plagioclase and olivine (partly replaced by chlorophaeite) are set within a pilotaxitic groundmass comprising plagioclase, olivine, oxides, and abundant accessory apatite. Minor analcite is present intergrown with oxides. This rock is the least altered of any of the intrusions described so far, and much of the olivine is still fresh. In more altered parts of the intrusion, olivine is completely replaced by brown smectite, and secondary carbonate is abundant.

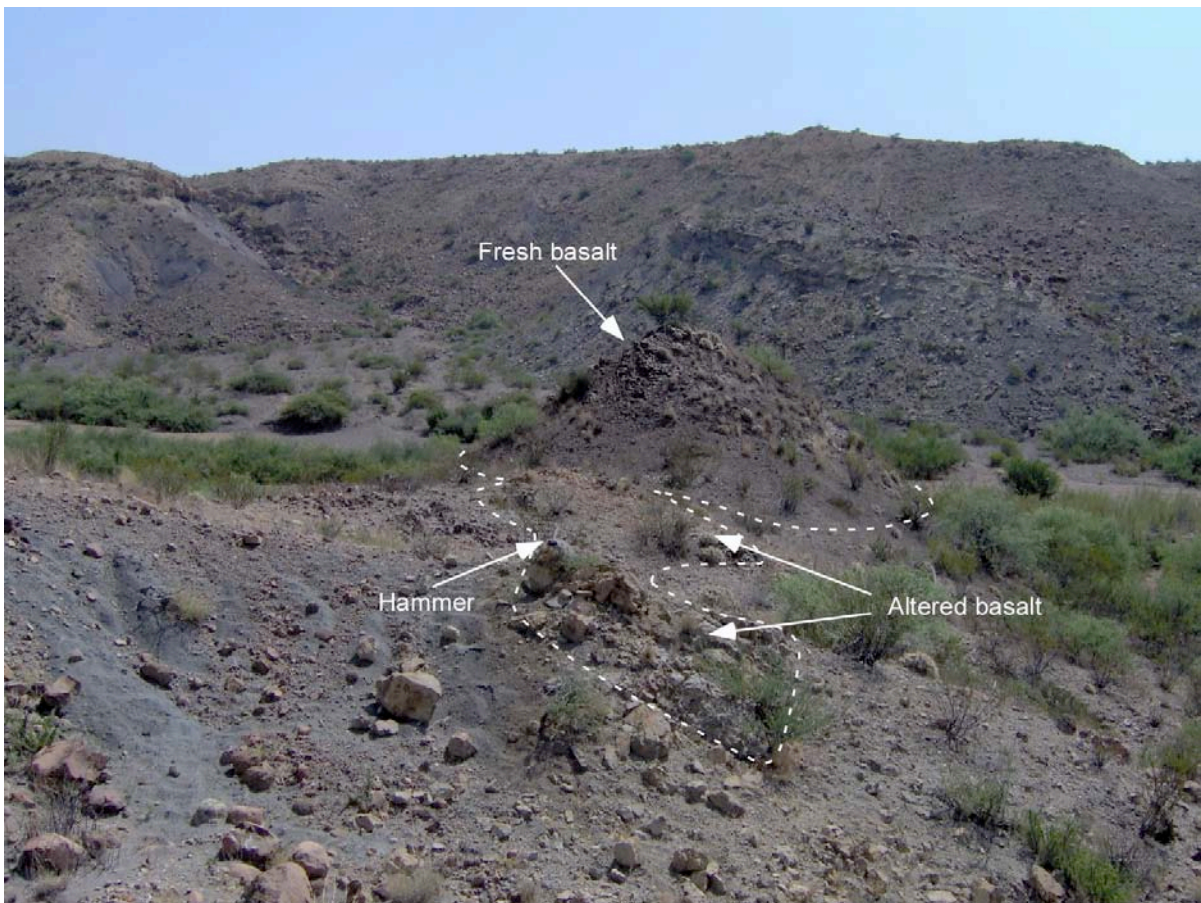


Figure 65: Outcrop of the Cottonwood Wash intrusion composed of domains fresh and altered basalt. Dashed lines approximate the intrusive contacts between basalt and Javelina mudstones. Hammer for scale.

Several tongues of sediment up to 3 m long that are composed of baked, light gray siltstone cut the intrusion. The sediment tongues contain ellipsoidal calcite amygdules ≤ 5 mm in diameter. In places, the baked siltstone shows well-developed micro-columnar jointing with columns ≤ 1 cm across that are perpendicular to the contact. Xenoliths of very fine-grained sediment with fluidal margins occur sparsely within the more altered basalt. The western contact between the basalt and Javelina mudstone is marked by a highly altered outcrop of indeterminate lithology in hand sample that is cut by numerous calcite veins. Petrographic analysis indicates the altered outcrop is composed of fine-scale globular peperite developed between the basalt and mudstone (Figure 66), although secondary carbonate locally replaces the sediment. Sub-millimeter fluidal basalt clasts are composed of altered sideromelane and contain hyalopilitic plagioclase microlites.

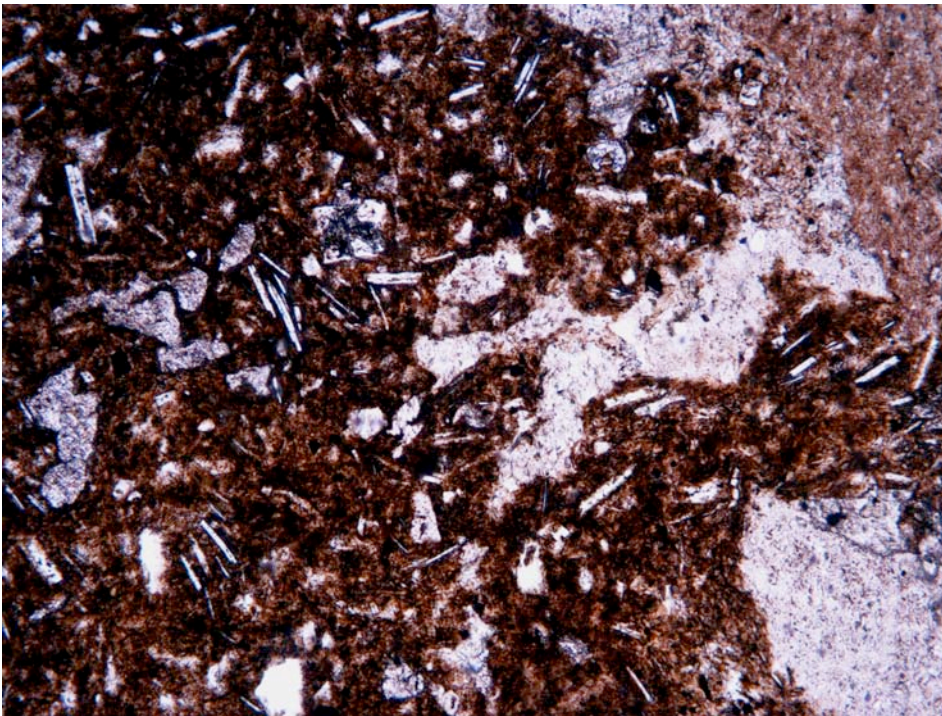


Figure 66: Photomicrograph of fine-scale globular peperite developed between altered basalt (dark) and Javelina mudstone (light to dark gray) in the Cottonwood Wash intrusion. Plane light; field of view is ~ 2 mm across.

Geochemistry

One focus of this study is to determine whether all of the basaltic intrusions shown in Figure 50 are genetically related. Petrographic studies indicate that the intrusions discussed so far are mineralogically similar, and the presence of titanite in the long, east-west-trending dike indicates alkaline affinities. Major- and trace-element geochemical analyses were used to further constrain the relationships between the intrusions.

Samples of the dikes and Cottonwood Wash intrusion are plotted in the total alkalis versus silica (TAS) diagram in Figure 67. Dikes A, B, and C located in the drainage on the southeastern part of Pitcock Ranch (samples A9b, A10a, A10b, respectively) plot in the trachybasalt field. This result must be treated with caution however, due to extensive alteration evident in thin section and reflected in the relatively high LOI values (Table 4). The fresh basalt from the Cottonwood Wash intrusion (C15) has slightly higher concentrations of both silica and alkalis, and plots in the basaltic trachyandesite field. This analysis is inferred to be reliable due to the lack of alteration in the sample. The long east-west-trending dike (D10) plots as a trachyandesite, which is consistent with the high percentage of plagioclase and low color index evident in thin section. This analysis is also interpreted to be valid due to the lack of alteration in the sample.

The dikes in the southeastern drainage and the Cottonwood Wash intrusion are tightly clustered in the alkaline basalt field on the Zr/TiO_2 vs. Nb/Y discrimination diagram (Figure 68). Based on the tight cluster of the samples, these intrusions likely formed from compositionally similar magmas, which suggests that the variation on the TAS diagram is due to major-element mobility during alteration. Therefore, the analysis of sample C15 from the fresh rock from the Cottonwood Wash intrusion can be viewed as the best estimate of the

original magma composition for the suite of intrusions in the southeastern portion of the Pitcock Ranch. The long east-west-trending dike (D10) plots in the alkaline basalt field in Figure 68, very near to the trachyandesite field, which nearly coincides with the TAS result and supports the inference that alteration had little effect on the mobile major elements in this sample.

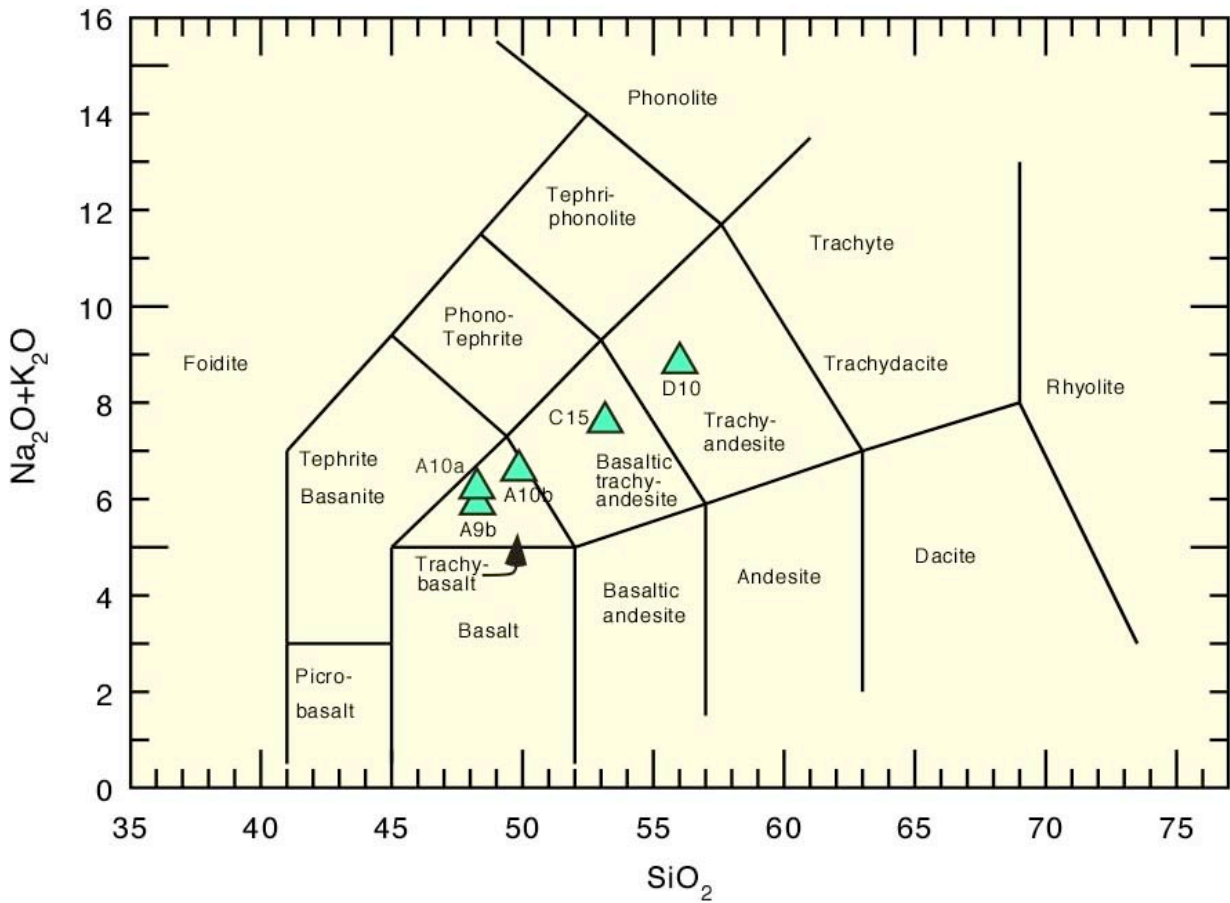


Figure 67: Analyses of samples from the dikes and Cottonwood intrusion plotted on total alkalis vs. silica (TAS) diagram (Le Bas et al., 1986).

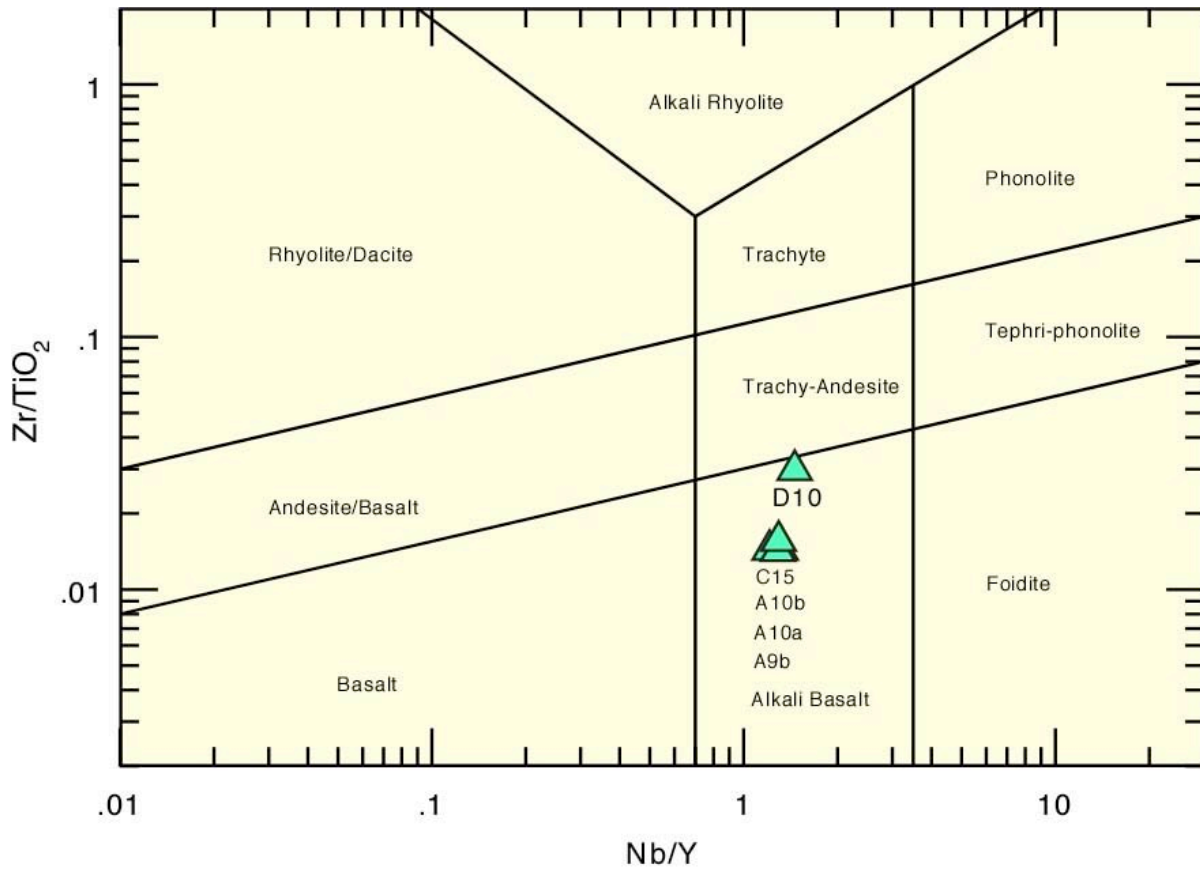


Figure 68: Analyses of samples from the dikes and Cottonwood Wash intrusion plotted on Zr/TiO_2 vs. Nb/Y discrimination diagram (Winchester and Floyd, 1977; revised by Pearce, 1996).

The spread in the data on the major-element variation diagrams shown in Figure 69 are interpreted to partly result from element mobility during alteration. However, the data are consistent with a petrogenetic connection between the more mafic intrusions and the more differentiated east-west-trending dike. All of these intrusions typically plot in alkaline to transitional, within-plate fields on other standard basalt discrimination diagrams using immobile trace elements (Figures 70 and 71). This result is consistent with the generally smooth, convex-upward patterns shown by the samples on normalized multi-element diagrams (Figures 72 and 73), which are typical of intraplate basalts (Wilson, 1989). The three samples of the dikes in the drainage on the southeastern portion of Pitcock Ranch have

anomalously low Rb and K concentrations on these diagrams, whereas the Cottonwood Wash intrusion and the east-west-trending dike do not show this feature. This result directly correlates with the degree of alteration evident in thin section for each sample. The samples all show strongly LREE-enriched patterns relative to chondrite, without negative Eu anomalies (Figure 74). These patterns are also typical for within-plate basalts (Wilson, 1989). The similarity in these patterns provides additional evidence for a genetic relationship between all these intrusions.

The long east-west-trending dike is a part of the dike swarm that was generated during the emplacement of the Christmas Mountains intrusive complex (Henry et al., 1989). Members of this dike swarm and the Christmas Mountains Gabbro have yielded K–Ar ages of ~44–40 Ma (Figure 51). Based on the similarities in trend between the dikes in the southeastern portion of the Pitcock Ranch and the east-west-trending dike, together with the geochemical evidence given above, all of these intrusions on the Pitcock Ranch are inferred to be related to the Christmas Mountains intrusive complex. Henry et al. (1989) do not report trace-element analyses in their study of the Christmas Mountains intrusive complex, so it has not been possible to make detailed geochemical comparisons between intrusions of the Christmas Mountains intrusive complex and the intrusions on the Pitcock Ranch.

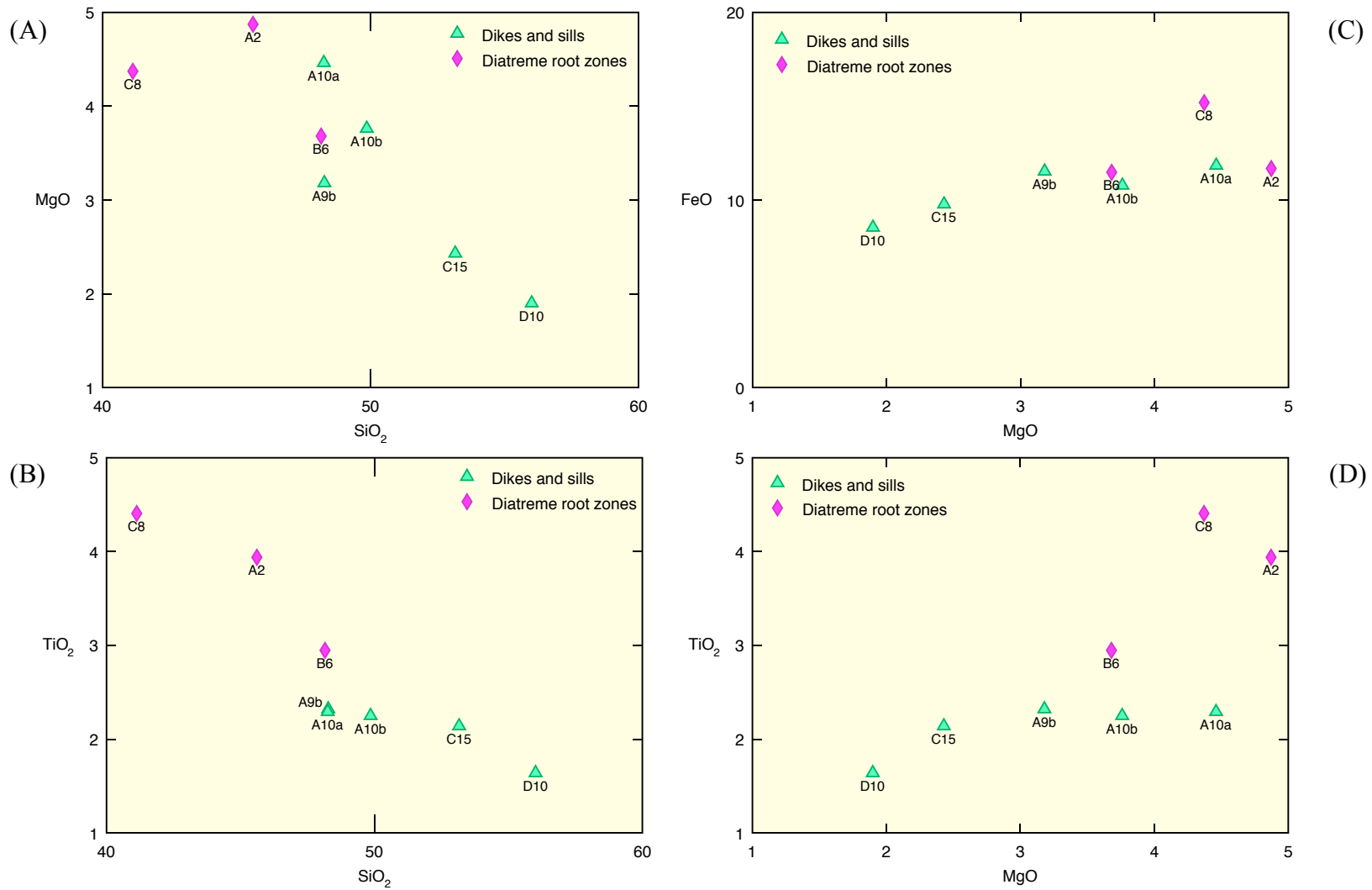


Figure 69: Major-element variation diagrams (in wt. %) for samples from the dikes, Cottonwood Wash intrusion, and diatreme root zones. Harker variation diagrams in A and B, Fenner variation diagrams in C and D.

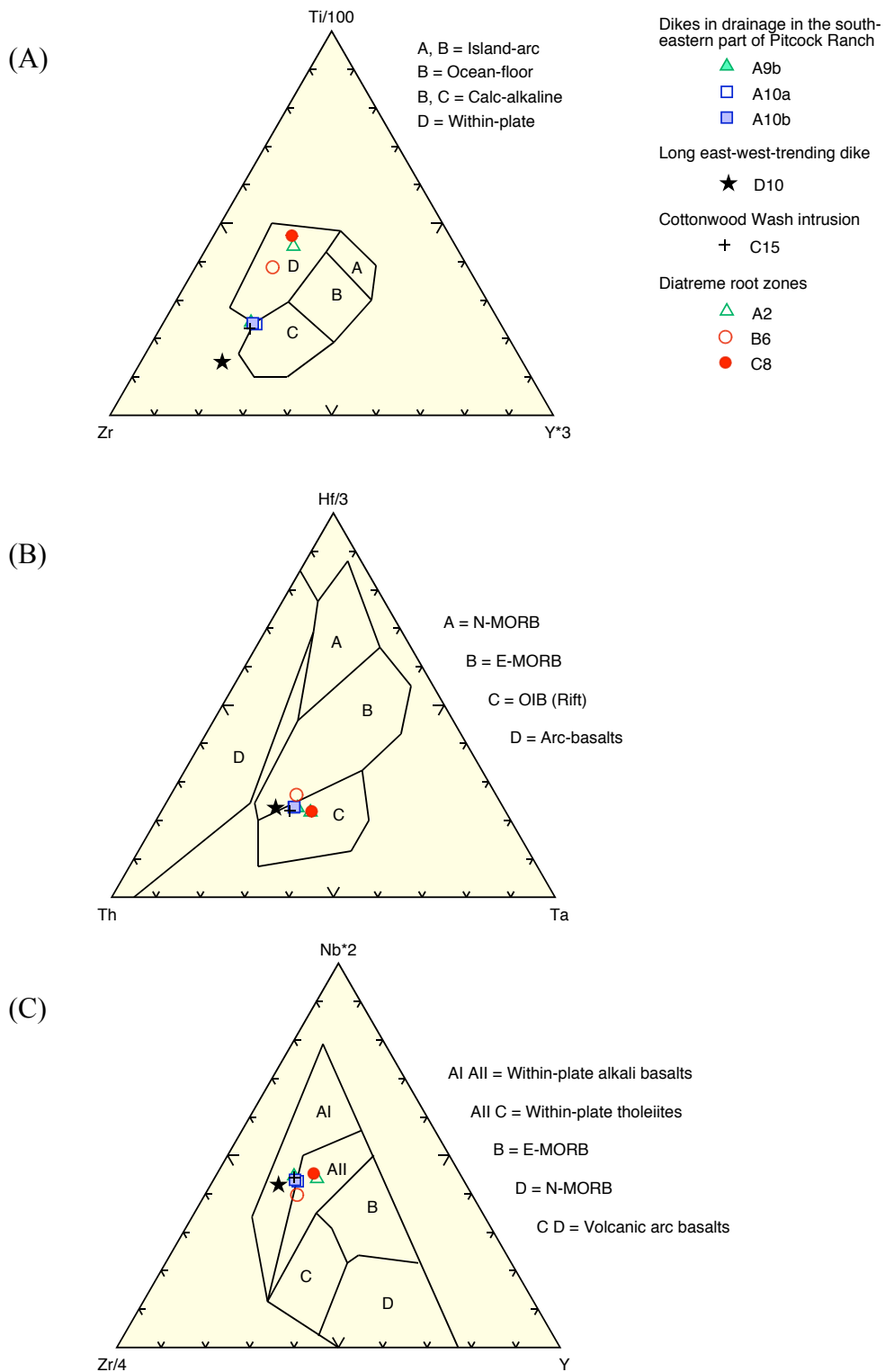


Figure 70: Analyses of samples from the dikes, Cottonwood Wash intrusion, and diatreme root zones plotted on standard trace-element discrimination diagrams. A from Pearce and Cann (1973), B from Wood (1980), C from Meschede (1986).

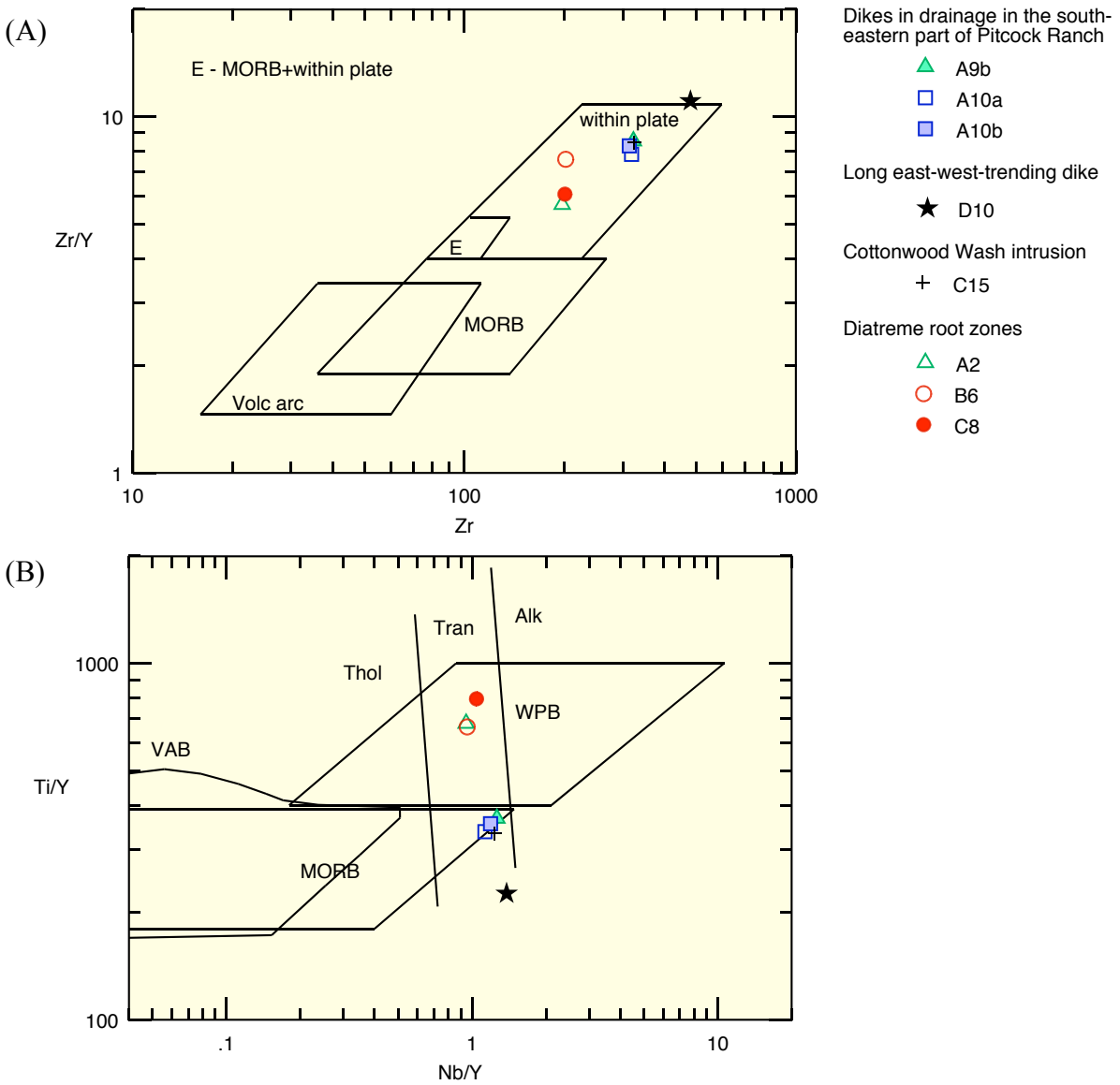


Figure 71: Analyses of samples from the dikes, Cottonwood Wash intrusion, and diatreme root zones plotted on other standard trace-element discrimination diagrams. A from Pearce (1982), B from Pearce and Norry (1979).

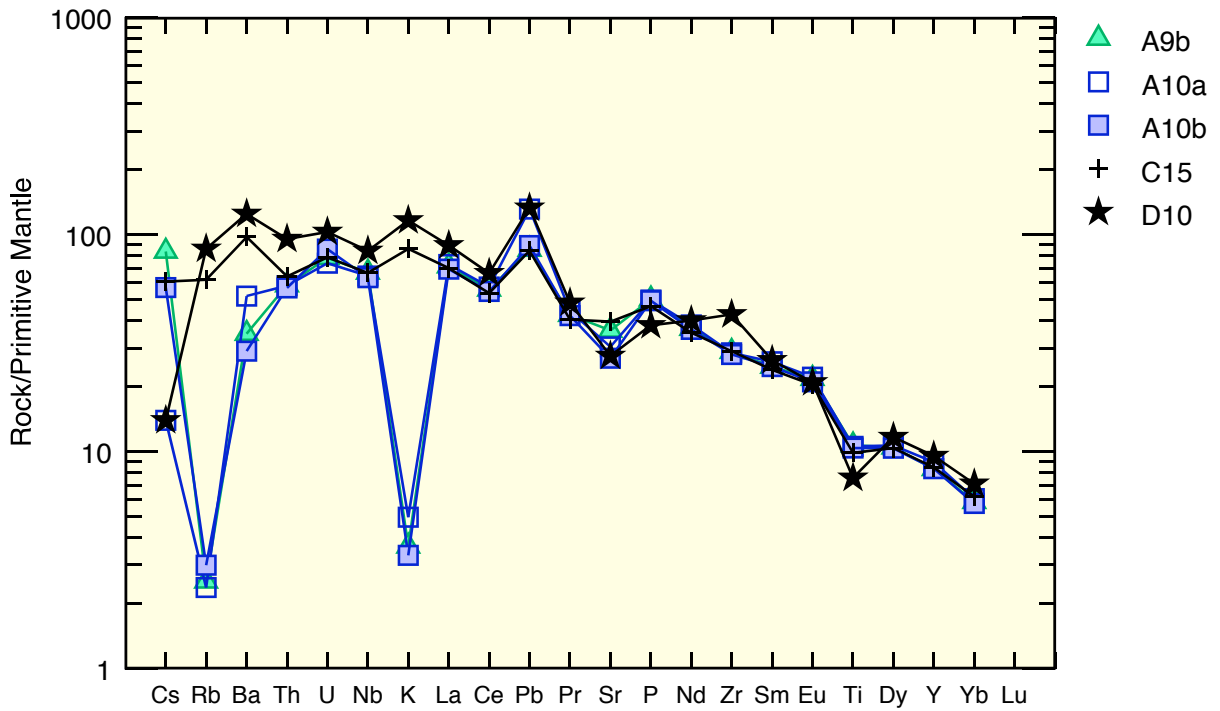


Figure 72: Multi-element diagram normalized to primitive mantle (Sun and McDonough, 1989) for samples from the dikes and Cottonwood Wash intrusion.

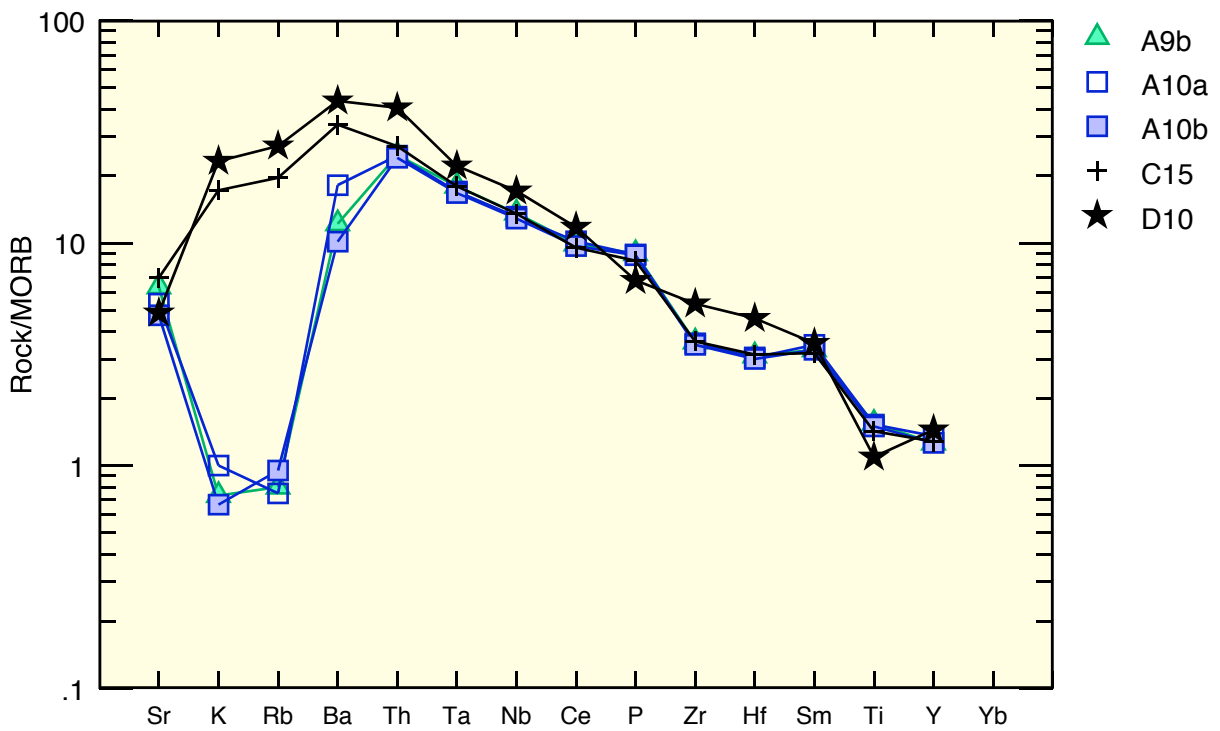


Figure 73: Multi-element diagram normalized to MORB (Pearce, 1982) for samples from the dikes and Cottonwood Wash intrusion.

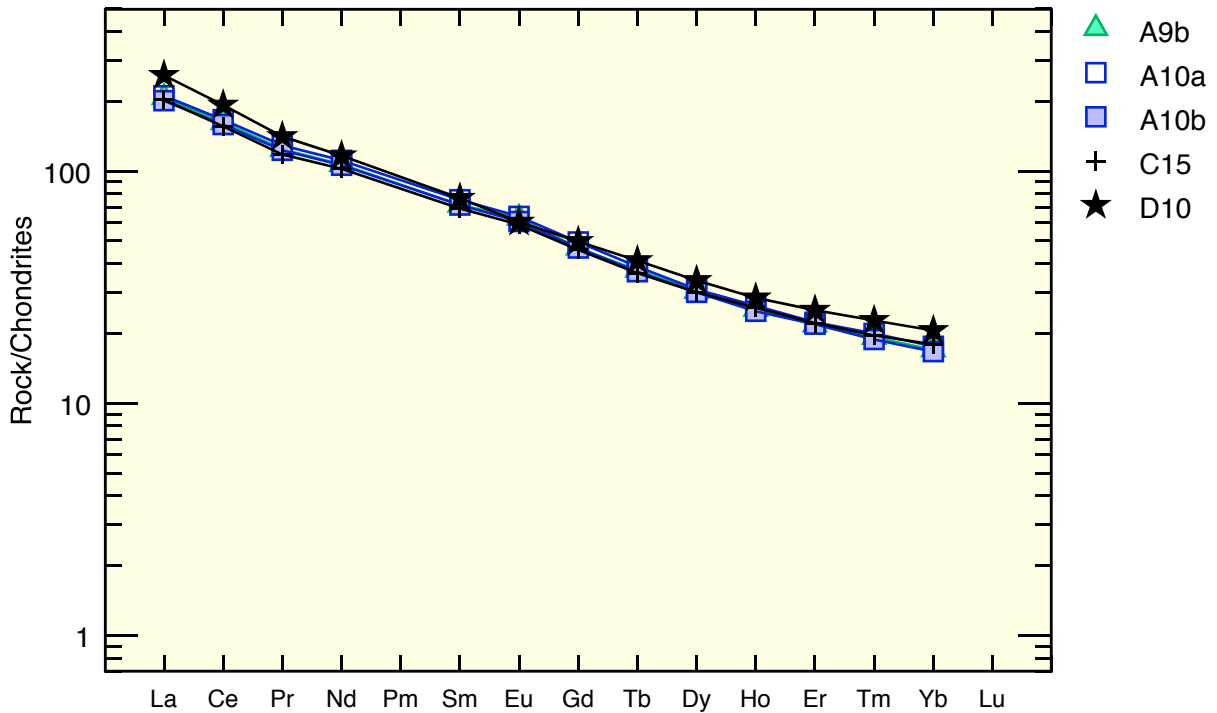


Figure 74: Chondrite-normalized REE abundances for samples from the dikes and Cottonwood Wash intrusion. Normalizing values from Sun and McDonough (1989).

Conclusion

Study of these intrusions has offered insight into several physical processes that occur along contacts between intrusive magma and unconsolidated sediment. Although many of the dikes only show cusped, billowy margins, others show progressive development of billowy contacts, intrusive pillows, and peperite.

In one thermite experiment designed by Wohletz (2002) to model molten fuel-coolant interactions during phreatomagmatic eruptions, a thermite dike intruded downward into wet, unconsolidated sand. Dike surfaces were marked by bulbous irregularities, akin to billowed margins described in this study. Dadd and Van Wagoner (2002) described field occurrences of pillow-like appendages that extend downward from a mafic lava flow that overlies mudstones. These pillow-like appendages have chilled margins, which show small amounts

of quench fragmentation in some cases. Dadd and Van Wagoner (2002) interpreted the pillow-like bodies to have formed due to gravitational instabilities between the mafic lava flow and underlying, unconsolidated wet sediment. Even though billows examined during the present study look like the load features described by Dadd and Van Wagoner (2002), they formed on vertical dike walls as well as along lower horizontal sill contacts; therefore, these features are not solely created by gravitational instability. Instead they are related to intrusive processes and may be explained by Rayleigh-Taylor instabilities, which form along the boundary between fluids with different densities. If the system is at equilibrium, this boundary is planar. Acceleration of either fluid creates a Rayleigh-Taylor instability where the denser fluid invades into and displaces the less dense fluid, ultimately forming a penetrative to undulatory, irregular fluid-fluid contact (Pollard et al., 1975).

Hooten and Ort (2002) described dikes and other hypabyssal intrusive bodies associated with peperite. Zones of blocky to globular peperite tended to form in areas where dikes developed irregular bulbs against the surrounding fine-grained siltstone. Hooten and Ort (2002) interpreted the peperite to record an initial, weakly explosive stage in molten fuel-coolant interaction, where physical properties of the system prevented explosive eruptions. Some of the peperite domains described in the present study are also inferred to have been created by relatively minor steam explosions coupled with quench fragmentation; however, relatively high confining pressures are interpreted to have prevented explosive activity in this situation.

Table 4: Geochemical data for dikes, Cottonwood Wash intrusion, and diatreme root zones.

Normalized major elements (wt. %)*

	A2**	A9b	A10a	A10b	B6**	C8**	C15	D10
SiO₂	45.62	48.28	48.26	49.86	48.16	41.14	53.16	56.01
TiO₂	3.937	2.32	2.291	2.249	2.946	4.404	2.139	1.64
Al₂O₃	17.00	18.54	18.50	18.31	18.56	18.72	17.55	17.37
FeO	11.67	11.52	11.83	10.77	11.47	15.18	9.77	8.53
MnO	0.263	0.283	0.245	0.153	0.153	0.529	0.194	0.154
MgO	4.87	3.18	4.46	3.76	3.68	4.37	2.43	1.90
CaO	10.83	8.89	7.11	7.24	9.42	10.02	6.14	4.74
Na₂O	3.29	5.78	6.07	6.49	4.00	3.80	5.00	5.32
K₂O	1.10	0.11	0.15	0.10	1.08	0.26	2.59	3.50
P₂O₅	1.424	1.096	1.087	1.079	0.524	1.575	1.019	0.832
LOI	3.59	7.27	7.24	8.50	2.48	7.92	2.21	1.54
Total***	95.52	91.05	90.98	89.85	95.65	89.60	95.74	97.42

CIPW Norms

	A2**	A9b	A10a	A10b	B6**	C8**	C15	D10
Q	-	-	-	-	-	-	-	-
or	6.50	0.65	0.89	0.59	6.38	1.54	15.31	20.68
ab	24.39	36.22	37.64	41.95	28.62	19.80	41.79	45.02
an	28.37	24.32	22.79	20.53	29.50	33.25	17.79	13.18
ne	1.87	6.87	7.44	7.03	2.83	6.69	0.28	-
di	13.29	10.69	4.51	7.00	11.59	5.19	1.10	4.18
hy	-	-	-	-	-	-	-	1.08
ol	13.05	13.80	18.84	15.13	12.94	19.54	12.34	10.08
mt	5.71	3.36	3.32	3.26	4.27	6.39	3.10	2.38
il	7.48	4.41	4.35	4.27	5.60	8.36	4.06	3.11
ap	3.30	2.54	2.52	2.50	1.21	3.65	2.36	1.93
Total	103.94	102.86	102.30	102.26	102.94	104.41	102.13	101.64
AN	53.77	40.17	37.71	32.86	50.76	62.68	29.87	22.65

Trace elements (ppm)

	A2**	A9b	A10a	A10b	B6**	C8**	C15	D10
Ni	13	5	5	5	11	16	6	4
Cr	12	4	4	3	3	13	4	3
V	193	64	65	63	284	202	69	54
Ga	21	20	19	20	24	19	21	25
Cu	16	8	6	7	13	15	7	6
Zn	91	101	103	103	101	97	102	111
Bi	1	1	1	3	2	1	2	2
La	44.52	49.17	49.98	47.59	27.56	41.92	48.11	61.27
Ce	93.73	99.14	101.9	97.00	56.30	88.73	95.30	117.8
Pr	11.79	11.79	12.26	11.67	6.90	11.02	11.20	13.39

Trace elements (continued)

	A2**	A9b	A10a	A10b	B6**	C8**	C15	D10
Nd	51.89	49.86	51.93	49.50	29.88	48.91	47.8	54.38
Sm	11.83	10.93	11.51	10.93	7.13	11.03	10.56	11.70
Eu	3.89	3.64	3.70	3.52	2.43	3.66	3.41	3.50
Gd	10.45	9.58	10.17	9.59	6.51	9.87	9.41	10.23
Tb	1.45	1.40	1.45	1.38	0.97	1.38	1.36	1.54
Dy	7.58	7.71	7.86	7.63	5.46	7.35	7.65	8.59
Ho	1.34	1.44	1.49	1.41	1.02	1.30	1.46	1.61
Er	3.11	3.60	3.70	3.63	2.50	3.07	3.67	4.17
Tm	0.40	0.49	0.51	0.48	0.34	0.39	0.5	0.58
Yb	2.20	2.89	2.99	2.84	2.00	2.15	3.05	3.50
Lu	0.32	0.45	0.45	0.43	0.30	0.32	0.46	0.54
Ba	380	244	364	203	710	252	681	871
Th	3.12	4.97	4.94	4.83	2.75	3.15	5.45	8.11
Nb	32.9	47.73	45.95	45.08	25.41	34.55	47.46	59.99
Y	34.8	37.86	40.72	37.96	26.62	33.19	38.46	43.42
Hf	4.69	7.46	7.34	7.23	4.88	4.83	7.57	11.01
Ta	2.39	3.24	3.07	3.02	1.73	2.44	3.24	4.00
U	0.96	1.64	1.55	1.80	0.89	1.06	1.65	2.16
Pb	2.44	6.05	9.31	6.32	3.28	2.74	5.98	9.43
Rb	14.0	1.6	1.5	1.9	16.2	1.3	39.3	54.6
Cs	1.23	0.66	0.11	0.45	1.1	0.26	0.48	0.11
Sr	1213	763	641	568	713	941	838	582
Sc	13.8	10.1	10.9	10.3	21.6	15.8	14.1	13.8
Zr	197	323	319	314	202	201	325	480

*Normalized to 100% on a volatile-free basis.

**Samples with asterisks (A2, B6, and C8) are from diatreme root zones described in the following section. Samples A9b, A10a, A10b are from dikes in the drainage in the southeastern portion of the Pitcock Ranch. Sample C15 comes from the Cottonwood Wash intrusion. Sample D10 is from the east-west-trending dike.

***Total before normalization.

Peperitic diatreme root zones

Three diatreme root zones crop out as discordant intrusions in the study area (Figure 50). The two western diatreme root zones occur in the Javelina Formation. In this area, the Javelina Formation is primarily composed of multicolored, structureless mudstones with less common, laterally discontinuous channel sandstones. The eastern diatreme root zone occurs in similar, structureless, color-banded mudstones of the Black Peaks Formation.

All of the diatreme root zones contain lithologically similar, relatively coarse-grained intergranular hypabyssal basalt to plagioclase-phyric diabase with calcite-filled amygdules up to 5 cm in diameter. The intrusions contain similar mineral assemblages, with plagioclase phenocrysts up to 1 cm in length and ophitic to subophitic titanaugite showing purple pleochroism (Figure 75). Secondary, very fine-grained green and brown phyllosilicates replace olivine, but a few cores of olivine remain in samples from the eastern diatreme root zone. Titanaugite shows slight alteration of the same type. All of the diatreme intrusions also contain Fe, Ti-oxides, interstitial analcite, abundant accessory apatite, and secondary carbonate. Analcite is generally considered a low-temperature zeolite mineral; however, its occurrence in regular intergrowths with other groundmass minerals in these intrusions (Figure 75) suggests it is a primary igneous phase. Titanaugite indicates an alkaline affinity for the intrusions.

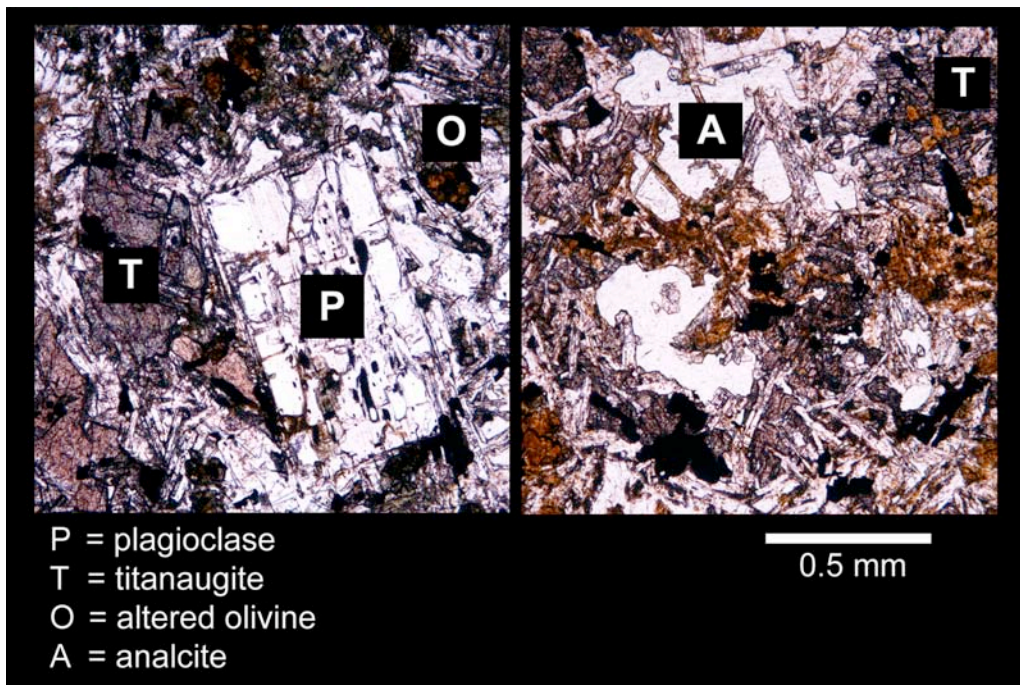


Figure 75: Photomicrographs of diabase in the eastern diatreme root zone showing characteristic mineral assemblage of titanaugite, altered olivine, plagioclase, and analcite. Plane light.

Major- and trace-element concentrations and CIPW norms for samples from the diatreme root zones are given in Table 4. All three samples show normative nepheline, consistent with the alkaline composition inferred from the petrography. The three samples show substantial variations in silica on the TAS diagram (Figure 76) and plot in the fields of tephrite/basanite (C8), basalt (A2), and trachybasalt (B6). The sample from the western diatreme root zone (C8) has a very low silica value. The pyroxenes in this sample are completely replaced by carbonate, and plagioclase is partially replaced by carbonate as well. Consequently, the alteration is inferred to have resulted in significant major-element mobility. Conversely, samples from the main diatreme root zone (A2) and the eastern diatreme root zone (B6) do not show significant alteration in thin section, although olivine has been replaced by secondary clay minerals in both samples.

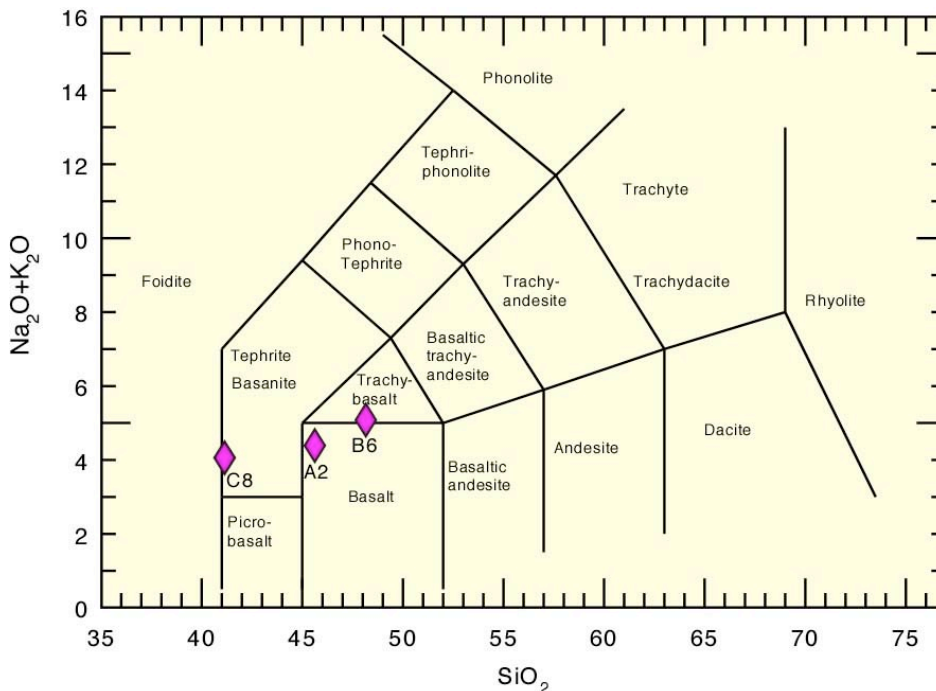


Figure 76: Analyses of samples from the diatreme root zones plotted on total alkalis vs. silica (TAS) diagram (Le Bas et al., 1986).

The samples plot in close proximity in the alkaline basalt field on the Zr/TiO₂ vs. Nb/Y discrimination diagram (Figure 77) and in within-plate fields on other trace-element

discrimination diagrams (Figures 70 and 71). They lack negative Ta–Nb anomalies on normalized multi-element diagrams (Figures 78 and 79), which is typical of intraplate basalts. Sample C8 shows distinct negative Rb and K anomalies, which is consistent with the high degree of alteration in that sample. All three samples have LREE-enriched patterns typical of within-plate basalts (Figure 80).

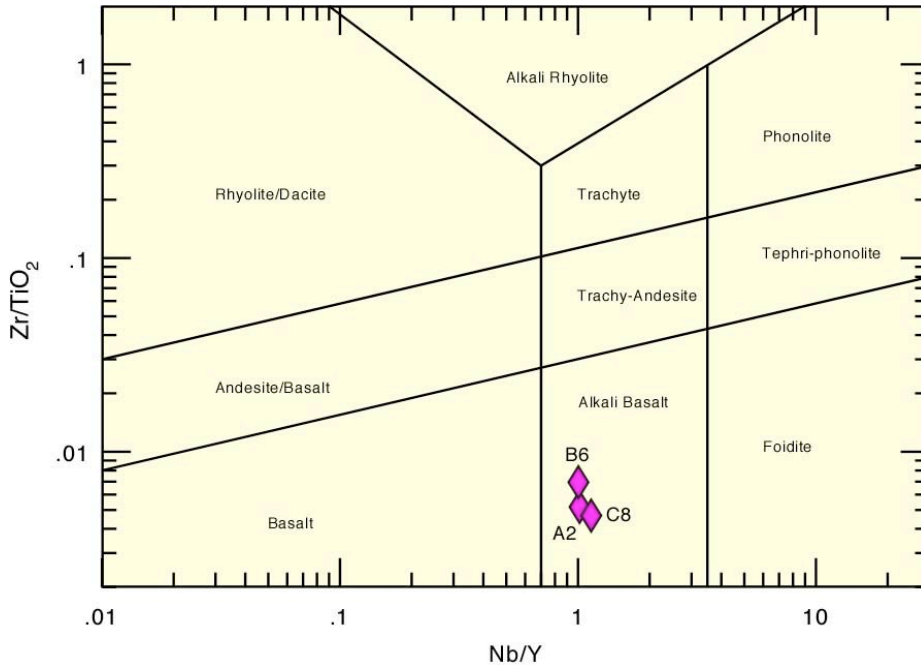


Figure 77: Analyses of samples from the diatreme root zones plotted on Zr/TiO₂ vs. Nb/Y discrimination diagram (Winchester and Floyd, 1977; revised by Pearce, 1996).

The petrographic and geochemical similarities between the samples from the three diatreme root zones suggest that the basaltic rocks in the root zones are parts of a compositionally related suite. The samples show substantial amounts of spread on major-element variation diagrams (Figure 69), but little significance can be attached to the trends on those diagrams due to the limited number of samples and high degree of alteration evident in thin section in sample C8. Samples from the diatreme root zones and from the other studied intrusions on the Pitcock Ranch show generally similar patterns on normalized multi-element

diagrams and also have similar chondrite-normalized REE patterns. They plot in similar fields in trace-element discrimination diagrams but are generally not tightly clustered with the other samples. As already discussed, the dikes on the Pitcock Ranch are inferred to be part of the Christmas Mountains dike swarm. Although basalts from the diatreme root zones are not compositionally identical to the dikes, they are also interpreted to be related to the Christmas Mountains intrusive complex because of their close geographic proximity to the dikes and because they show strong petrographic affinities to mafic rocks in the Christmas Mountains intrusive complex, including the presence of titanite and analcite (cf., Henry et al., 1989). Therefore, all the mafic to intermediate intrusions on the Pitcock Ranch are considered to have an age of ~44–40 Ma.

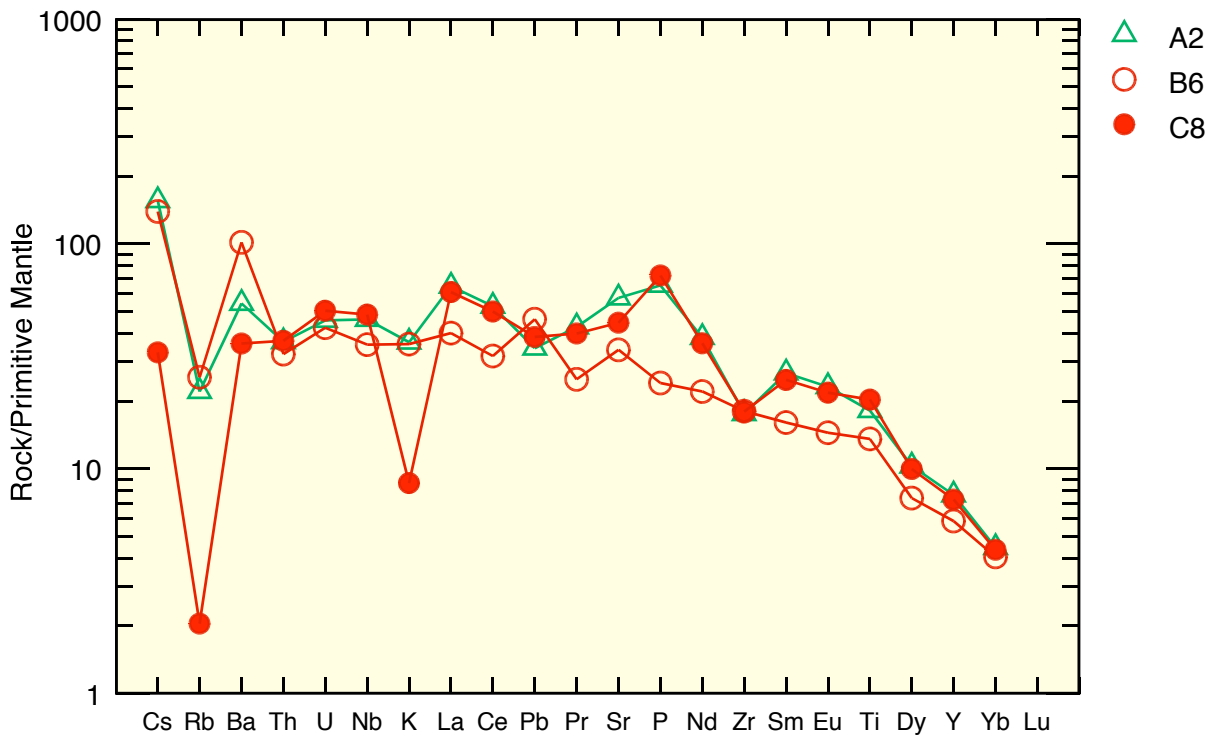


Figure 78: Multi-element diagram normalized to primitive mantle (Sun and McDonough, 1989) for samples from the diatreme root zones.

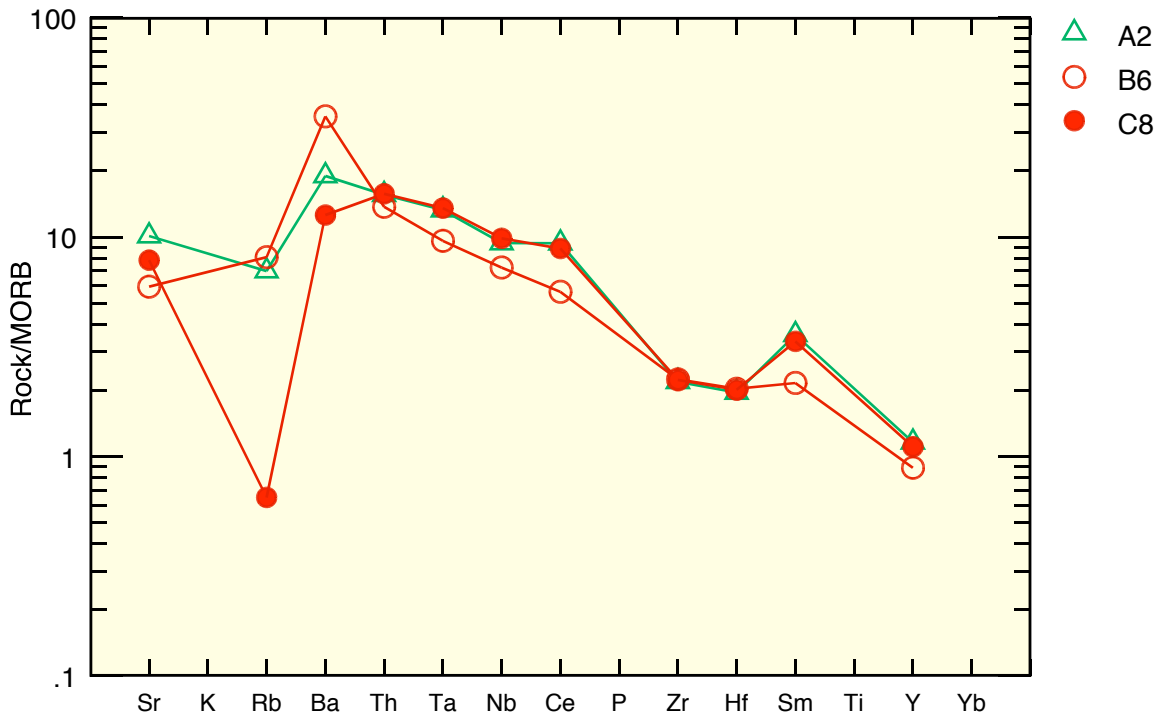


Figure 79: Multi-element diagram normalized to MORB (Pearce, 1982) for samples from the diatreme root zones.

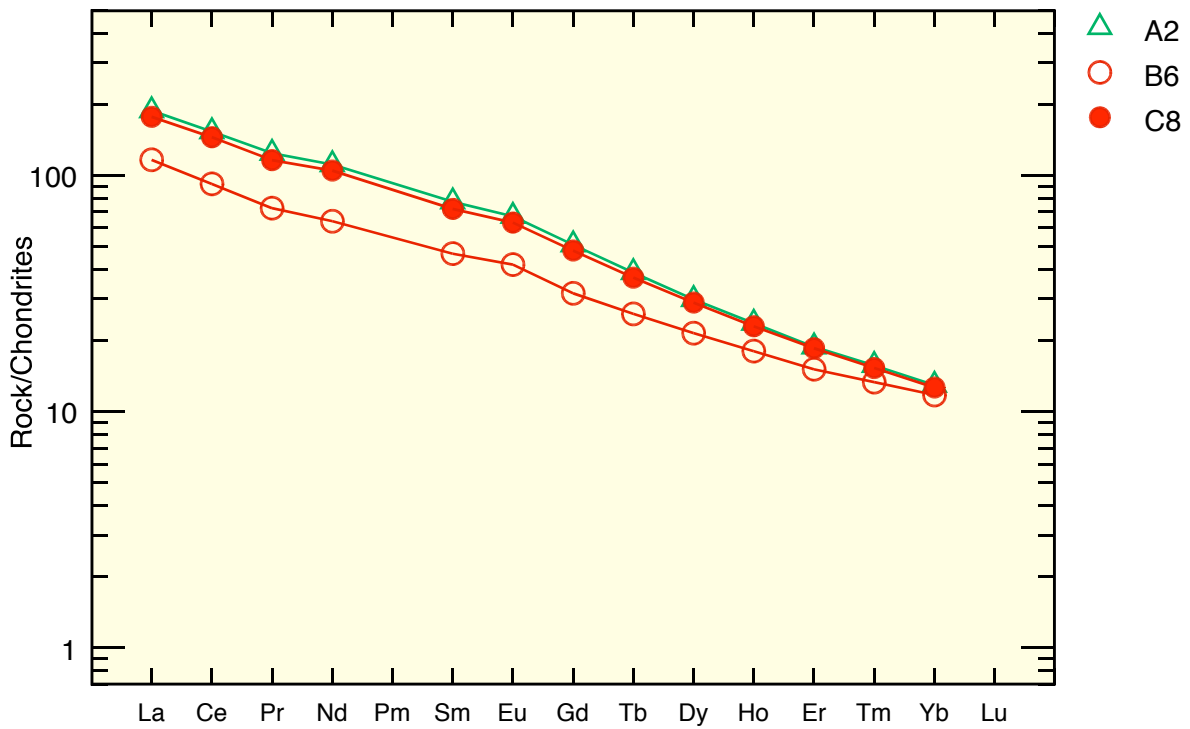


Figure 80: Chondrite-normalized REE abundances for samples from the diatreme root zones. Normalizing values from Sun and McDonough (1989).

Main diatreme root zone and associated intrusions

An intrusive body ~70 m across crops out in the Upper Cretaceous Javelina Formation on the Pitcock Ranch (Figure 81). The intrusion has a complicated internal structure composed of igneous and clastic components (Figure 82). It consists primarily of coarse-grained basalt similar in composition and phenocryst content to the other diatremes discussed in this study. Basalt along the intrusive margins contains $\leq 15\%$ calcite amygdules ≤ 5 cm in diameter, whereas basalt in central portions of the intrusion is much less amygdaloidal.

Color-banded Javelina mudstones are adjacent to most parts of the intrusion. A lenticular, moderately well-sorted, subangular, medium-grained, calcite-cemented quartzarenite showing trough cross-bedding is in contact with the northeastern portion of the intrusion. The contact between the basalt and sandstone is sharp and shows no evidence of faulting or fluidization. Recent colluvium obscures contact relations along the eastern and southwestern margins of the intrusion; however, where it is well exposed, the contact between mudstone and basalt is commonly complex and is marked by localized patches of microglobular peperite composed of quench-fragmented basalt set within a mudstone matrix (Figure 83). A mappable domain of microglobular peperite ~10 m across extends into the intrusion from the northern margin. Tendrils of mudstone also pervade basalt near the intrusive contacts and extend well into the intrusion. Along the northwestern side of the intrusion, ovoid intrusive pillows of basalt ≤ 2 m in diameter occur in Javelina mudstones within 10 m of the contact. The intrusive pillows are sparsely to nonvesicular and lack chilled margins. Pockets of centimeter-scale microglobular peperite occur between some intrusive pillows. Mudstone within the zone of intrusive pillows shows evidence that it was disturbed

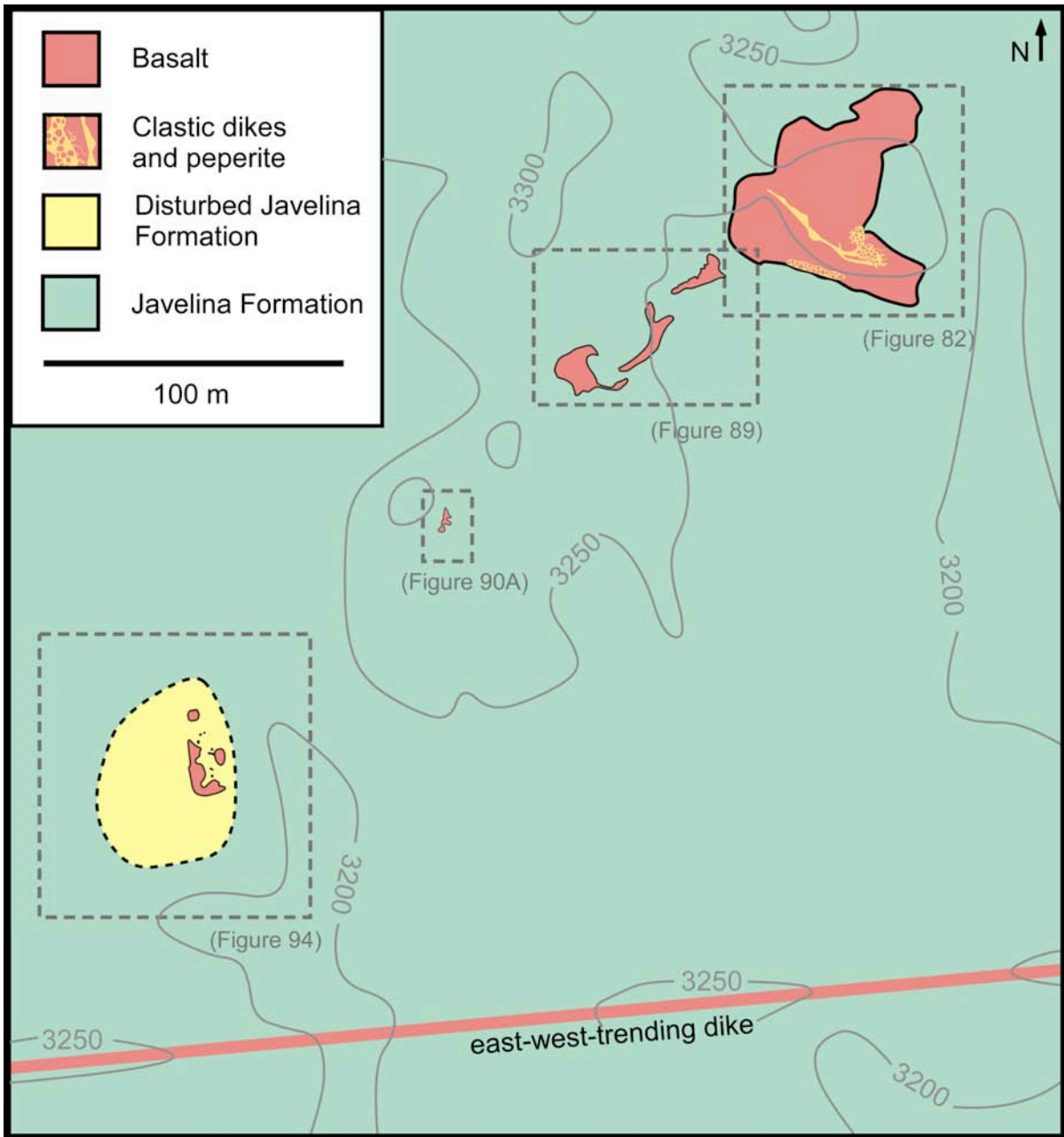


Figure 81: Geologic map of the western diatreme root zones and associated intrusions. Location shown in Figure 50. Contours in feet.

by processes related to the formation of the intrusion. Discontinuous bodies of disturbed sandstone typically up to 2 m across occur within this disturbed zone; three larger sandstone bodies are also present near or within this zone (Figure 82). Some sandstone bodies are massive, while others show soft-sediment deformation of bedding. Well-rounded sandstone,

limestone, and chert cobbles ≤ 10 cm in diameter occur in places within Javelina mudstone in this area. These cobbles also appear in another area near the southwestern contact as shown in Figure 84. Data from a clast count from the southwestern area is shown in Table 5. The clast populations are not similar to conglomerates previously described in the Javelina Formation by Lehman (1985, 1991), which are primarily composed of paleocaliche nodules. Instead, the clast populations are similar to conglomerate of the Eocene Hannold Hill Formation, which occurs higher in the sequence in the region.

Conglomerate domains with clast proportions similar to those in the mudstone occur in three locations within the main intrusion (Figure 82). A pillar composed primarily of Hannold Hill conglomerate is exposed in the northeastern corner of the intrusion. It is in contact with disturbed Javelina mudstone on the west and poorly exposed basalt on the east, north, and south. The conglomerate is composed of well-rounded pebbles and cobbles of sandstone, limestone, and chert chaotically arranged within a dark mud matrix. Ovoid masses of basalt 10–40 cm across intrude the conglomerate. In places, thin basalt tendrils surround pebbles and cobbles, forming conglomerate-hosted peperite. In some cases, the basalt incorporates the pebbles and cobbles as xenoliths. The second and third areas of conglomerate-hosted peperite are poorly exposed because they are covered by scree dominantly composed of sandstone, limestone, and chert cobbles derived from in situ weathering of the conglomerate-hosted peperite.

Domains of dispersed to closely packed globular peperite occur in four general locations near or along the southern and eastern margins of the intrusion. These areas are composed of ellipsoidal to subangular bodies of basalt ≤ 1 m in diameter, separated by

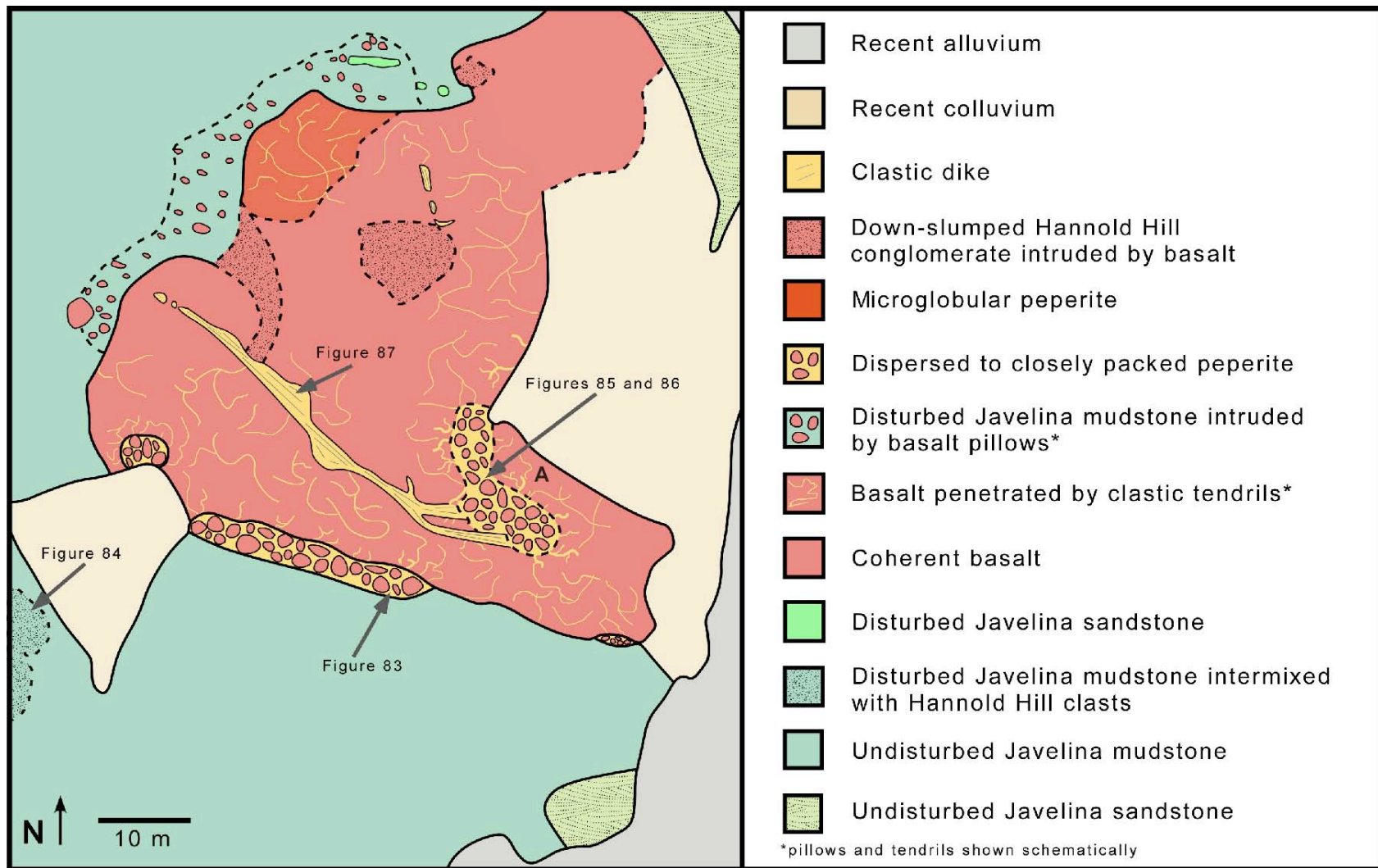


Figure 82: Tape-and-compass map of the main diatreme root zone on the Pitcock Ranch. Location shown in Figure 81. A = Location of U–Pb zircon sample.

Table 5: Clast counts of conglomerate.

Location	Clast size (mm)	Total # of clasts	Limestone clasts	Chert clasts	Mixed clasts*	Sandstone clasts
Hannold Hill conglomerate at the Canoe syncline	> 64	1	1 (100%)	0	0	0
	32–64	33	18 (55%)	6 (18%)	4 (12%)	5 (15%)
	16–32	105	62 (60%)	19 (18%)	13 (12%)	11 (10%)
	< 16	87	51 (58%)	28 (32%)	4 (5%)	4 (5%)
Main diatreme root zone	> 64	0	0	0	0	0
	32–64	8	3 (38%)	4 (50%)	1 (12%)	0
	16–32	125	98 (78%)	21 (17%)	0	6 (5%)
	< 16	75	57 (76%)	17 (23%)	0	1 (1%)
Western diatreme root zone **	> 64	2	2 (100%)	0	0	0
	32–64	32	21 (66%)	3 (9%)	3 (9%)	5 (16%)
	16–32	86	69 (80%)	4 (5%)	4 (5%)	9 (10%)

Clast counts were performed in a 1 m² area by passing all of the clasts in that area through sieves. Clasts too large to pass through the respective sieve were counted and classified.

* Mixed clasts are composed of limestone and chert.

** Did not count clasts that were smaller than the M4 sieve.



Figure 83: Microglobular peperite composed of basalt (dark) and Javelina mudstone (white) developed along the intrusive contact of the main diatreme root zone. Location shown in Figure 82.

massive sediment that shows no internal structure (Figures 85 and 86). The sediment contains angular basalt clasts up to 5 cm across that are similar in composition to the basalt within the diatreme as a whole and are widely dispersed within a finer clastic matrix. Thin-section study indicates that the matrix is dominantly composed of terrigenous mud, with silt- to sand-sized grains of quartz, chert, feldspar, and sparse basalt shards. The matrix is unlike nearby Javelina quartzarenites.



Figure 84: Limestone, chert, and sandstone cobbles weathering out of disturbed Javelina mudstone near the southeastern margin of the diatreme root zone. Location shown in Figure 82. View is looking southwest toward pillowed intrusion described in text. Color-banded Javelina mudstone is visible in the background.



Figure 85: Globular peperite formed when basalt (dark) intruded into and mixed with wet, unconsolidated sediment (light). Location shown in Figure 82.

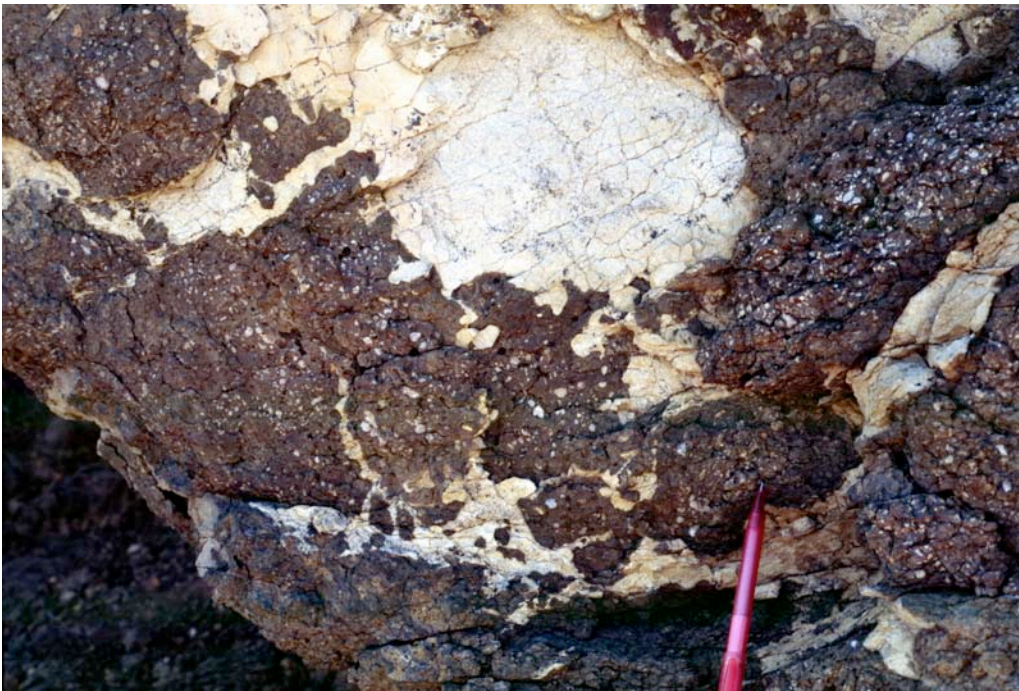


Figure 86: Smaller scale globular peperite consisting of basalt (dark) and unconsolidated sediment (light). Location shown in Figure 82.

Clastic tendrils ≤ 15 cm thick extend into the surrounding basalt along contraction cracks that typically propagate away from the domains of dispersed to closely packed peperite. These tendrils are similar in shape to the mudstone tendrils that extend from the outer contact of the intrusion. However, the clastic tendrils derived from domains of globular peperite contain silt- to sand-sized material with grain-size changes defining a diffuse lamination parallel to the margins of the tendrils. Nonvesicular shards of basalt ≤ 5 cm across also occur in these tendrils.

A well-indurated clastic dike ~ 40 m long and ≤ 3 m thick cuts through the intrusion and trends approximately northwest-southeast (Figure 87). The clastic dike does not extend to the margins of the intrusion, at least at the present level of exposure. It is composed of



Figure 87: Clastic dike with discontinuous internal layering that parallels the margin of the dike. Location shown in Figure 82. In area of photo, dike crops out as a ridge extending above more easily weathered basalt.

matrix-supported sand- to pebble-sized grains of feldspar, quartz, and scoriaceous to vesicular, altered basalt (listed in increasing abundance). It also contains subrounded mudstone cobbles, wood fragments ≤ 30 cm long aligned parallel to the margins of the dike, and angular, cobble-sized clasts of vesiculated basalt. The dike shows discontinuous, locally discordant layering defined by slight grain-size and color changes that parallels the margins of the dike (Figure 87).

The clastic dike bifurcates at its southeastern end into two parts, which then connect with numerous smaller clastic dikes. These smaller dikes have irregular to tabular morphologies and discordantly cut through both coherent basalt and peperite domains within the intrusion.

An inclined pillowed dike extends to the southwest from the main intrusion (Figures 81, 84, 88, and 89). The dike does not connect to the main intrusion at the current level of



Figure 88: Inclined pillowed dike that extends from the main diatreme root zone. View looking toward the southwest. Note the distinct color banding in surrounding Javelina mudstones.

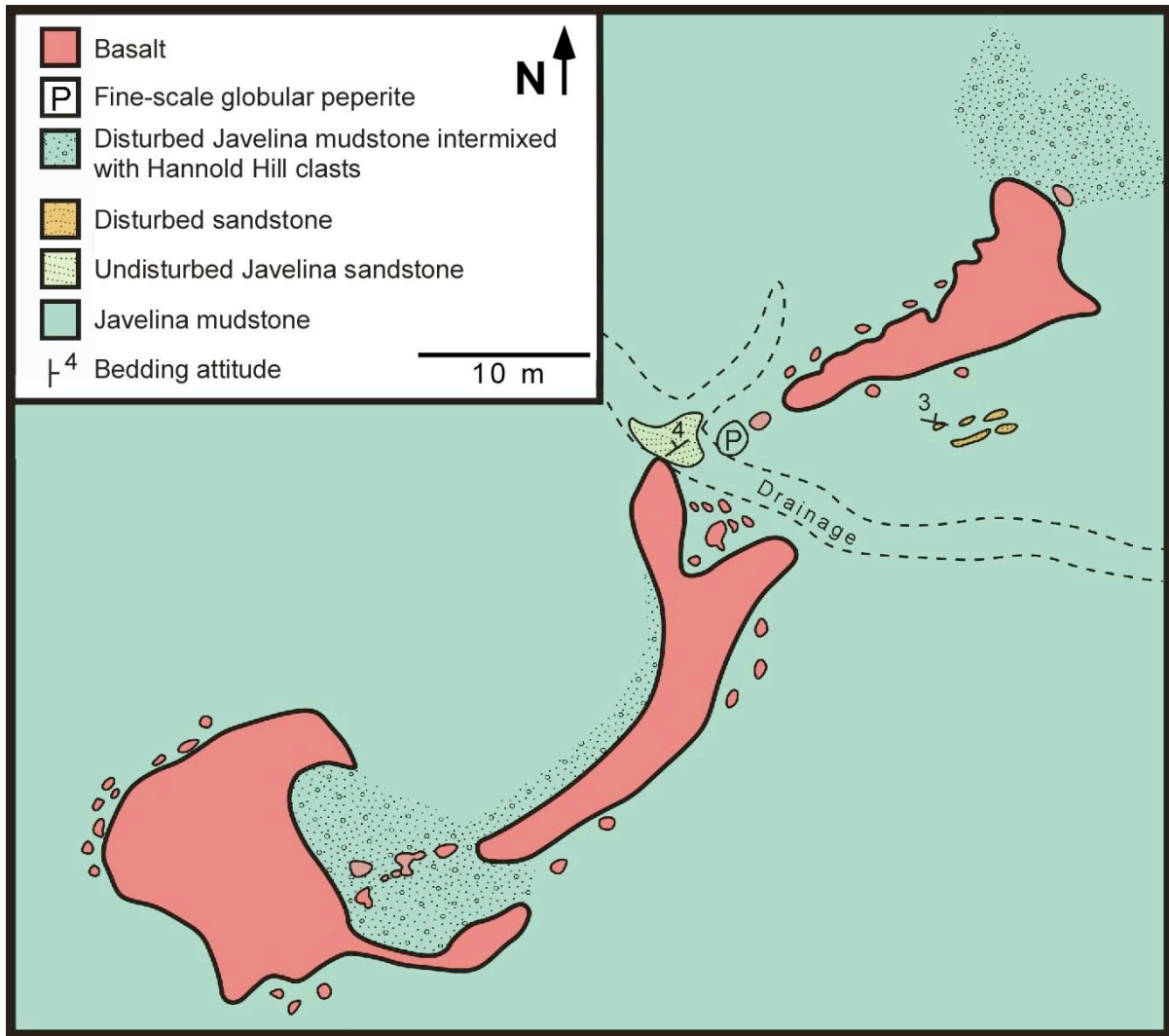


Figure 89: Tape-and-compass map of the inclined pillowed dike. Location shown in Figure 81. Intrusive pillows are shown to scale.

exposure; however, it is lithologically identical to the basalt in that intrusion. The dike is composed of intrusive pillows of basalt ≤ 3 m in diameter. Mudstone tendrils separate some pillows, whereas other pillows are in direct contact. Where exposure permits, the pillows can be seen to be connected in three dimensions. In one location (Figure 89), microglobular peperite occurs where thin tendrils of mudstone 5 mm to 10 cm thick extend between some of the smaller pillows. The dike terminates in an inclined, tabular, pillowed mass of basalt 60 m from the southwestern edge of the main intrusion. Microglobular peperite is visible along

some mudstone-basalt contacts. In other places, conglomeratic mudstone or ellipsoidal pods of discontinuous sandstone showing internal soft-sediment deformation occur near the intrusive contacts (Figure 89). The conglomeratic mudstone is poorly exposed but contains clasts inferred to be derived from the Hannold Hill Formation.

An isolated irregularly shaped intrusive mass of basalt occurs ~120 m to the southwest of the main intrusion (Figures 81 and 90). It is similar in lithology and phenocryst content to the basalt in the main intrusive body and occurs along the projected strike of the inclined pillow dike. Small intrusive pillows ~1 m in diameter occur along the margins of the intrusive mass. In addition, a body of disturbed, thinly bedded sandstone ~2 m² in area crops out at the southern margin of the intrusion and has subvertical contacts with the adjacent host mudstone.

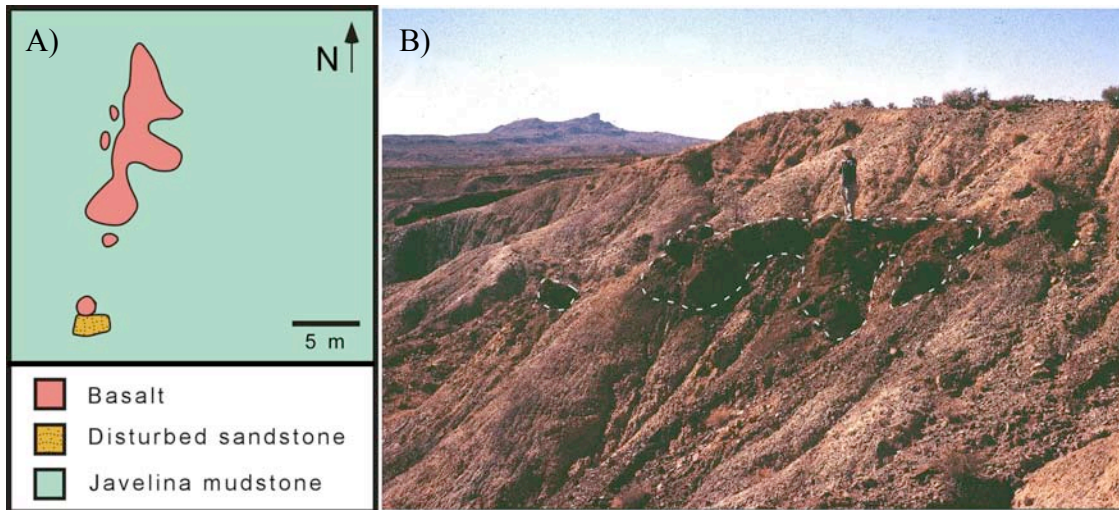


Figure 90: A) Tape-and-compass map of the irregularly shaped intrusive mass. Location shown in Figure 81. B) Photograph of intrusion (outlined) with author for scale. View looking toward the west.

A sample of basalt from the main basalt within the diatreme root zone (Figure 82) was collected for U–Pb SHRIMP-RG geochronological analyses (location shown in Figure 82), which was carried out by W.R. Griffen. The sample produced four zircon grains that

yielded ages from Late Cretaceous to Proterozoic (Figure 91 and Table 6). The youngest analysis is slightly discordant (Figure 92) and yields an age of 73.7 ± 3.1 Ma, which is within error of the U–Pb zircon age for the Cretaceous phreatomagmatic deposits on the Pitcock Ranch described by Breyer et al. (2005, and in review). However, a Cretaceous age for the diatreme root zone is contradicted by the presence of Eocene Hannold Hill conglomerate in that body. Therefore, even the youngest zircon grain within the sample is inferred to be a xenocryst derived from underlying strata. This example illustrates the need for caution when interpreting the U–Pb zircon geochronological results for basaltic rocks from this area.

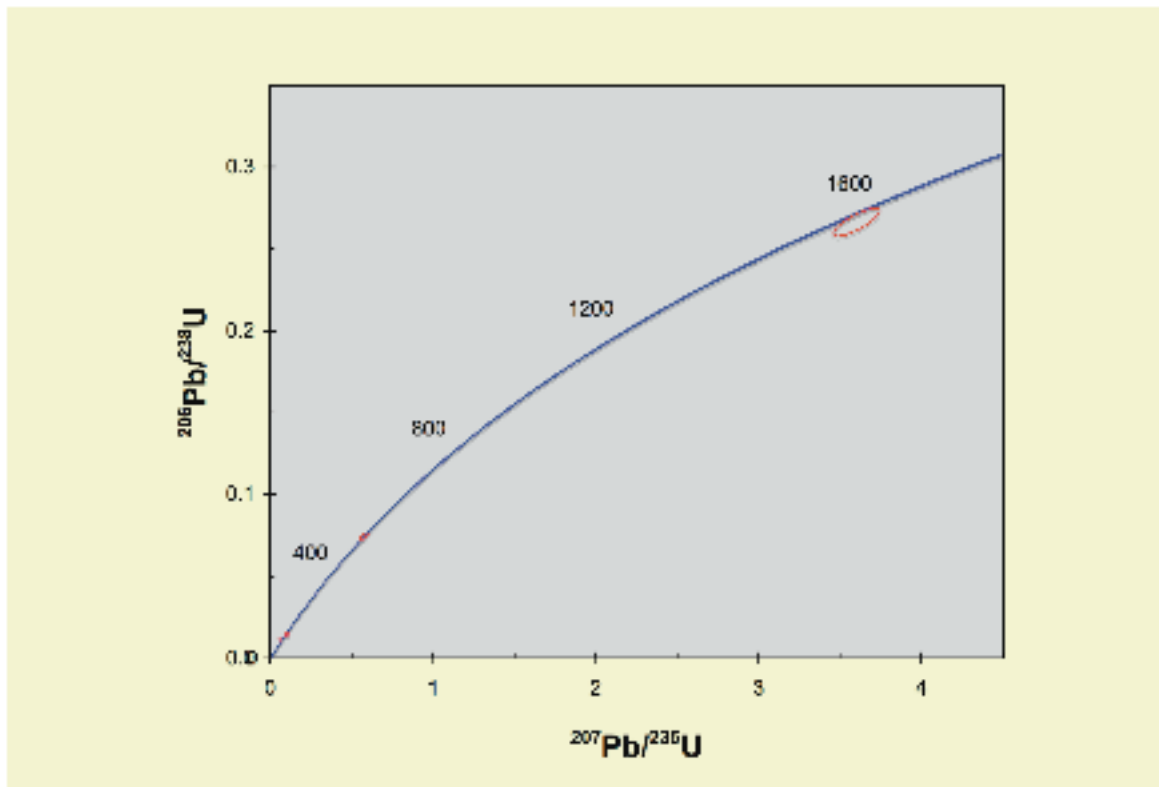


Figure 91: Concordia diagram for the sample taken from basalt within the main diatreme root zone. Analyses of individual spots on zircon grains are depicted as 2σ error ellipses.

Table 6: Analytical and calculated data from SHRIMP-RG analyses of zircon grains extracted from basalt at the main diatreme root zone on the Pitcock Ranch.

Grain No.	Comm. ^{206}Pb (%)	U (ppm)	Th (ppm)	$^{232}\text{Th}/^{238}\text{U}$	^{207}Pb -corrected		^{204}Pb -corrected		Total $^{238}\text{U}/^{206}\text{Pb}$	%	Total $^{207}\text{Pb}/^{206}\text{Pb}$	%	^{204}Pb -corrected				Error corr. coeff. *		
					$^{206}\text{Pb}/^{238}\text{U}$ age (Ma)	1 σ error (Ma)	$^{207}\text{Pb}/^{206}\text{Pb}$ age (Ma)	1 σ error (Ma)					$^{238}\text{U}/^{206}\text{Pb}$	error	$^{207}\text{Pb}/^{206}\text{Pb}$	error		$^{207}\text{Pb}/^{235}\text{U}$	error
P2-1	0.04	113	90	0.82	1526.6	20.3	1531.2	18.6	3.73	1.4	.0981	0.9	3.73	1.4	.0978	1.0	3.61	1.7	.816
P2-2	0.00	92	33	0.37	93.0	2.1	92.7	2.1	69.05	2.3	.0445	6.3	69.05	2.3	.0445	6.3	0.09	6.7	.335
P2-3	0.11	525	753	1.48	464.5	5.4	464.3	5.3	13.38	1.2	.0568	1.1	13.39	1.2	.0559	1.3	0.58	1.8	.668
P2-4	0.91	796	475	0.62	74.9	1.0	74.2	1.0	85.57	1.3	.0473	2.3	86.36	1.3	.0392	7.8	0.06	7.9	.170

*Error correlation coefficient between $^{207}\text{Pb}/^{235}\text{U}$ and $^{206}\text{Pb}/^{238}\text{U}$.

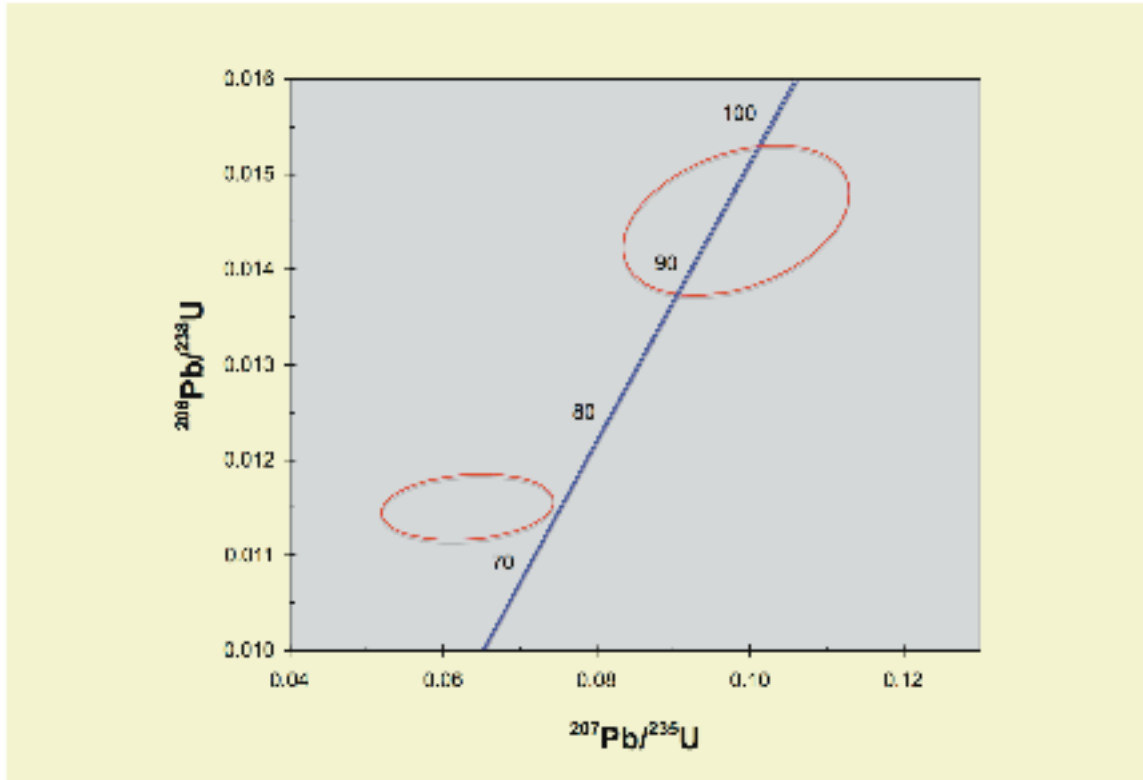


Figure 92: Concordia diagram for the two analyses yielding the youngest ages for the sample taken from basalt within the main diatreme root zone. Analyses of individual spots on zircon grains are depicted as 2σ error ellipses.

Interpretation. The main intrusive body is inferred to represent the erosional remnants of a diatreme root zone related to a maar (Figure 93). Based on age constraints discussed previously, this maar is interpreted to have formed at ~40 Ma when basaltic magma, related to the Christmas Mountains intrusive complex, intruded groundwater-rich sediment in the Hannold Hill Formation or overlying strata, initiating a phreatomagmatic eruption. The eruption propagated downward as explosions quarried into the poorly consolidated country rock. The deepening crater filled with phreatomagmatic slurry composed of disrupted sediment, fragmented basalt, and released groundwater (cf., White, 1991). During the eruption, strata near the crater walls, including the Hannold Hill conglomerate, slumped progressively deeper into the vent. Farther east, where the Hannold

Hill Formation is exposed in the Tornillo basin, it occurs > 225 m above the top of the Javelina Formation (Lehman, 1986). Therefore, the Hannold Hill conglomerate in the root zone must have subsided a comparable distance. The presence of Hannold Hill conglomerate in the diatreme root zone indicates volcanism occurred after, or possibly during, deposition of the Hannold Hill Formation.

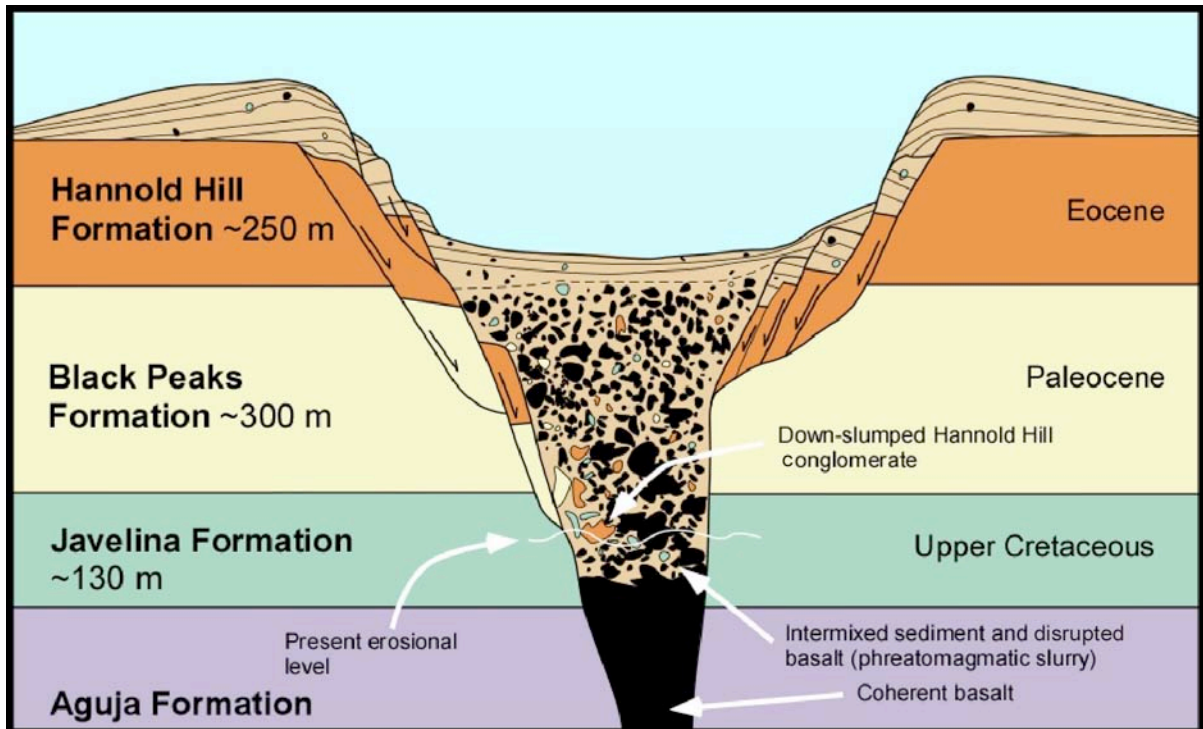


Figure 93: Model for the formation of the main diatreme root zone. Generalized thickness of units from Lehman (1985).

Masses of basalt intruded the diatreme root zone following the final stages of explosive volcanism after most of the groundwater had been consumed. During this period of non-explosive intrusion, fluidal bodies of basalt magma penetrating the surrounding poorly consolidated mudstone formed intrusive pillows along the northern side of the intrusion. In addition, the inclined pillowed dike extending to the southwest from the main intrusion is inferred to represent a blind apophysis from the main intrusive body, which was injected

laterally into the Javelina Formation (cf., White and McClintock, 2001). Disrupted sandstone masses and abundant clasts of Hannold Hill conglomerate mixed with mudstone along the intrusive contacts of both the dike and main intrusion suggest that the surrounding Javelina Formation and down-slumped Hannold Hill conglomerate became fluidized by heating of pore fluids during magma intrusion. Some fluidized Javelina mudstone was injected into the margins of the intrusions and formed fine-grained clastic tendrils cutting the basalt.

Abundant peperite formed by non-explosive magma-sediment interaction during this stage as well, including microglobular peperite present along the margins of the intrusion against the Javelina Formation. Busby and White (1987) interpreted microglobular peperite as arrested fuel-coolant interaction. Following this interpretation, microglobular peperite in the diatreme root zone records incipient stages in phreatomagmatic activity that did not result in explosions because of lack of sufficient groundwater during a late phase in the development of the diatreme root zone. Masses of dispersed to closely packed peperite within the root zone (e.g., Figure 85) record magma-sediment interaction between passively upwelling basalt magma and unconsolidated, intravent phreatomagmatic slurry. Fluidized portions of the phreatomagmatic slurry propagated through contraction cracks in the cooling magma, forming numerous clastic tendrils within basalt. The large clastic dike and subsidiary clastic dikes extending from it represent the last stages of activity in the intrusion. These dikes are inferred to have formed from upward injection of fluidized phreatomagmatic slurry from deeper levels of magma-sediment interaction (cf., Leat and Thompson, 1988).

Western diatreme root zone

An area of disturbed Javelina Formation ~60 m in diameter is located ~250 m southwest of the main diatreme root zone (Figure 81). This second diatreme root zone is centered on a small hill composed of disturbed Javelina mudstone and sandstone, intrusive basalt, and conglomerate (Figures 94 and 95). The basalt crops out as three closely spaced mounds separated by homogenous mudstone and forms an erosion-resistant unit that supports the hill. Each of the larger basaltic masses is composed of numerous ovoid pillows typically 1–3 m in diameter. Tendrils of white mudstone 15–40 cm thick separate many of the pillows, whereas other pillows are in direct contact. Small intrusive pillows < 1 m diameter are also dispersed in the mudstone between the mounds.

The three main masses of basalt are in contact with silty conglomerate containing well-rounded cobbles of limestone, chert, and sandstone. Subangular blocks of massive and cross-bedded sandstone up to 50 cm across also occur as clasts in the conglomerate. Basalt intrudes the conglomerate as ovoid tongues down to 3 cm in diameter that likely connect in three dimensions, forming domains of conglomerate-hosted peperite (Figure 96). Angular basaltic clasts formed by quench fragmentation occur in the conglomerate near these basalt/conglomerate contacts. In one well-exposed location in the eastern basalt mass, conglomerate intrudes the basalt along a contraction crack several centimeters wide. Sparse, angular to subangular basaltic clasts 2–5 cm across are intermixed with the matrix of the conglomerate filling the crack. A clast count on the conglomerate near the northern mound shows that the conglomerate is similar to that within the main diatreme to the northeast (Table 5). As in that diatreme, the conglomerate is inferred to have been derived from the

Hannold Hill Formation. The conglomerate has discordant, subvertical contacts with the disturbed zone of Javelina Formation (Figure 95).

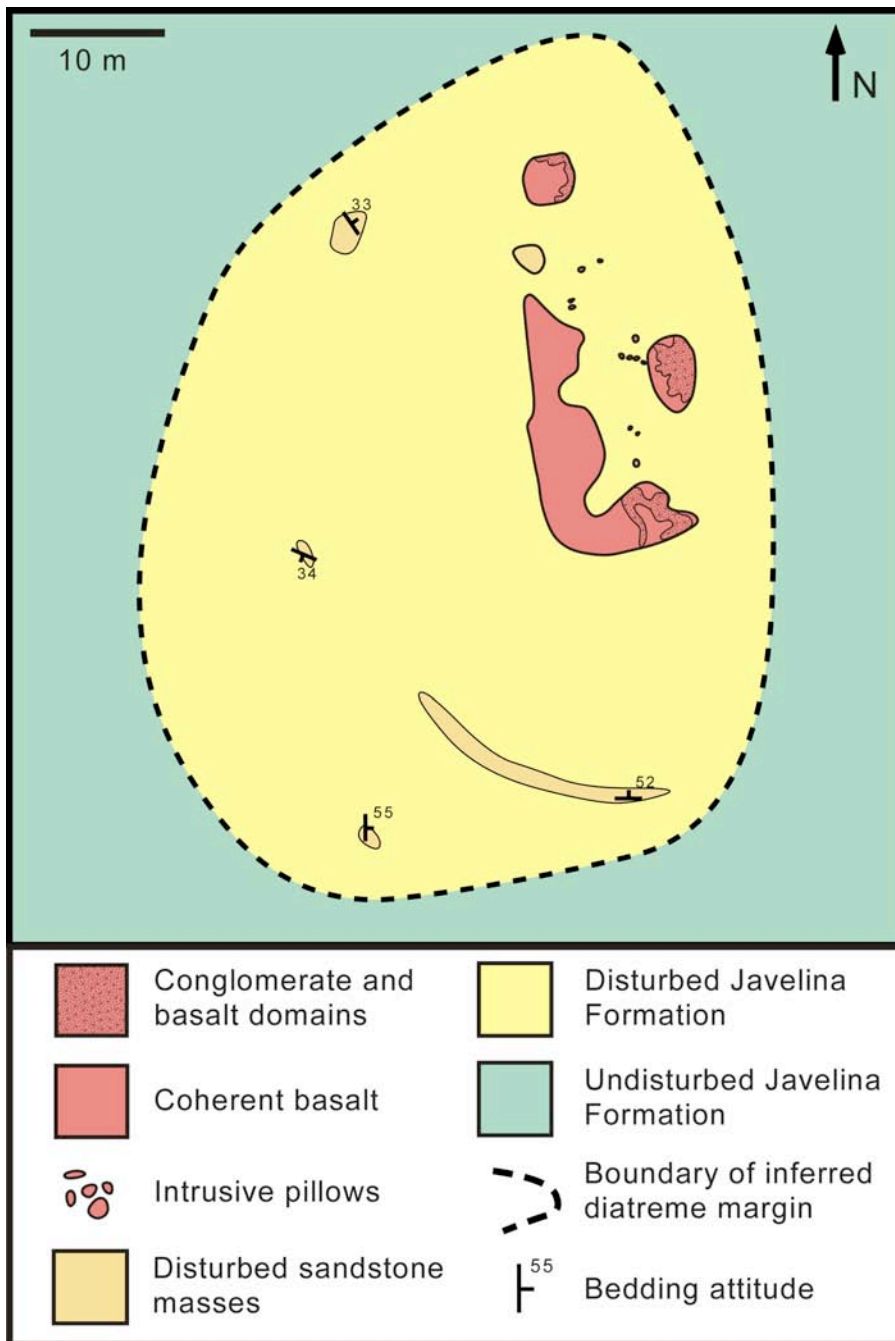


Figure 94: Sketch map of the western diatreme root zone. Bedding attitudes are located correctly; however, disturbed sandstone masses are shown schematically. Location shown in Figure 81.

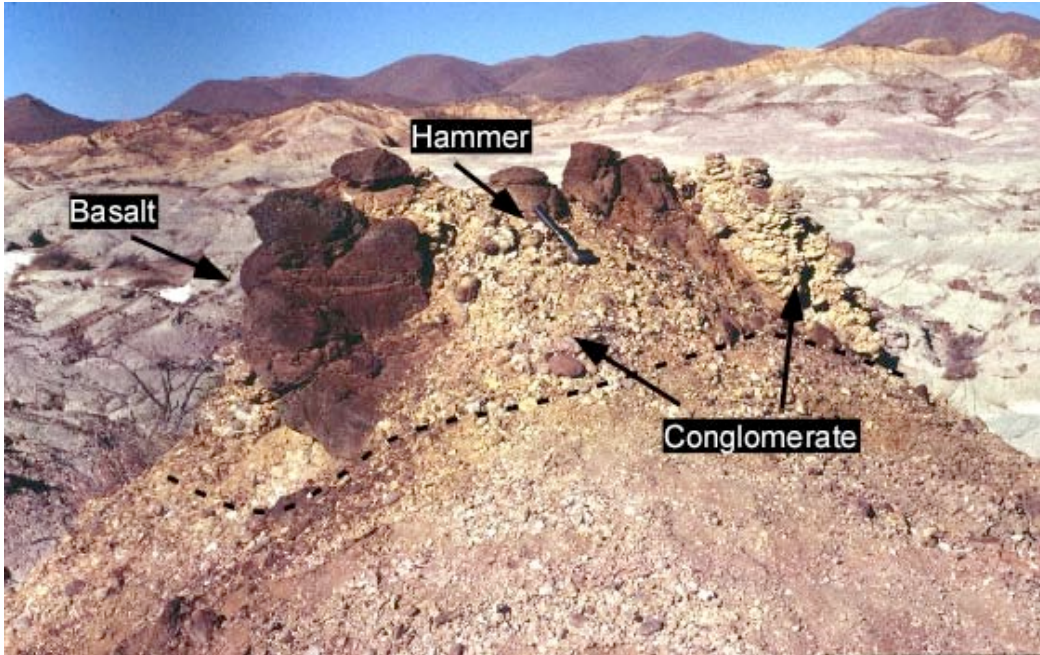


Figure 95: Northernmost mass of basalt in contact with conglomerate in the western diatreme root zone. The dashed line approximates the subvertical contact between conglomerate and disturbed Javelina mudstone. Undisturbed Javelina mudstone is visible in the background.



Figure 96: Conglomerate-hosted peperite formed between basalt and down-slumped Hannold Hill conglomerate.

The area surrounding the intrusion is predominantly composed of color-banded Javelina mudstones. Disrupted mudstones within the disturbed zone do not show well-defined horizontal bands of color typical of the Javelina Formation elsewhere and instead tend to show randomly arranged color variations on the scale of several meters. However, the margin of the disturbed zone is difficult to trace based solely on this criterion and was primarily delineated by mapping disrupted sandstones in the area (Figure 97). Outside of the disturbed zone, typical Javelina channel sandstones are cross-bedded and have very shallow dips. Sandstones within the disturbed zone are dispersed, detached masses ≤ 4 m across that have variable dips, rounded to irregular margins, and convolute to disrupted internal bedding indicative of soft-sediment deformation. In some disturbed sandstone masses, the convolute bedding is parallel to the irregular margin of the mass. Some disturbed sandstone masses contain channel-lag conglomerate composed of paleocaliche pebbles ≤ 1 cm in diameter, which is commonly found in the Javelina Formation. Many discrete sandstone masses are aligned along similar trends that are roughly concentric around the central intrusive area; these aligned masses may represent individual disrupted beds. In the southern portion of the diatreme root zone, a continuous sandstone lens 1.5 m thick partly wraps around the basalt intrusion. One portion of the southern boundary of the disturbed zone is marked by a sharp fault separating normal sandstone and disturbed, steeply dipping sandstone.

Poorly exposed dike-like stringers up to 10 m long consisting of limestone and chert cobbles similar to those in Hannold Hill conglomerate appear in disrupted mudstone within the disturbed zone in some locations. The appearance of these cobbles defines the margin of the disturbed zone within homogenous mudstone where disrupted and faulted sandstone masses are not present.

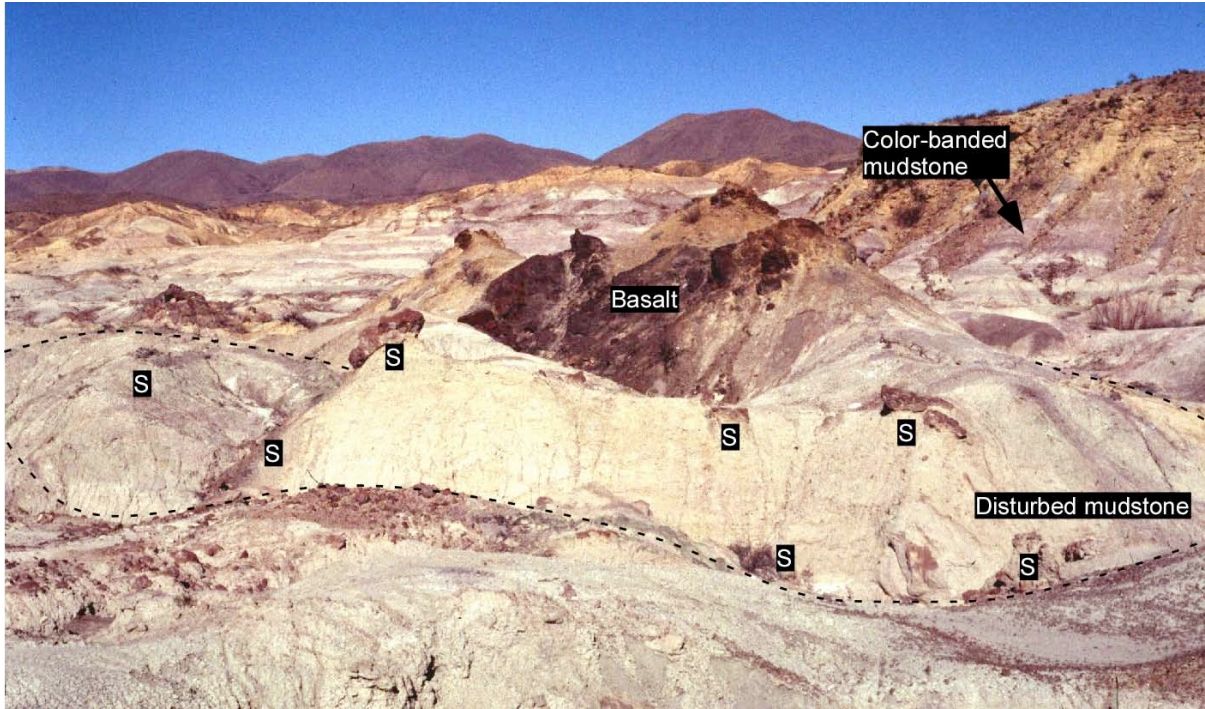


Figure 97: Outcrop view of the western diatreme root zone looking north. Dotted line represents approximate contact between disturbed and undisturbed Javelina Formation. Width of view is ~150 m. S = detached sandstone masses.

Interpretation. The disturbed zone is inferred to represent the diatreme root zone of a second maar volcano. Although this root zone occurs at the same stratigraphic level as the main diatreme root zone discussed earlier, the root zone is different because it is primarily composed of disturbed Javelina Formation with only a small volume of basalt. The two diatreme root zones in this area, the inclined pillowed dike extending from the main diatreme, and the isolated intrusive mass are aligned along a southwest-northeast trend (Figure 81), suggesting a control by pre-existing structures in the basement or by residual Laramide compressional stress during the Eocene (cf., Henry et al., 1991).

Eastern diatreme root zone

The largest intrusion in the study area forms a semicircular discordant mass ~250 m across that is composed of diabase and intrudes the Black Peaks Formation in Big Bend National Park (Figure 50). Maxwell et al. (1967) mapped the intrusion as two dike-like masses. During the present study, the intrusion was only examined briefly; however, interesting styles of magma-sediment interaction indicate the intrusion may represent a third diatreme root zone. Except for being coarser grained, the diabase is petrographically identical to the analcite-bearing basalt found in the other diatreme root zones (Figure 75).

A large raft (25 x 20 m across and 5 m thick) of trough cross-bedded sandstone lies within the intrusion and typically dips at ~50–70° into its center (Figure 98). Channel-lag deposits within the sandstone raft contain pebbles of red and black chert, and do not resemble Hannold Hill conglomerate. The intrusive contacts surrounding the raft are covered by scree, but they can be located within a few meters. No clastic dikes extend from the raft, and the sandstone is internally undeformed. Despite this, the diabase intrusion displays several types of magma-sediment interaction.

Along the margins of the intrusion, tendrils composed of silt and mud up to 20 cm thick propagate into the diabase along contraction cracks. Some of these sediment-filled cracks form well-developed triple junctions (Figure 99). Some cracks contain small domains of peperite 5–10 cm across. Petrographic examination of the domains of peperite indicates they are composed of sparse, angular diabase clasts set within a mud-rich matrix containing silt- to sand-sized grains of quartz, chert, and feldspar. In thin section, contacts between sediment tendrils and diabase appear sharp and jagged. Thus, these domains of peperite are

inferred to record small-scale magma-sediment interaction involving brittle failure of chilled diabase.



Figure 98: Raft of trough cross-bedded sandstone within the eastern diatreme root zone. View is looking toward the north.

Clastic tendrils between 1 mm and 50 cm thick also invade the diabase in the southern portions of the intrusion. These tendrils are different from the sediment tendrils along the margins of the intrusion because they are composed of a medium- to coarse-grained sandy matrix with dispersed angular to subangular basalt clasts ~1 cm across and pebble-sized quartz and chert clasts. In places, the tendrils follow regular contraction cracks but in general they extend randomly throughout the diabase away from a zone of closely packed peperite composed of rounded to angular, chaotically arranged diabase clasts ≤ 2 m in diameter that are intermixed with the sandy matrix (Figure 100). Jigsaw texture occurs in places. The sedimentary component in the peperite is not similar to local Black Peaks mudstones.

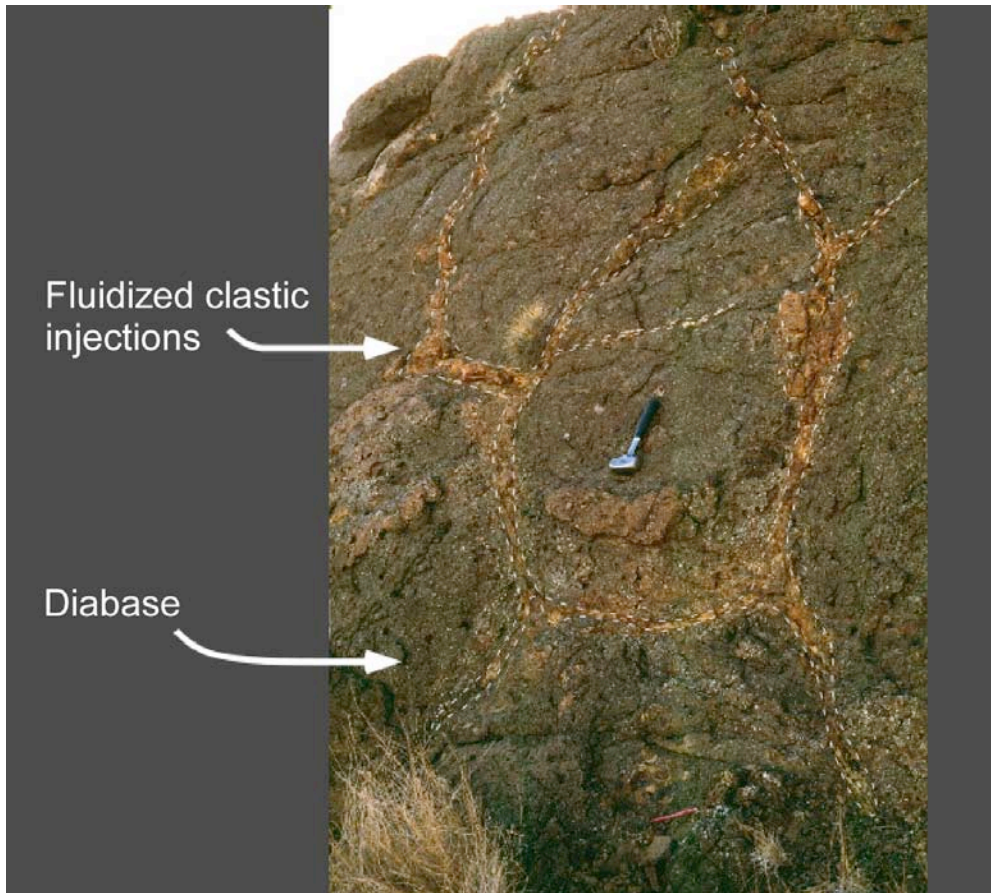


Figure 99: Sediment-filled contraction cracks (outlined) forming well-developed triple junctions.

Interpretation. The Black Peaks Formation was wet and unconsolidated at the time of the intrusion. The formation of thermal contraction cracks in the diabase resulted in a significant release in pressure that allowed fluidized sediment to inject for meters into the cooling intrusion. Similar sediment-filled contraction cracks, created by fluidization of wet sediment in contact with magma, are discussed by Kokelaar (1982).

The sedimentary component of the closely packed peperite in the southern portions of the intrusion is interpreted to represent phreatomagmatic slurry composed of disaggregated, down-slumped country rock mixed with shattered basalt and water. Sediment-filled tendrils and closely packed peperite in the intrusion are similar to features described in the main

diatreme root zone in the western portion of the study area. For these reasons, the intrusion is inferred to be another diatreme root zone, in this case occurring at a shallower stratigraphic level in the Black Peaks Formation.

The steeply dipping sandstone raft is inferred to represent a coherent, slumped block of sandstone from an overlying unit and is most likely derived from higher parts of the Black Peaks Formation. Rafts of this type have been documented in upper portions of other diatreme root zones (White and McClintock, 2001; Ross and White, 2006).

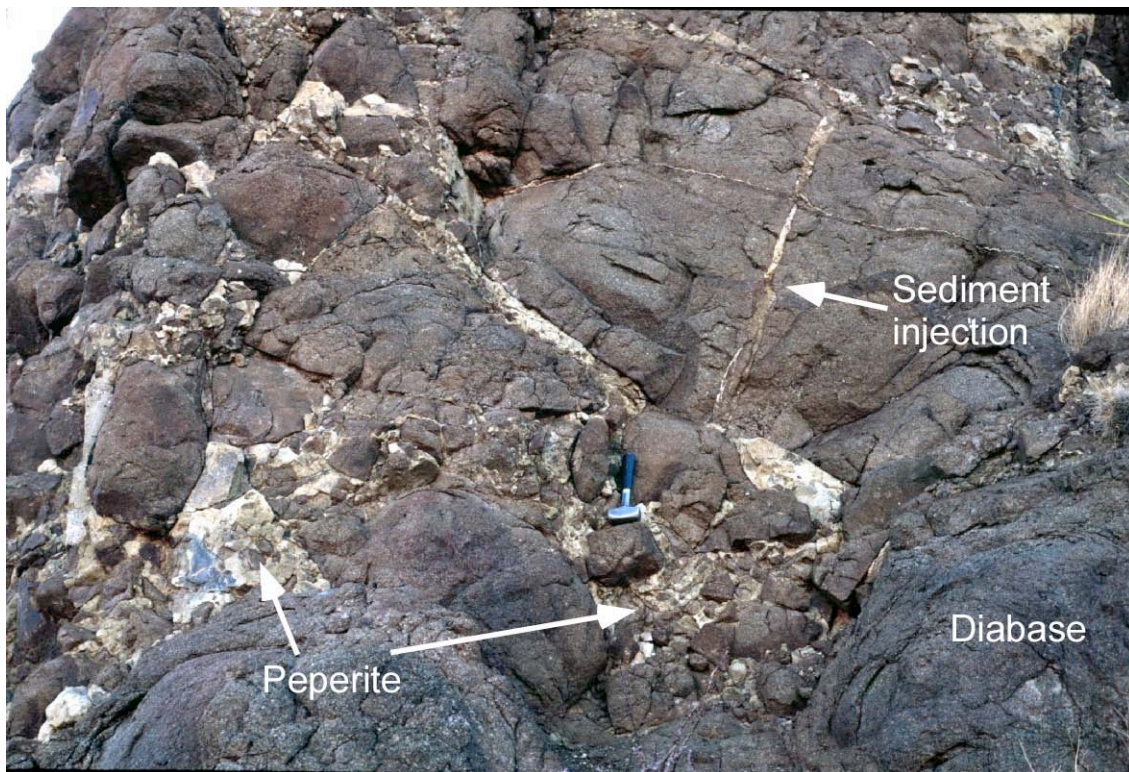


Figure 100: Closely packed peperite consisting of diabase and light-colored sedimentary material.

Chapter 5: Conclusions

This study investigates two separate volcanological problems in the Big Bend area of West Texas. The first aspect of this research concerns Upper Cretaceous pyroclastic deposits at Peña Mountain in Big Bend National Park. The second focus of this research is the physical volcanology of Eocene diatreme root zones and associated intrusions on the Pitcock Ranch and Big Bend National Park.

Dr. Thomas Lehman discovered the Upper Cretaceous pyroclastic deposits at Peña Mountain but did not describe them in detail. As a result of the present study, the pyroclastic deposits are interpreted to be the erosional remnants of at least two maars. Deposits on the northern side of Peña Mountain form upper and lower pyroclastic sequences separated by a sharp truncation surface. In places, a calcareous siltstone and mudstone unit that contains a lacustrine fossil assemblage and represents a period of eruptive quiescence overlies the truncation surface. Both the upper and lower pyroclastic sequences on the northern side of Peña Mountain consist of numerous beds ~30 cm thick on average that are composed of tuff, lapilli tuff, and grain-supported lapillistone and are interpreted to have been deposited by air-fall and base-surge processes.

Pyroclastic strata on the southern side of Peña Mountain are also composed of similar deposits, in addition to thick, massive layers rich in blocks and bombs. The pyroclastic strata on the southern side of Peña Mountain preserve a crater margin defined by highly disturbed pyroclastic beds and nonvolcanic Aguja strata, which rim less disturbed pyroclastic deposits. The highly disturbed strata are inferred to have slumped into the vent as it progressively deepened and widened during the eruption. Less disturbed strata were not as strongly affected by these processes. The lower pyroclastic sequence on the northern side of Peña

Mountain is inferred to correlate with the pyroclastic strata on the southern side of the mountain, whereas the upper pyroclastic sequence on the northern side of the mountain is interpreted to represent the construction of a second, nearby maar following a period of quiescence.

The pyroclastic strata on Peña Mountain show features typical of wet phreatomagmatic eruptions, such as armored lapilli, uncarbonized wood fragments, and abundant impact sags. These features indicate that the eruption columns contained water and that the beds were wet and cohesive during and after deposition. Juvenile basaltic ash and lapilli in the deposits are intermixed with a significant amount (up to 70%) of accidental, sand-sized quartz, feldspar, and lithic grains. Some lapilli have globular shapes and were ejected as fluid droplets of magma. Angular quench-fragmented shards also occur. Basaltic pyroclasts are poorly to moderately vesicular and contain abundant basaltic glass altered to smectite. Quartz xenocrysts are common and record fine-scale magma-sediment interaction before eruption. Lithic blocks of sandstone containing abundant oyster fossils were derived from the Rattlesnake Mountain Sandstone Member of the Aguja Formation, indicating that the eruptions excavated to depths of at least 150 m below the surface. All these features point to generation of the tephra from subsurface phreatomagmatic explosions driven by uprise of basalt magma into wet, unlithified sediments.

The pyroclastic deposits at Peña Mountain intertongue with the upper shale member of the Aguja Formation, constraining the volcanism to have occurred during the Campanian. Furthermore, U–Pb isotopic dating of zircon grains extracted from basalt bombs in the pyroclastic strata yields an age of 76.6 ± 1.3 Ma, which is consistent with other age constraints on the upper shale member. If the U–Pb zircon age is taken to represent the

crystallization age of the basalt, then the pyroclastic deposits at Peña Mountain are approximately equivalent in age to the phreatomagmatic pyroclastic strata on the Pitcock Ranch north of Big Bend National Park described by Busbey et al. (1998) and Breyer et al. (2005, and in review). Besides having a similar age, the pyroclastic deposits at Peña Mountain show a similar eruptive style to the pyroclastic deposits on the Pitcock Ranch and significantly increase the known extent of Cretaceous phreatomagmatic volcanism in the Big Bend area. The Peña Mountain basaltic rocks have different trace-element signatures from the Pitcock Ranch deposits, but this conclusion is based on very limited data. Extensive alteration shown by these rocks makes it difficult to determine their original magmatic affinities.

Breyer et al. (2005, and in review) inferred that the pyroclastic deposits on the Pitcock Ranch might represent a westward extension of the intraplate Balcones igneous province, which is present farther east in Texas. If this interpretation is correct, then the Peña Mountain maars are also a part of that province, although they appear to be geochemically unlike the strongly alkaline rocks in the Balcones igneous province (cf., Barker et al., 1987; Wittke and Mack, 1993).

The second major part of this study focused on Tertiary intrusions on the Pitcock Ranch north of Big Bend National Park. These intrusions cut through and interact with strata of the Cretaceous Javelina Formation and Paleogene Black Peaks and Hannold Hill Formations, forming an array of features resulting from magma-sediment interaction. The intrusions correlate with the Christmas Mountain intrusive complex to the west (Henry et al., 1989), indicating an Eocene age.

Dikes in the southeastern portion of the Pitcock Ranch intruded unconsolidated Black Peaks mudstones. Billows separated by cusate invaginations, intrusive pillows, and peperite occur along the margins of the intrusions. Some of the dikes have all three of these features developed along their margins in a restricted area, suggesting that they record progressive stages of magma-sediment interaction. Billows separated by cusate invaginations are interpreted to represent the initial stage of interaction between magma and wet, unconsolidated host sediment. As individual billows become more bulbous and separate from the main intrusive body, they grade into intrusive pillows. Intrusive pillows in turn grade into areas of peperite, which record a more intimate stage of magma-sediment interaction. Small-scale blocky peperite formed by quench fragmentation of chilled margins of intrusions (and possibly by minor steam explosions). The long east-west-trending dike in the southwestern part of the study area developed similar billows against unconsolidated strata of the Javelina Formation. The Cottonwood Wash intrusion, which also cuts the Javelina Formation, locally developed fine-scale globular peperite along the intrusive contacts.

Three intrusions interpreted to be diatreme root zones crop out on the Pitcock Ranch and nearby land in Big Bend National Park and exhibit intrusive pillows and different types of peperite, as well as clastic dikes and related features. In two of the diatreme root zones, domains of conglomerate-hosted peperite occur where magma intruded and mixed with masses of down-slumped Hannold Hill conglomerate. The presence of down-slumped Hannold Hill strata in those two diatreme root zones requires that the volcanoes fed by these root zones erupted after, or possibly during, deposition of the Eocene Hannold Hill Formation. Four zircon grains were extracted from a sample of basalt from the main diatreme

root zone. The youngest analysis yielded a slightly discordant U–Pb SHRIMP-RG age of 73.7 ± 3.1 Ma, but this age is inferred to date a xenocryst derived from underlying strata.

Samples from the dikes on the Pitcock Ranch, from the Cottonwood Wash intrusion, and from basalts in the diatreme root zones show similar chondrite-normalized REE patterns, as well as comparable patterns on normalized multi-element diagrams. All of these intrusions plot in similar fields in trace-element discrimination diagrams, and although they are not tightly clustered, the samples show transitional to alkaline, within-plate signatures.

Barker (2004) briefly noted the presence of peperite developed between basalt and strata in the Chisos Group, but the present study provides the first detailed documentation of progressive stages of interaction between mafic magma and unconsolidated, wet sediment in the Big Bend region. In addition, the variety of features associated with the intrusions discussed in this study offers insights into processes that may lead to the initiation of phreatomagmatic explosions in the subsurface. Detailed mapping in a small area along the southern flank of the Rosillos Mountains laccolith found the first evidence for phreatomagmatic diatreme root zones in the Tertiary Trans-Pecos magmatic province. This work suggests that at one time there may have been a number of small phreatomagmatic volcanoes in the region. More diatreme root zones probably remain to be discovered, and the Big Bend area could become an important locale for the study of ancient phreatomagmatic volcanoes and associated features created by magma-sediment interaction.

Finally, the current study describes peperite formed in the Eocene along intrusive contacts between basaltic magma and unconsolidated strata as old as the Upper Cretaceous Javelina Formation. This observation is of general importance because it negates a common

assumption in the literature that peperite records penecontemporaneous sedimentation and intrusive activity (e.g., Skilling et al., 2002).

References

- Barker, D.S., 1977, Northern Trans-Pecos magmatic province; introduction and comparison with the Kenya Rift: *Geological Society of America Bulletin*, v. 88, p. 1421-1427.
- Barker, D.S., 2004, Sedimentation, volcanism and intrusion in the lower Chisos Group, Big Bend National Park, Texas: *Geological Society of America Abstracts with Programs*, v. 36, p. 128-129.
- Barker, D.S., Mitchell, R.H., and McKay, D. 1987, Late Cretaceous nephelinite to phonolite magmatism in the Balcones province, Texas, *in* Morris, E.M., and Pasteris, J.D., eds., *Mantle metasomatism and Alkaline Volcanism*: Boulder, Colorado, Geological Society of America Special Paper 215, p. 293-304.
- Barnes, V.E., 1979, Geologic atlas of Texas, Emory Peak–Presidio Sheet: The University of Texas at Austin, Bureau of Economic Geology.
- Befus, K., Hanson, R., Lehman, T., and Breyer, J., 2006a, Late Cretaceous phreatomagmatic volcanism at Peña Mountain, Big Bend National Park, Texas: *Geological Society of America Abstracts with Programs*, v. 38, p. 30.
- Befus, K.S., Hanson, R.E., Breyer, J., Busbey, A., 2006b, Paleogene basaltic peperites developed in Cretaceous to Paleogene strata in the Big Bend area of West Texas: *Geological Society of America Abstracts with Programs*, v. 38, p. 35.
- Black, L.P., Kamo, S.L., Allen, C.M., Davis, D.W., Aleinikoff, J.W., Valley, J.W., Mundil, R., Campbell, I.H., Korsch, R.J., Williams, I.S., and Foudoulis, C., 2004, U–Pb microprobe geochronology by the monitoring of a trace-element-related matrix effect; SHRIMP, ID-TIMS, ELA-ICP-MS and oxygen isotope documentation for a series of zircon standards: *Chemical Geology*, v. 205, p. 115-140.
- Breyer, J.A., Busbey, A.B., Hanson, R.E., Griffen, W.R., Hargrove, U.S., and Bergman, S.C., 2005, New evidence for Late Cretaceous volcanic activity in Trans-Pecos Texas: *Geological Society of America Abstracts with Programs*, v. 37, p. 11.
- Breyer, J.A., Busbey, A.B., Hanson, R.E., Griffen, W.R., Hargrove, U.S., Bergman, S.C., and Befus, K.S., Evidence for Late Cretaceous volcanism in Trans-Pecos Texas: *Journal of Geology*, in review.
- Busbey, A.B., Breyer, J.A., and Hanson, R.E., 1998, Late Cretaceous volcanic activity in the Trans-Pecos magmatic province, Texas: *Geological Society of America Abstracts with Programs*, v. 30, p. A178.
- Busby-Spera, C.J., and White, J.D.L., 1987, Variation in peperite textures associated with differing host-sediment properties: *Bulletin of Volcanology*, v. 49, p. 765-775.

- Bryan, W.B., 1972, Morphology of quench crystals in submarine basalts: *Journal of Geophysical Research*, v. 77, p. 5812-5819.
- Carman, M.F., 1994, Mechanisms of differentiation in shallow mafic alkaline intrusions, as illustrated in the Big Bend area, western Texas: *Journal of Volcanology and Geothermal Research*, v. 61, p. 1-44.
- Cas, R.A.F., and Wright, J.V., 1987, *Volcanic Successions: Modern and Ancient*: Allen & Unwin, London, 528 p.
- Chough, S.K., and Sohn, Y.K., 1990, Depositional mechanics and sequences of base surges, Songaksan tuff ring, Cheju Island, Korea: *Sedimentology*, v. 37, p. 1115-1135.
- Collinsworth, B.D., and Rohr, D.M., 1986, An Eocene carbonate lacustrine deposit, Brewster County, West Texas, *in* Pause P.H., and Spears, R.G., eds., *Geology of the Big Bend Area and Solitario Dome, Texas*: West Texas Geological Society Guidebook, p. 117-124.
- Dadd, K.A., and Van Wagoner, N.A., 2002, Magma composition and viscosity as controls on peperite texture: an example from Passamaquoddy Bay, southeastern Canada: *Journal of Volcanology and Geothermal Research*, v. 114, p. 63-80.
- Dennie, D.P., 2001, *Geology of the Quaternary deposits along Cottownwood Wash, southern Rosillos Mountains, near Big Bend National Park, Texas*: Texas Christian University, M.S. thesis, 58 p.
- Gilmer, A.K., Kyle, J.R., Connelly, J.N., Mathur, R.D., and Henry, C.D., 2003, Extension of Laramide magmatism in southwestern North American into Trans-Pecos Texas: *Geology*, v. 31, p. 447-450.
- Gradstein, F., Ogg, J.G., and Smith, A.G., eds., 2004, *A Geologic Time Scale 2004*: Cambridge University Press, London, 589 p.
- Hanson, R.E., and Elliot, D.H., 1996, Rift-related Jurassic basaltic phreatomagmatic volcanism in the central Transantarctic Mountains: precursory stage to flood-basalt effusion: *Bulletin of Volcanology*, v. 58, p. 327-347.
- Hanson, R.E., and Hargrove, U.S., 1999, Processes of magma/wet sediment interaction in a large-scale Jurassic andesitic peperite complex, northern Sierra Nevada, California: *Bulletin of Volcanology*, v. 60, p. 610-626.
- Hanson, R.E., and Wilson, T.J., 1993, Large-scale rhyolite peperites (Jurassic, southern Chile): *Journal of Volcanology and Geothermal Research*, v. 54, p. 247-264.

- Henry, C.D., and Davis, L.L., 1996, Tertiary volcanic, volcanoclastic, and intrusive rocks adjacent to the Solitario, *in* Henry, C.D., and Muehlberger, W.R., eds., *Geology of the Solitario Dome, Trans-Pecos Texas; Paleozoic, Mesozoic, and Cenozoic sedimentation, tectonism, and magmatism: Report of Investigations*, The University of Texas at Austin, Bureau of Economic Geology, v. 240, p. 81-105.
- Henry, C.D., McDowell, F.W., Price, J.G., and Smyth, R.C., 1986, *Compilation of potassium-argon ages of Tertiary igneous rocks, Trans-Pecos Texas: The University of Texas at Austin, Bureau of Economic Geology Geological Circular 86-2*, 34 p.
- Henry, C.D., Price, J.G., and Miser, D.E., 1989, *Geology and Tertiary igneous activity of the Hen Egg Mountain and Christmas Mountains Quadrangles, Big Bend region, Trans-Pecos Texas: The University of Texas at Austin, Bureau of Economic Geology Report of Investigations No. 183*, 105 p.
- Henry, C.D., Price, J.G., and James, E.W., 1991, Mid-Cenozoic stress evolution and magmatism in the Southern Cordillera, Texas and Mexico: Transition from continental arc to intraplate extension: *Journal of Geophysical Research*, v. 96, p. 13,545-13,560.
- Hooten, J.A., and Ort, M.H., 2002, Peperite as a record of early-stage phreatomagmatic fragmentation processes: an example from the Hopi Buttes volcanic field, Navajo Nation, Arizona, USA: *Journal of Volcanology and Geothermal Research*, v. 114, p. 95-106.
- Horton, R.P., 2006, *Geology and vertebrate paleontology of Cretaceous and Tertiary strata on the Pitcock Rosillos Mountain Ranch, Brewster County, Texas: Texas Christian University, M.S. thesis*, 56 p.
- Ireland, T.R., and Williams, I.S., 2003, Considerations in zircon geochronology by SIMS: *Reviews in Mineralogy and Geochemistry*, v. 53, p. 215-241.
- Kano, K., 1991, Miocene pillowed sills in the Shimane Peninsula, SW Japan: *Journal of Volcanology and Geothermal Research*, v. 48, p. 359-366.
- Kokelaar, B.P., 1982, Fluidization of wet sediments during the emplacement and cooling of various igneous bodies: *Journal of the Geologic Society of London*, v. 139, p. 21-33.
- Leat, P.T., and Thompson, R.N., 1988, Miocene hydrovolcanism in NW Colorado, USA, fueled by explosive mixing of basic magma and wet unconsolidated sediment: *Bulletin of Volcanology*, v. 50, p. 229-243.
- Le Bas, M.J., LeMaitre, R.W., Streckeisen, A., and Zanettin, B., 1986, A chemical classification of volcanic rocks based on the total alkali silica diagram: *Journal of Petrology*, v. 27, p. 745-750.

- Lehman, T.M., 1985, Stratigraphy, sedimentology, and paleontology of Upper Cretaceous (Campanian-Maastrichtian) sedimentary rocks in Trans-Pecos Texas: University of Texas at Austin, Ph.D. dissertation, 299 p.
- Lehman, T.M., 1986, Late Cretaceous sedimentation in Trans-Pecos Texas, *in* Pause P.H., and Spears, R.G., eds., *Geology of the Big Bend Area and Solitario Dome, Texas: West Texas Geological Society Guidebook*, p. 105-110.
- Lehman, T.M., 1988, Stratigraphy of the Cretaceous-Tertiary and Paleocene-Eocene transition rocks of Big Bend National Park, Texas: a discussion: *Journal of Geology*, v. 96, p. 627-631.
- Lehman, T.M., 1989, Upper Cretaceous (Maastrichtian) paleosols in Trans-Pecos Texas: *Geological Society of America Bulletin*, v. 101, p. 188-203.
- Lehman, T.M., 1990, Paleosols in the Cretaceous/Tertiary transition in the Big Bend region of Texas: *Geology*, v. 18, p. 362-364.
- Lehman, T.M., 1991, Sedimentation and tectonism in the Laramide Tornillo Basin of West Texas: *Sedimentary Geology*, v. 75, p. 9-28.
- Lehman, T.M., and Coulson, A.B., 2002, A juvenile specimen of the sauropod dinosaur *Alamosaurus sanjaunensis* from the Upper Cretaceous of Big Bend National Park, Texas: *Journal of Paleontology*, v. 76, p. 156-172.
- Lorenz, V., 1973, On the formation of maars: *Bulletin of Volcanology*, v. 35, p. 183-204.
- Lorenz, V., Zimanowski, B., and Buettner, R., 2002, On the formation of deep-seated subterranean peperite-like magma-sediment mixtures: *Journal of Volcanology and Geothermal Research*, v. 114, p. 107-118.
- Ludwig, K.R., 2000, *Isoplot/Ex 3.0: A geological toolkit for Microsoft Excel*: Berkeley Geochronology Center Special Publication 1.
- Ludwig, K.R., 2001, *2001 SQUID 1.02 Add-In for Excel™*: Berkeley Geochronology Center Special Publication 2.
- Maxwell, R.A., Lonsdale, J.T., Hazzard, R.T., and Wilson, J.A., 1967, *Geology of Big Bend National Park, Brewster County, Texas*: The University of Texas at Austin, Bureau of Economic Geology Publication 6711, 320 p.
- McDowell, F.W., Lehman, T.M., and Connelly, J.N., 2004, A U–Pb age for the Late Cretaceous *Alamosaurus* vertebrate fauna of West Texas: *Geological Society of America Abstracts with Programs*, v. 37, p. 6.

- Melson, W.G., and Thompson, G., 1973, Glassy abyssal basalts, Atlantic sea floor near Saint Paul's Rocks; petrography and composition of secondary clay minerals: *Geological Society of America Bulletin*, v. 84, p. 703-716.
- Meschede, M., 1986, A method of discriminating between different types of mid-ocean basalts and continental tholeiites with the Nb–Zr–Y diagram: *Chemical Geology*, v. 56, p. 207-218.
- Moore, J.G., 1975, Mechanisms of formation of pillow lava: *American Scientist*, v. 63, p. 269-277.
- Mullen, E.D., 1983, MnO/TiO₂/P₂O₅: A minor element discriminant for basaltic rocks of oceanic environments and its implications for petrogenesis: *Earth and Planetary Science Letters*, v. 62, p. 53-62.
- Murray, J.K., 1999, Geologic mapping of the southern flank of the Rosillos laccolith, Brewster County, Texas: Texas Christian University, M.S. thesis, 45 p.
- Ogg, J.G., Agterberg, F.P., and Gradstein, F.M. 2004. The Cretaceous Period, *in* Gradstein, F., Ogg, J.G., and Smith, A.G., eds., *A Geologic Time Scale 2004*: Cambridge University Press, London, p. 344-383.
- Pearce, J.A., 1982, The role of subcontinental lithosphere in magma genesis at destructive plate margins, *in* Hawksworth C.J., and Norry, M.J., eds., *Continental Basalts and Mantle Xenoliths*, p. 230-249.
- Pearce, J.A., 1996, A user's guide to basalt discrimination diagrams, *in* Bailes, A.H., Christiansen, E.H., Galley, A.G., Jenner, G.A., Keith, J.D., Kerrich, R., Lentz, D.R., Leshner, C.M., Lucas, S.B., Ludden, J.N., Pearce, J.A., Peloquin, S.A., Stern, R.A., Stone, W.E., Syme, E.C., Swinden, H.S., and Wyman, D.A., eds., *Trace element geochemistry of volcanic rocks; applications for massive sulphide exploration: Short Course Notes*, Geological Association of Canada, 12, p. 79-113.
- Pearce, J.A., and Cann, J.R., 1973, Tectonic setting of basic volcanic rocks determined using trace element analysis: *Earth and Planetary Science Letters*, v. 19, p. 290-300.
- Pearce, J.A., and Norry, M.L., 1979, Petrogenetic implications of Ti, Zr, Y, and Nb variations in volcanic rocks: *Contributions to Mineralogy and Petrology*, v. 69, p. 33-47.
- Price, J.G., Henry, C.D., Parker, D.F., and Barker, D.S., eds., 1986, *Igneous Geology of Trans-Pecos Texas, Field Trip Guide and Research Articles*: The University of Texas at Austin, Bureau of Economic Geology, 360 p.
- Pollard, D.D., Muller, O.H., and Dockstader, D.R., 1975, The form and growth of fingered sheet intrusions: *Geological Society of America Bulletin*, v. 86, p. 351-363.

- Ross, P., and White, J.D.L., 2006, Debris jets in continental phreatomagmatic volcanoes: A field study of their subterranean deposits in the Coombs Hills vent complex, Antarctica: *Journal of Volcanology and Geothermal Research*, v. 149, p. 62-84.
- Roth, B., 1984, *Lysinoe* (Gastropoda: Pulmonata) and other land snails from Eocene-Oligocene of Trans-Pecos Texas, and their paleoclimatic significance: *The Veliger*, v. 27, p. 200-218.
- Runkel, A.C., 1990, Lateral and temporal changes in volcanogenic sedimentation; analysis of two Eocene sedimentary aprons, Big Bend Region, Texas: *Journal of Sedimentary Petrology*, v. 60, p. 747-760
- Schiebout, J.A., Rigsby, C.A., Rapp, S.D., and Hartnell, J.A., 1987, Stratigraphy of the Cretaceous-Tertiary Rocks of Big Bend National Park, Texas: *Journal of Geology*, v. 95, p. 359-371.
- Shervais, J.W., 1982, Ti-V plots and the petrogenesis of modern and ophiolitic lavas: *Earth and Planetary Science Letters*, v. 59, p. 101-118.
- Skilling, I.P., White, J.D.L., and McPhie, J., 2002, Peperite: a review of magma-sediment mingling: *Journal of Volcanology and Geothermal Research*, v. 114, p. 1-17.
- Sohn, Y.K., and Park, K.H., 2005, Composite tuff ring/cone complexes in Jeju Island, Korea: possible consequences of substrate collapse and vent migration: *Journal of Volcanology and Geothermal Research*, v. 141, p. 157-175.
- Stacey, J.S., and Kramers, J.D., 1975, Approximation of terrestrial lead isotope evolution by a two-stage model: *Earth and Planetary Science Letters*, v. 26, p. 207-221.
- Sun, S.S., and McDonough, W.F., 1989, Chemical and isotopic systematics of oceanic basalts; implications for mantle composition and process, *in* Saunders, A.D., and Norry M.J., eds., *Magmatism in the Ocean Basins*, Geological Society of London Special Publications, v. 42, p. 313-345.
- Tera, F., and Wasserburg, G.J., 1972, U-Th-Pb systematics in three Apollo 14 basalts and the problem of initial Pb in lunar rocks: *Earth and Planetary Science Letters*, v. 14, p. 281-304.
- Walker, G.P.L., 1992, Morphometric study of pillow-size spectrum among pillow lavas: *Bulletin of Volcanology*, v. 54, p. 459-474.
- Wheeler, E.A., and Lehman, T.M., 2005, Upper Cretaceous-Paleocene conifer woods from Big Bend National Park, Texas: *Palaeogeography, Palaeoclimatology, Palaeoecology*, v. 226, p. 233-258.

- White, J.D.L., 1991, Maar-diatreme phreatomagmatism at Hopi Buttes, Navajo Nation (Arizona), USA: *Bulletin of Volcanology*, v. 53, p. 239-258.
- White, J.D.L., 1996, Impure coolants and interaction dynamics of phreatomagmatic eruptions: *Journal of Volcanology and Geothermal Research*, v. 74, p. 155-170.
- White, J.D.L. and McClintock, M.K., 2001, Immense vent complex marks flood-basalt eruption in a wet failed rift: Coombs Hills, Antarctica: *Geology*, v. 29, p. 935-938.
- Winchester, J.A., and Floyd, P.A., 1976, Geochemical magma type discrimination; application to altered and metamorphosed basic igneous rocks: *Earth and Planetary Science Letters*, v. 28, p. 459-469.
- Winchester, J.A., and Floyd, P.A., 1977, Geochemical discrimination of different magma series and their differentiation products using immobile elements: *Chemical Geology*, v. 20, p. 325-343.
- Williams, I.S., 1997, U-Th-Pb geochronology by ion microprobe: not just ages but histories: *Society of Economic Geologists Reviews of Economic Geology*, v. 7, p. 1-35.
- Wilson, M., 1989, *Igneous Petrogenesis*: Chapman and Hall, Oxford, 466 p.
- Wittke, J.H., and Mack, L.E., 1993, OIB-like mantle source for continental alkaline rocks of the Balcones Igneous Province, Texas: Trace-element and isotopic evidence: *Journal of Geology*, v. 101, p. 333-344.
- Wood, D.A., 1980, The application of a Th–Hf–Ta diagram to problems of tectonomagmatic classification and to establishing the nature of crustal contamination of basaltic lavas of the British Tertiary volcanic province: *Earth and Planetary Science Letters*, v. 50, p. 11-30.
- Wohletz, K., 2002, Water/magma interaction: some theory and experiments on peperite formation: *Journal of Volcanology and Geothermal Research*, v. 114, p. 19-35.
- Wohletz, K.H., and Sheridan, M.F., 1983, Hydrovolcanic explosions II. Evolution of basaltic tuff rings and tuff cones: *American Journal of Science*, v. 283, p. 385-413.

Vita

Personal Background

Kenneth Befus
Fort Worth, Texas
Son of Richard and Pamela Befus
Married to Elizabeth Befus, March 13, 2004

Education

Diploma, Christiansen Academy, Rubio, Venezuela, 2000
Bachelor of Science, Texas Christian University, Geology, 2003

Experience

Teaching assistant at University of North Texas, 2004
Teaching assistant at Texas Christian University, 2005-2006

ABSTRACT

LATE CRETACEOUS AND EOCENE PHREATOMAGMATIC VOLCANISM AND MAGMA-SEDIMENT INTERACTION IN THE BIG BEND AREA OF WEST TEXAS

by Kenneth Befus, M.S., 2006
Department of Geology
Texas Christian University

Richard Hanson – Professor of Geology and Chair of the Department

John Breyer – Professor of Geology

Arthur Busbey – Associate Professor of Geology

This project examines two separate aspects of the volcanic evolution of the Big Bend area. Detailed mapping of phreatomagmatic, basaltic air-fall and base-surge deposits at Peña Mountain shows that they represent the erosional remnants of at least two maars. The deposits intertongue with the Campanian upper shale member of the Aguja Formation, increasing the known extent of Cretaceous volcanism in the Big Bend region. Zircon grains extracted from basalt bombs in the pyroclastic deposits yield a U–Pb SHRIMP-RG age of 76.6 ± 1.3 Ma.

On the Pitcock Ranch and adjacent parts of the park, Eocene basaltic dikes and phreatomagmatic diatreme root zones show various styles of magma-sediment interaction with the Javelina, Black Peaks, and Hannold Hill Formations. Billowed dike margins, intrusive pillows, and different types of peperite developed in strata as old as the Late Cretaceous, which must have remained unconsolidated and rich in pore water into the Eocene.